# THE FREE-FALL DETERMINATION OF THE UNIVERSAL CONSTANT OF GRAVITY

by

**JOSHUA PETER SCHWARZ**

B. A., University of Massachusetts,1993

M. S., University of Colorado, 1996

A thesis submitted to the
Faculty of the Graduate School of the
University of Colorado in partial fulfillment
of the requirements for the degree of
Doctor of Philosophy
Department of Physics
1998

This thesis entitled:
The Free-Fall Determination of the Universal Constant of Gravity
written by Joshua Peter Schwarz
has been approved for the Department of Physics

James Faller

Douglas Robertson

David Bartlett

John Hall

Date ____________

The final copy of this thesis has been examined by the signatories, and we find that both the content and the form meet acceptable presentation standards of scholarly work in the above mentioned discipline.

Schwarz, Joshua Peter (Ph. D.,Physics)

The Free-Fall Determination of the Universal Constant of Gravity

Thesis directed by Professor Adjoint James Faller

The Newtonian constant of gravity, G, is the constant of proportionality that scales the magnitude of the gravitational force between masses. G is the least precisely known of all fundamental constants. Recent high-precision experiments to measure G have produced highly discordant results, with values spread over a range of 0.7%. The situation is almost incredible; the second digit of the value is in contention and experiments disagree by as much as 50 of their individual error estimates.

We have developed a new determination that uses an absolute free-fall gravimeter to sense the gravitational attraction between a known source mass and a falling test mass. We use a one-half metric ton source mass whose position is alternated from above to below the dropping region, either decreasing or increasing the observed acceleration of the test mass. The source mass generates a differential signal of 8 parts in $10^7$ of the local acceleration due to the Earth. This method is independent of many of the systematic errors associated with the traditional torsion balance experiments upon which the accepted value of G is based.

Using this "free-fall" method in two data runs of approximately two weeks, we have found a value of G at the level of 1100 ppm. Our value is: $G = (6.6873 \pm 0.0076)\ X10^{-11}\ m^3/kg\text{-}s^2$. This value lies in the approximate center of the range of recent results

# ACKNOWLEDGEMENTS

Many people have offered assistance with my experiment. Tim Niebauer originally suggested the method of using the gravimeter to measure the acceleration signal of a source mass to determine G. But there is no doubt in my mind that the person most responsible for the free fall experiment was Jim Faller. Jim provided the energy and drive to get the experiment flying, and in many respects drew me along for the ride. His was the insight that lead to our source mass design, and also provided an example of the type of thought that I most enjoy attempting.

Doug Robertson was like a second advisor to me. While Jim discussed (and argued) different points of apparatus with me, Doug and I worked closely on the software framework that was crucial for the experiment. Doug offered liberal constructive criticism on my rough drafts, and good ideas about the experiment.

In more practical ways the instrument makers John Andru, Dave Alchenberger, Jim Csotty, Blaine Horner, Cole Briggs, Seth Wieman, Hans Rohner, and (especially!) Hans Green helped me (or did I help them?) with the design of the lifting assembly. I certainly was no help to Hans Green or Blaine when they did the actual work.

I didn't understand the purpose of the supply office until it was too late. That didn't stop Ed Holliness, Maryly Dole, Brian Lynch and David Tegart from defying all the laws of physics I learned about to get me everything I desperately needed (UPS RED!) on time. Ed and Brian also helped me work on my ping pong game and throwing arm. In this capacity they boosted my self confidence to the heights required to submit a dissertation.

The last two paragraphs have mentioned many people, yet it only covers the first floor of JILA. The Computing and Electronics Department is on the second floor. Terry Brown, Joel Frahm, Alan Dunwell, James Fung-A-Fat, Paul Beckingham, Mike Whitmore, Ralph Mitchell, Nick Metro, Peter Ruprecht, and Chela Kunasz have helped me with all my electronics and computer needs. Terry Brown, especially, worked hard to fill my electronics-empty skull with ideas about the discriminator circuit of the gravimeter (Chapter 3). He also helped me with my arm, and kindly ran patterns for a rookie QB. James kept me honest by toying with me on the raquetball court. He would have ruined my self confidence, if I had been so foolish as to challenge him while working on this thesis.

The Scientific Reports Office is also on the second floor. It's in a corner in the building, where the Jewels are kept. Laurie Kovalenko and Marilee DeGoede waded through so many sentences like this one that I can't help suffering from feelings of deep remorse — although I also experience feelings of thanks and admiration because they were both such good writers, knowledgeable like I am not, and feelings of regret because I'm leaving and won't be able to depend on their help again, never ever, ever any more — maybe.

Outside of JILA the kind folks at Micro-g Solutions, Inc. were a great help to us. They worked hard to help us get the experiment up and running quickly so that we could capitalize on the gravimeter time were allocated. Tim Niebauer, Fred Klopping, Kip Buxton, Jess Valentine, Jerry Gschwind and Echo never let us down. I'd especially like to thank Fred and Jess, who were always very nice to me even though I was needy.

From NOAA and the Table Mountain Gravity Observatory J.D. Williams, Tonie van Dam, Dan Winister and Glenn Sasagawa helped us wade through red tape on our way to borrowing the gravimeters we used.

I've thanked the people who have helped with the experiment, and now I'd like to give a hearty handshake[1] to all the people who have helped me to make it through — not by pointing out systematic errors in our experiment, or by suggesting alternate data analysis techniques, but by helping with "the life part". Many people I've already mentioned fall into this class. Jim Faller, for example, supported my interests in subjects apart from physics. We had many enjoyable conversations about Music, Sport, and Fine Dining that helped me keep proper perspective. Every one in the instrument shop, too, always made me feel welcome to shoot the breeze, have some popcorn and join up for a ride up Flagstaff.

Lisa Perry, LaReina Romero, Cheryl Glenn, Fran Haas, and even Leslie Haas were almost always available for a quick chat whenever the mood arose. Cheryl has suffered through hummed melodies from my singing classes, while Lisa was always quick to demonstrate proper technique (not just in singing).

Before there was JILA there was the Department of Physics, and classes. Both Susan Thompson and Linda of "The Department" made me feel like more than a cog in the machine. Somehow they also made sure that I fulfilled the bureaucratic requirements of the grad school — two tough jobs.

Without Harold Volkie Parks, Darren Link, and Greg Rakness I never would have scraped by. I needed three full-time tutors, and luckily that's what I got. These three even helped feed me, by working out a system where I was taken to lunch by everyone who got better exam scores than mine. Such generosity of time, knowledge and food is too rare. Nevertheless I found similar generosity (well, two of three…) in all my classmates. I think that we were all lucky in our peers.

That leaves all the special people. I hope they know who they are.

---

[1] I had "hug" here, but the first person I started to write about was Jim…

# CONTENTS

CHAPTER

**APPENDIX**

# FIGURES

Figure

# TABLES

Table

# CHAPTER 1

# INTRODUCTION

The world we live in is largely defined by gravity. When we see the waves of the ocean below or the sky above we are conscious of the effects of this far reaching force. The atmosphere we breathe, the light of the sun, the fall of rain, the shape of a flame — all are consequences of the attraction of matter.

> For my ally is the Force. And a powerful ally it is... Its energy surrounds us and binds us... You must feel the Force around you. Here, between you... me... the tree... the rock... everywhere! Yes, even between this land and that ship!
> — Yoda, The Empire Strikes Back, George Lucas

The force that defines the arrangement of the stars above us is a subject well deserving of appreciation, contemplation, and study. It is no wonder that for thousands of years questions about gravity have occupied the minds of the curious and contemplative.

Sir Isaac Newton provided the first model that we of the modern world cite when considering the effects of this powerful attraction, in a description that all physicists learn in the formative years of their studies:

$$F = \frac{GMm}{r^2}$$

Just this snippet of information is very valuable, for it forms the basis of much knowledge of how things interact – how the forces of gravity vary with mass and distance.

Without the universal gravitational constant, G, it is not possible to scale the force – to calculate the gravitational attractions between objects, even if their masses and relative positions are known. Although the practical benefits of performing this calculation are far and few between, the value of G is of real interest in some areas of physical research. Geophysicists, geologists, and seismologists use the value of G to deduce information about the structure and makeup of the Earth. Cosmologists and astronomers, on the other hand, base information concerning astronomical structure and the early universe on G[1]. Theorists who work on unification the four known forces need to know G to gauge the success of their theories.

It is the search for this constant that forms the basis of this dissertation, and has motivated many experiments since the late eighteenth century. Experiments to measure G have all had to deal with the same set of tough issues. Most important is the requirement that the experimental system be very sensitive to the gravitational field of a well-known mass, yet simultaneously be very insensitive to all other forces. This is a difficult demand to meet because the force of gravity is so weak in comparison to other forces. The following calculation illustrates this point. The accepted value for G, as of 1998, was

$$G = (6.6726 \pm 0.00085) \times 10^{-11}\ \mathrm{m}^3/\mathrm{kg} - \mathrm{s}^2 \tag{1.1}$$

based on the 1986 adjustment of standards. We can use this value to estimate the gravitational attraction between two average sized people (Jack and Jill) in a close hug:

$$F = \frac{\mathrm{G} \cdot (\mathrm{Mass}_{\mathrm{Jack}})(\mathrm{Mass}_{\mathrm{Jill}})}{\mathrm{Distance}^2}$$

which may be approximately

$$F = \frac{(6.7X10^{-11}\mathrm{m}^3/\mathrm{kg} \cdot \mathrm{s}^2)(65\mathrm{kg}) \cdot (50\mathrm{kg})}{(0.3\mathrm{m})^2} = 2.4\ \times 10^{-7}\ \mathrm{N}$$

This is equivalent to the weight of three tenths of one billionth of a gram (luckily gravity is not the only attractive force!).

We don't generally think of gravity as weak because we associate it with the pull of the entire Earth. Yet other forces can easily swamp gravity on many length scales. An example is the electrostatic force; the minute charge picked up when your feet scuff a rug is enough to cause slips of paper to stick to your hair, defying the gravitational attraction of the whole world. A more quantitative comparison can be made between the magnitude of the electric attraction of a proton for an orbiting electron and the gravitational force between them. The electric force is $10^{40}$ times larger.

Another hard fact of G-measurements is that gravity can't be shielded. If I wished to produce a region that was free of electric fields, all I would have to do is construct a conducting shell around the region. If I wanted to exclude magnetic fields, I could make the shell super conducting. If I need to exclude gravitational fields, then I had better think of a different experiment!

For this reason G experiments are designed so that it is not necessary to have a gravity-free environment for their success. Most experimenters, however, would like to circumvent one major component of the gravity field that exists on Earth – namely the attraction due to the planet itself. Experimentalists have commonly attempted to do this by using a torsion fiber to support a dumbbell-shaped beam. This allows horizontal forces to be expressed in twists of the fiber support without strong dependence on the local acceleration.

Fibers have been most commonly used in torsion balances, first conceived by the Minister John Price and used by Henry Cavendish in his famous determination of G [2]. The torsion balance is used by measuring the shift of the equilibrium position of the beam due to the gravitational attraction of external masses (Figure 1.1). Because fibers twist very easily even small gravitational forces produce a

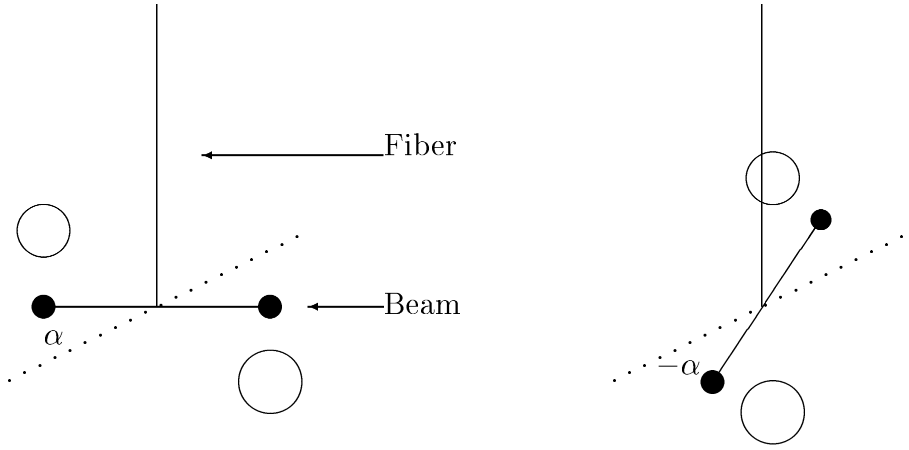

Figure 1.1: Schematic of a torsion balance. A dumbbell-shaped beam is hung from a torsion fiber. External source masses (hollow circles) deflect the beam from its equilibrium position (dotted line). The deflection changes depending on where the source masses are placed.

significant shift in the equilibrium position.

To relate the change in equilibrium position to the value of G it is necessary to calibrate the torque produced by the twisted fiber. This is typically done by measuring both the oscillation frequency of the system without the source masses present and the moment of inertial of the beam. These two measurements can be combined to give a value for the torsion constant of the fiber. The torsion balance is sensitive to more than just the gravitational signal of the source masses. Changes in the fiber can affect both the equilibrium position of the beam and the natural frequency of the isolated system, skewing the results of the experiment.

A very similar experimental setup can be used in a different type of measurement called a “time-of-swing,” “torsion pendulum,” or “Heyl-type” experiment[3]. This method requires that the frequency of oscillation of the beam be recorded. Source masses add a gravitational torque that acts on the beam either to enhance or decrease the effective torsion constant of the fiber (Fig. 1.2). By quantifying the effect of the masses on the period, the value of the gravitational constant can be found.

The vast majority of precision G experiments done since Cavendish have used either torsion balances or torsion pendulums. Over the ninety years before the 1986 setting of the accepted value, more than three quarters of all G measurements used one of these two systems. Of the three most accurate experiments before the reassesment of the accepted value in 1986, two (Luther and Towler [4] and Sagitov et al.[5]) used torsion pendulums, while the third (Karagioz and Izmailov ([6])) used a torsion balance. The accepted value of the constant, today, is based on the Luther and Towler number. More complete discussion of the measurement of G in the last 200 years may be found in Gillies[7], Bagley [8], and Koldewyn [9].

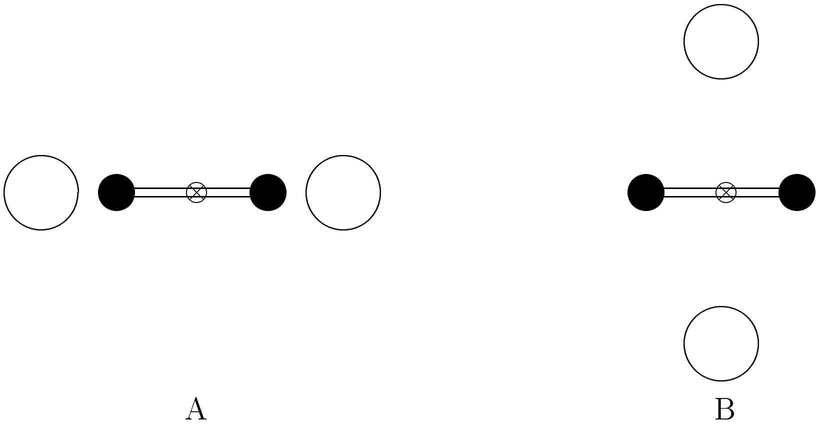

Figure 1.2: A schematic of the time-of-swing method. A torsion pendulum (in its equilibrium position) is represented by the dumbbell-shaped rod. $\otimes$ represents the torsion support. The hollow circles represent source masses. A) The source masses gravitationally augment the restoring torque of the fiber, increasing the frequency of oscillation. B) The source masses decrease the frequency of oscillation.

Recently fiber-based torsion experiments have come under attack. They are subject to a systematic effect that was first recognized in 1995 by Kazuki Kuroda[10]. The error arises because the anelastic relaxation effects in twisted fibers change the torsion constant of the fibers; real fibers diverge slightly from the simpler model of twisted members that had been used until Kuroda released his findings. This systematic error affects both torsion balance and pendulum experiments. Continuing research on this characteristic of fibers is ongoing [11, 12]. There are also plans to operate a torsion pendulum at cryogenic temperatures, to reduce anelastic effects [13].

## 1.1 G-Whiz: The Current Situation

The dominance of torsion fiber based determinations of G, coupled with uncertainty about fiber anelasticity, lead to four new experiments that have produced results in the last three years (Figure 1.3). The results vary over such a large range (0.7%) that the probability that the disagreement is due to a statistical fluctuation is approximately one in $5^{18}$.

The first measurement was conducted by Walech, Meyer, Piel and Schurr, at the University of Wuppertal, Germany [18, 19]. The group used two simple pendulums to support mirrors defining a microwave Fabry-Pèrot resonator. By placing a source mass system on the line between the pendulums, the distance between the two bobs was changed. The resonator measured the separation change, thereby scaling G. Their initial result[18], released in 1995, was:

$$\mathrm{G} = 6.6719 \pm 0.0006 \ \times 10^{-11} \mathrm{m}^3/\mathrm{kg} \cdot \mathrm{s}^2$$

This value was the only recent result consistent with the accepted value. In 1998 large systematic errors associated with the positioning of their source masses came to light. When they correct their previous result to reflect these errors, their value changes to:

$$\mathrm{G} = 6.6637 \pm 0.0004 \pm 0.0044 \ \times 10^{-11} \ \mathrm{m}^3/\mathrm{kg} \cdot \mathrm{s}^2$$

This value lies 2 standard errors below the accepted value [16].

Fitzgerald and Armstrong of the New Zealand Standards used a nulled torsion balance [15]. This is a normal torsion balance experiment with one important

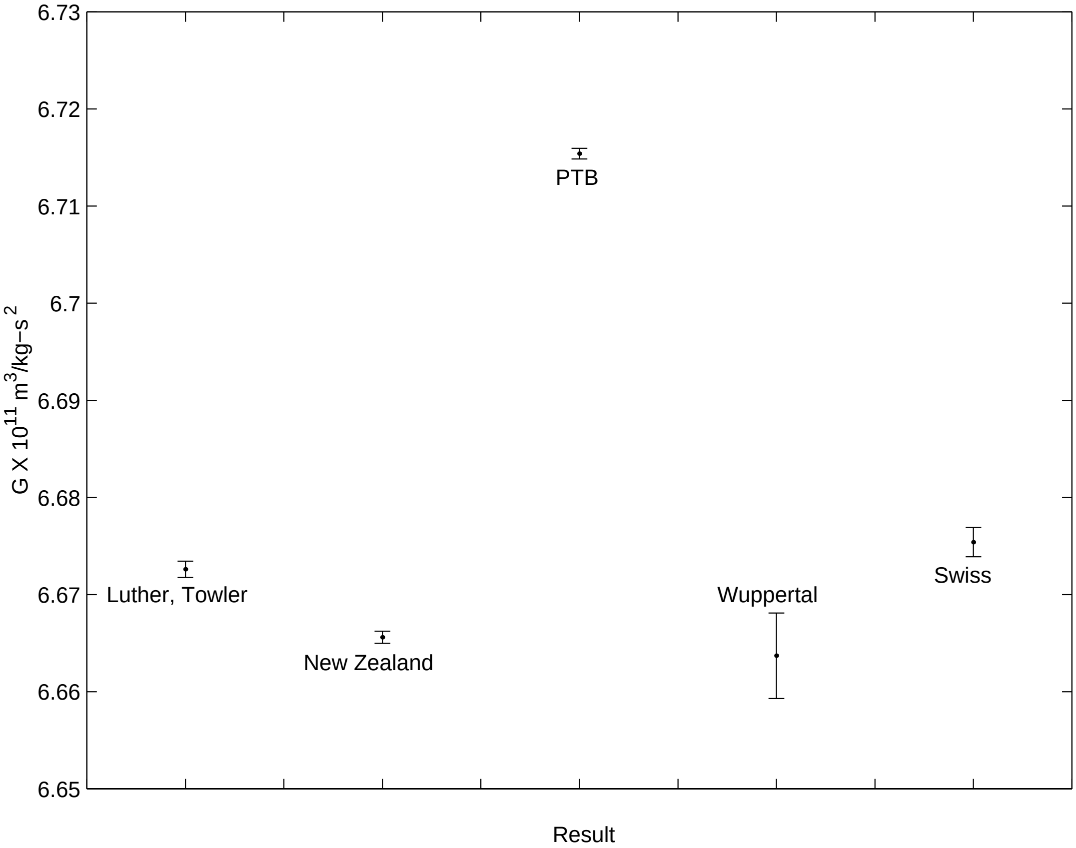

Figure 1.3: Four recent results of G experiments. The 1982 result of Luther and Towler at the NBS [4] is the basis of the accepted value. The results of the PTB (German Standards, $42\sigma$ high [14]), the New Zealand Standards ($10\sigma$ low [15]), and a group at the University of Wuppertal ($2\sigma$ low [16]) were all released in 1995. A group in Switzerland released a preliminary result in 1998 ($2\sigma$ high [17])

difference — the torque of the source masses was not matched by the twist in the fiber, but rather by a torque produced by electrostatic forcers. The forcers were servoed to maintain the orientation of the beam. This method has the advantage that the orientation of the beam doesn't change, so spatially variant horizontal gravity gradients do not influence the results. Also, this type of system is not subject to fiber anelasticity problems. The major hurdle with this method is in the calibration of the torque produced by the forcers. Fitzgerald and Armstrong released a result in 1995:

$$\mathrm{G} = 6.6656 \pm 0.00063 \ \times 10^{-11}\mathrm{m}^3/\mathrm{kg}\cdot\mathrm{s}^2$$

This result is 11 standard errors ( about 0.1% ) below the accepted value.

At the Physikalisch-Technische Bundesanstalt (PTB)[1] de Boer, Haars and Michaelis have carried out a similar experiment for which planning began in 1976 [14, 20]. They used a compensated torsion balance with a mercury bearing, rather than a fiber, to support the beam. This type of bearing is nearly free of static friction. The experimenters made measurements of G at different distances and between different materials. These measurements gave consistent results. In 1995 the final result of their measurement was released:

$$\mathrm{G} = 6.7154 \pm 0.00055 \ \times 10^{-11}\mathrm{m}^3/\mathrm{kg}\cdot\mathrm{s}^2$$

This represents a disagreement with the accepted value of more than 40 $\sigma$ (0.6% high).

A group at the University of Zürich, consisting of J. Schurr, F. Nolting and W. Kündig [17, 21] is currently measuring the difference in the weight of two masses[2] . They modulate this difference by moving two source masses around the

---

[1] The PTB is the German Bureau of Standards

[2] This method is similar, in some respects, to our own "free fall" method, and shares many of its benefits. The difference, for example, is measured in the vertical direction, so this determination is made with the perturbing gravitational attraction in-line with the attraction of the Earth.

two weights. The group uses two large flasks containing 13.5 tons of mercury as their source masses. They released a preliminary result (using water instead of mercury in the flasks) in February of 1998:

$$\mathrm{G} = 6.6754 \pm 0.0015 \ \times 10^{-11} \mathrm{m}^3/\mathrm{kg} \cdot \mathrm{s}^2$$

This result is $2\sigma$ above the accepted value.

Let us summarize the situation. Many experiments have been effected recently, yet at the level of a quarter percent there is no clear value for G. The new experiments use a variety of methods, most moving away from twisted fiber ideology, but their results fail to converge. The large spread in results compared to small error estimates, as shown in Fig.1.3, indicates that there are large systematic errors in at least two of the three high precision results.

A need for experiments that are independent of the torsion/twisted support methodology exists. Consider that the two values with the largest discrepancies with the accepted value are based on similar experiments using different torsion supports (PTB and New Zealand). Also recall that the great majority of G experiments relied on a twisted fiber torsion approach to the measurement, a method subject to systematic errors that are only now becoming understood.

The "Free Fall Measurement of G" is presented in this thesis. The free fall measurement is unique in that it uses an unsupported test mass to sense the gravitational force. It senses this force in a direction parallel to the acceleration due to the Earth (no torque). This method, therefore, has a very different set of systematic errors than other G-experiments. We hope that our results will add useful information in the current situation of nearly one-half a percent of uncertainty in G.

## 1.2 The Free-Fall Method

The free-fall method depends on our ability to measure the amount that an external source mass changes the acceleration of a freely falling object. First a source mass is placed above the region in which the "test mass" falls. Here the gravitational pull of the source mass acts in the opposite direction to the attraction of the Earth, decreasing the downward acceleration of the test mass. Second the source mass is placed below the drop region, where it augments the Earth's attraction and the acceleration of the falling mass. If the change in acceleration can be measured accurately, and if the geometry of the source and test masses are well known, then we can determine G.

This is conceptually simple, yet in practice the subtleties of the measurement are plentiful. These subtleties arise from the lack of an ideal mechanism to measure the acceleration of the test mass. The acceleration signal produced by our source mass is only 1 part in $10^7$ of the signal of the Earth. Thus we need to precisely measure a small acceleration signal on top of a huge offset. To achieve an accuracy in our measurement of 0.01%, we must have a precision of 1 part in $10^{11}$ in the measurement of the absolute acceleration of the falling object. This is not an easy task.

Fortunately free-fall gravimeters have been developed to precisely measure the local acceleration of gravity, g. The gravimeter drops an object and records its position as a function of time. By fitting the position/time curve with a parabola the acceleration of the test mass is extracted.

Working at JILA we were perfectly poised to capitalize on the utility of free-fall gravimeters for the G measurement. The gravimeter we used, a Micro-g Solutions, Inc. model FG-5, grew out of free-fall gravimeter systems that were developed in JILA by Jim Faller[22], James Hammond, Robert Rinker[23], Mark

Zumbergezumberge, and Tim Niebauer[24]. Tim originally suggested the idea for the free-fall measurement of G, and is the head of the Micro-g Solutions, Inc. Thus we had, at our elbows, a group of people with tremendous expertise with the gravimeter system. Also the University of Colorado, which is associated with JILA, owns an FG-5 that we were able to borrow for our measurements.

The experiment was carried out at the Table Mountain Gravity Observatory (TMGO), a center for the research and development of absolute and relative gravimeters, 10 miles north of Boulder. TMGO is operated by the National Oceanic and Atmospheric Administration (NOAA). Running the experiment at TMGO was crucial to the success of the free-fall measurement because of the exceptional quality (low vibration noise) of the site. Also TMGO is equipped with secondary measurement systems that were extremely helpful in our experiment.

A free fall gravimeter uses a laser interferometer system to track the motion of the falling test mass. The test mass contains a corner-cube retroreflector that defines one arm of a Michaelson-type interferometer. Thus the interferometer fringe crossings correspond to changes of the test mass's position. By incorporating a precise time standard, a stable position reference, and all the electronics and hardware required to drop the test mass in vacuum, it is possible to record the position as a function of time of the falling mass. The absolute accuracy of the system is $1\mu$Gal, or approximately one part in $10^9$ of the acceleration due to the Earth[3] . It is limited by machine-dependent uncertainties arising from (among other things) residual air pressure in the vacuum can, electrostatic forces, and the attraction of the gravimeter itself.

In the free-fall G experiment we were more interested in the change of the acceleration of the test mass than its absolute acceleration. This meant that we were not limited by the accuracy of the gravimeter so much as by its precision. We

---

[3] A Gal is a cm/s$^2$, and a $\mu$Gal is 1e-6 Gal.

operated the gravimeter in a differential mode that eliminated “common mode” errors in the measurement — errors that were independent of the source mass position. This allowed us to achieve a precision in our result that is more than twenty times greater than the absolute accuracy of the gravimeter.

The perturbing gravity field that changed the acceleration of the falling mass was produced by a ring-shaped source mass made of 500 kg of tungsten alloy. The use of a ring-shape gives a tremendous advantage over traditional spherical or solid cylindrical source masses because the axial acceleration field produced by a ring has two extrema. This means that there are two positions at which the field of the masses doesn't change with a movement from that position; there are two positions for the source mass that cause our results to be nearly insensitive to positioning errors. The source mass was located alternately above and below the drop zone in these two places, as shown in Fig.1.4. The actual experimental setup is shown in Fig.1.5 with the source mass in its upper position.

Conceptually the experiment was a variant of a classical orbit determination problem in which our free-falling test mass was the orbiting body [25]. In effect, we did a satellite laser ranging experiment in a laboratory. But in contrast to classical spacecraft tracking problems, where one determines the quantity GM (G times the mass of the primary planet or star, M), we were able to extract G because we measured M in the laboratory. The close analogy to conventional spacecraft tracking problems allowed us to use a number of classical orbit determination techniques.

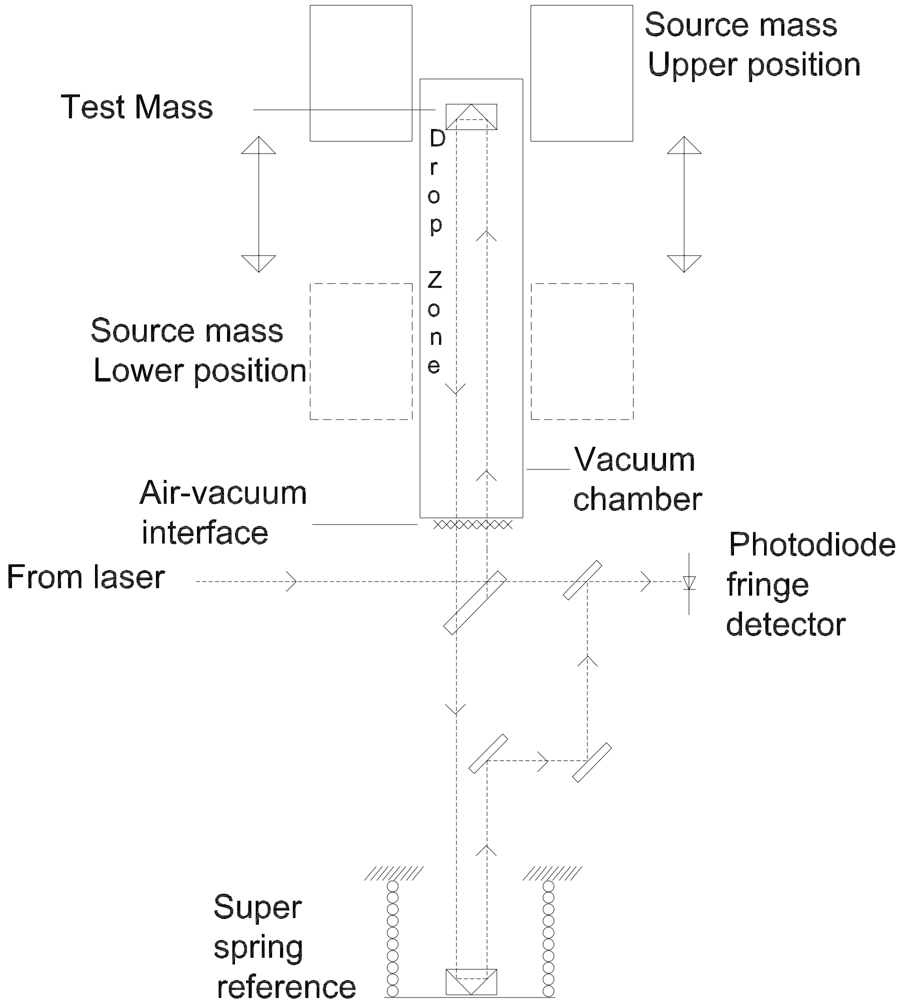

Figure 1.4: A schematic cross-section of the experimental apparatus. The source mass was alternately placed at positions A and B at twenty minute (100 drop) intervals.

Figure 1.5: A photograph of the experimental apparatus. The source mass is in its upper optimal position around the dropping chamber. The interferometer looks like a black box located below the dropping chamber. The super spring hangs below the interferometer. The large aluminum structure was built for the G-experiment, and supported the source mass.

# CHAPTER 2

# THEORY

The underlying physics of the free-fall determination have been well understood for hundreds of years. Two equations are sufficient to classically describe the gravitational interaction between masses. Sir Isaac Newton first recognized the relationship between the mass of two point particles ($M$ and $m$), their separation ($d$), and the magnitude of the gravitational force ($F$) between them:

$$F = \frac{GmM}{d^2} \tag{2.1}$$

Newton's second law,

$$\mathbf{F} = m\mathbf{a} \tag{2.2}$$

describes the acceleration, $\mathbf{a}$, of a mass $m$, arising from the application of a vector force, $\mathbf{F}$. The second law, although only valid in a classical regime of low velocity, is sufficiently accurate to describe the action of the free-fall experiment.

These equations allowed us to calculate both the attraction between the test and source masses, and the theoretical path that the falling test mass was expected to follow. Although these calculations were developed from a straightforward model, they were nontrivial. The test mass and the source mass were both complicated objects, composed of many different pieces with a variety of densities. Also, the attraction between them depended on their relative positions, which was time dependent.

The problem of determining the motion of a falling object is often treated in spacecraft tracking experiments. We used a number of numerical methods that were developed for tracking applications. These included the use of the numerical quadrature of Eqn. 2.1, the numerical integration of the equation of motion, and "Encke's Method" for dealing with differential equations that include small perturbative terms[26].

This chapter deals with the mathematical and computational work necessary to solve for the motion of a test mass falling in the presence of a fixed mass. First the calculation of the mutual attraction of the two masses is presented. Second the determination of the expected path of the falling object is laid to view. These two steps fully define our expectations of the physical behavior of the system. The manner in which these "great expectations" and the observed data are brought into agreement is dealt with in Chapter 4.

## 2.1 Mutual Attraction of the Free-Falling and Source Masses

To calculate the instantaneous force between the source and proof masses we integrated the gravitational attraction of each differential element of one mass to each bit of the other mass. This involved a three-dimensional integral over each volume:

$$m_p \frac{d^2 \vec{r}_p}{dt^2} = \iiint_{V_p} \iiint_{V_s} \frac{G \rho_s \rho_p}{|\vec{r'}_s - \vec{r'}_p|^2} \, d\vec{r'}_s \, d\vec{r'}_p \tag{2.3}$$

where the subscripts $p$ and $s$ refer to the proof and source mass respectively, $V$ is the volume, $\rho$ is the density, $m_p$ is the mass of the proof mass, and $\vec{r}$ is the position vector. For this theoretical work we used an assumed value (the 1986 CODATA number) for the gravitational constant. The vertical component of the force is given by:

$$m_p \frac{d^2 z_p}{dt^2} = \iiint_{V_p} \iiint_{V_s} \frac{G \rho_s \rho_p z'}{|\vec{r'}_s - \vec{r'}_p|^3} \, d\vec{r'}_s \, d\vec{r'}_p \tag{2.4}$$

in which $z$ is the vertical component of $\vec{r}$. This integral cannot be analytically solved for an arbitrary mass configuration, so it was numerically solved. However, by limiting the description of the source and proof masses to collections of right cylinders, the integral could be partially reduced analytically. This greatly simplified the computation of the mutual attraction, and also eased the modeling of the two masses. Working now in cylindrical coordinates with $z$ representing the vertical position, and $\vec{r}$ the polar vector, the integral for the attraction between each pair of cylinders was reduced to four dimensions. The vertical integration over each cylinder of the source and test mass was analytically solved:

$$\begin{aligned}\sum_{C_p C_s} \iint_{A_p} \iint_{A_s} d^2\vec{r}_s\, d^2\vec{r}_p\; G\rho_p\rho_s \Big[ & \frac{1}{\ln(z_{p2}-z_{s2}+\sqrt{(\vec{r_p}-\vec{r_s}+\vec{\delta})^2+(z_{p2}-z_{s2})^2})} \\ & - \frac{1}{\ln(z_{p2}-z_{s1}+\sqrt{(\vec{r_p}-\vec{r_s}+\vec{\delta})^2+(z_{p2}-z_{s1})^2})} \\ & + \frac{1}{\ln(z_{p1}-z_{s2}+\sqrt{(\vec{r_p}-\vec{r_s}+\vec{\delta})^2+(z_{p1}-z_{s2})^2})} \\ & - \frac{1}{\ln(z_{p1}-z_{s1}+\sqrt{(\vec{r_p}-\vec{r_s}+\vec{\delta})^2+(z_{p1}-z_{s1})^2})} \Big]\end{aligned} \tag{2.5}$$

where the sum is over the set of cylinders comprising the proof ($C_p$) and source ($C_s$) mass models. $\delta$ is the horizontal offset between the integration cylinders. The integrals are over only the ends, $A$, of the cylinders because the vertical integral has been analytically solved.

We used Romberg quadrature to execute the integrations. In Romberg quadrature simple trapezoidal evaluations of the integrations are computed with a variety of step sizes. The set of results is then extrapolated to find the value corresponding to an infinitesimal step size. By increasing the number of step values used in the extrapolation, and recording the progression of the extrapolated value, limits can be placed on the error of the extrapolation. This method is an example of "Richardson's deferred approach to the limit." The actual code that we used for each dimension of the integral is presented in Refs. [27, 28]

The model of the test mass is made of nearly 100 cylinders, that of the source mass of approximately 60. Thus the simplified integral of Equation 2.5 must be computed for approximately $60 * 100 = 6000$ cylinder pairs (for a single test mass position relative to the source mass). This was an extremely large task because the integrations are layered; if a single numerical integration requires 20 evaluations of the integrand to converge, then a single four-dimensional integral would require $20^4$ evaluations of the integrand and the computing cycles required to execute the integration routine $20^3$ times. To complete our problem an average workstation[1] would take approximately eight months.

To speed up the integration I split the integral into two portions, each performing a set of two dimensional integrals. This allowed the use of an interpolation grid to break the layering of the integrals. With an interpolation grid the value of the inner two integrations could be "looked up" for whatever range of variables the grid covers, avoiding the inner layer integrations[2] . Thus, for the outer two integrals, the integrand doesn't contain a double integral, but only a lookup of the value for the inner integrals at the appropriate point. If a four dimensional layered integral is split into two two-dimensional integrations in this way, it would only require $2X20^2$ evaluations of the integrand, a factor of 200 decrease over a straight evaluation.

The first set of integrals were evaluated over the cylinders of the source mass, returning the magnitude of the vertical acceleration field produced by them. The integrals were evaluated along a two-dimensional grid covering the two dimensions of vertical and radial position with respect to the source mass. Only two dimensions were required (instead of three) because I made the assumption that the

---

[1] Here "average" refers to an HP 730/9000 series workstation. This probably was average in the mid-1990s.

[2] "Lookup," as used here, isn't a rigorous term. It refers to the operation of interpolating the values associated with the grid points to an intermediate point. I have made the assumption that such a lookup takes negligible time — compared to the time required for a double integral this is very reasonable.

source mass field was cylindrically symmetric. This was a reasonable assumption given the symmetry of both the test and source mass, and was highly accurate. The completed interpolation grid was, essentially, a description of the source mass gravity field.

The second set of integrations were calculated over the volume of the proof mass, on the interpolation grid. Each differential bit of mass, $\delta m$, was subject to a force proportional to the value of the gravity field, $a(z, r)$ at its position:

$$\delta F = \delta m \, a(z, r)$$

Thus the net force[3] on the proof mass was calculated.

Alternatively, this set of integrations may be thought of as the averaging of the acceleration field over the volume of the proof mass, weighted by the density of each cylinder of the model. The result of the second set of integrations is a single number — the acceleration of the entire test mass due to the entire source mass. The use of the interpolation field decreased computation time by a factor of 500.

It was necessary to know the influence of the source mass on the proof mass throughout the length of the drop. This was found by evaluating the second set of integrations at a sequence of (vertical) test mass positions. The sequence was used to create a second interpolation array, containing the acceleration of the proof mass due to the source mass. Thus the source mass perturbation, at any vertical position, was readily available by interpolated from this one-dimensional grid.

---

[3] It was the acceleration of the test mass, not the force acting on it, that interested us. Thus the force was divided by the net mass of the proof mass, returning the acceleration. Note that the acceleration of a falling mass is independent of its mass, but not its mass distribution

## 2.2 Theoretical Determination of the Trajectory

Once the gravitational attraction between the source and proof mass was quantified we needed to calculate the theoretical path that the proof mass would follow. This was done by integrating the acceleration of the proof mass twice with respect to time. For an object in a constant acceleration field, $-g\hat{z}$, the equation of motion is:

$$\frac{d^2z}{dt^2} = -g. \tag{2.6}$$

When integrated twice with respect to time, the equation gives the path of the object,

$$z(t) = -\frac{1}{2}gt^2 + V_0t + Z_0 \tag{2.7}$$

with the boundary conditions $z(t=0) = Z_0$ and $z'(t=0) = V_0$.

The actual acceleration field the proof mass fell through was not constant either in time nor space. A linear gradient term is the first order correction to a constant field. With such a term the equation of motion becomes:

$$\frac{d^2z}{dt^2} = -g + \gamma z \tag{2.8}$$

where $\gamma$ is the magnitude of the linear gradient — typically on the order of 3 parts in $10^9$ of the local acceleration per centimeter for the gravity field of the Earth. Integration yields

$$\begin{aligned} z(t) = \frac{g}{\gamma} & - \frac{g}{2\gamma}(e^{-\sqrt{\gamma}t} + e^{\sqrt{\gamma}t}) \\ & - \frac{V_0}{2\sqrt{\gamma}}(e^{-\sqrt{\gamma}t} - e^{\sqrt{\gamma}t}) \\ & - \frac{Z_0}{2}(e^{-\sqrt{\gamma}t} + e^{\sqrt{\gamma}t}) \end{aligned} \tag{2.9}$$

Alternatively we can substitute Eqn. 2.7 into Eqn. 2.8 to get an approximate polynomial solution:

$$z(t) = \frac{1}{2}g(t^2 + \frac{\gamma t^4}{12}) + V_0(t + \frac{\gamma t^3}{6}) + X_0(1 + \frac{1}{2}\gamma t^2) \tag{2.10}$$

This approximation is clearly very good over the length scale of this experiment. It is merely the first few terms of the Taylor expansion of the hyperbolic functions. By expanding Equation 2.9 to sixth order in $\sqrt{\gamma}t$, with $X_0$ and $V_0$ set to zero for clarity we get Equation 2.10 with a single correction term, $C(t)$:

$$C(t) = -\frac{\gamma^2 g t^6}{6!} + \mathcal{O}(t^8)$$

Over the length of the drop the difference between the two parabolas is negligible.

This completes the description of the motion of a particle falling in a uniform gravitational field with a linear gradient, but we still must include the effect of the source mass distribution. The perturbing acceleration, $P(z, G)$, was numerically calculated from Eqn.2.3. Adding this term to the equation of motion gives:

$$\frac{d^2 z}{dt^2} = -g + \gamma z + P(z, G) \tag{2.11}$$

Clearly $P(z, G)$ depends on both the proof mass position relative to the source mass and the actual value of the constant of gravity. Eqn. 2.11 must be integrated numerically because $P(z, G)$ was not analytically described. We used the Bulirsch-Stoer algorithm [27], which relies on the Richardson extrapolation technique much as Romberg quadrature does[4] .

To further increase the accuracy of the integration, we used a technique known as "Encke's Method"[26]. The differential equation 2.11 contains a large simple differential equation, Equation 2.6, that is perturbed by a small complicated term, $\gamma z + P(z, G)$. Encke's method is simply a change of variables, to allow separate integrations of the constant field and the perturbation terms. We define $\chi$ as the solution of the unperturbed equation:

$$\frac{d^2 \chi}{dt^2} = -g \tag{2.12}$$

---

[4] Here we integrate a differential equation, not a simple integrand, so the intermediate points used in the extrapolation come from modified-midpoint integrations.

thus $\chi$ is the second degree polynomial of Equation 2.7. If $z$ is the exact solution to the whole differential equation, and $\delta z$ is the difference between the $z$ and $\chi$, then:

$$\begin{aligned} \frac{d^2\delta z}{dt^2} &= \frac{d^2 z}{dt^2} - \frac{d^2\chi}{dt^2} \\ &= P(z, G) \end{aligned}$$

Encke's method was used to avoid round-off error introduced by the large position and acceleration values of the "total solution."

## 2.3 The Solutions

The numerical integration of the equation of motion allowed us to calculate the position versus time path of the falling test mass as a function of: 1) The relative position of the start of the drop relative to the source mass. 2) The source mass configuration. 3) The proof mass configuration. 4) The value of G. 5) The value of the local gradient, $\gamma$. 6) The initial velocity of the proof mass.

To illustrate the abilities this conferred upon us, I include some plots describing the (theoretical) proof mass motion. Figure 2.1 displays the acceleration experienced by the test mass due to the source mass. Note that the acceleration field is highly symmetric around the center of the source mass (approximately a position of 10 cm) because of the vertical symmetry of the source mass. There are two optimal source mass positions in the experiment, corresponding to the extrema of the acceleration curve. The two positions maximize the acceleration signal of the source mass; this is how the they are defined. These positions also minimize sensitivity of the signal to the relative position of the drop and the source mass[5] . Additionally, they minimize signal sensitivity to source mass inhomogeneities and test mass modeling errors.

---

[5] The signal is insensitive to changes of both the vertical and horizontal position of the drop.

Figure 2.2 shows the perturbation to the parabolic path of the test mass when dropped with the source mass either in its upper or lower position. The symmetry of these perturbations is somewhat unexpected. It arises because the source mass was positioned to take advantage of the extrema of the acceleration curve; the source mass was placed to produce an effect most like that of a constant field (this defines the positional invariance characteristic of the two optimal positions).

The experiment consisted of quantifying the source mass's perturbation to the path. This measurement is described in the next chapter, on "Experimental Apparatus." The task of scaling the theory to experimental data is discussed in Section 4.

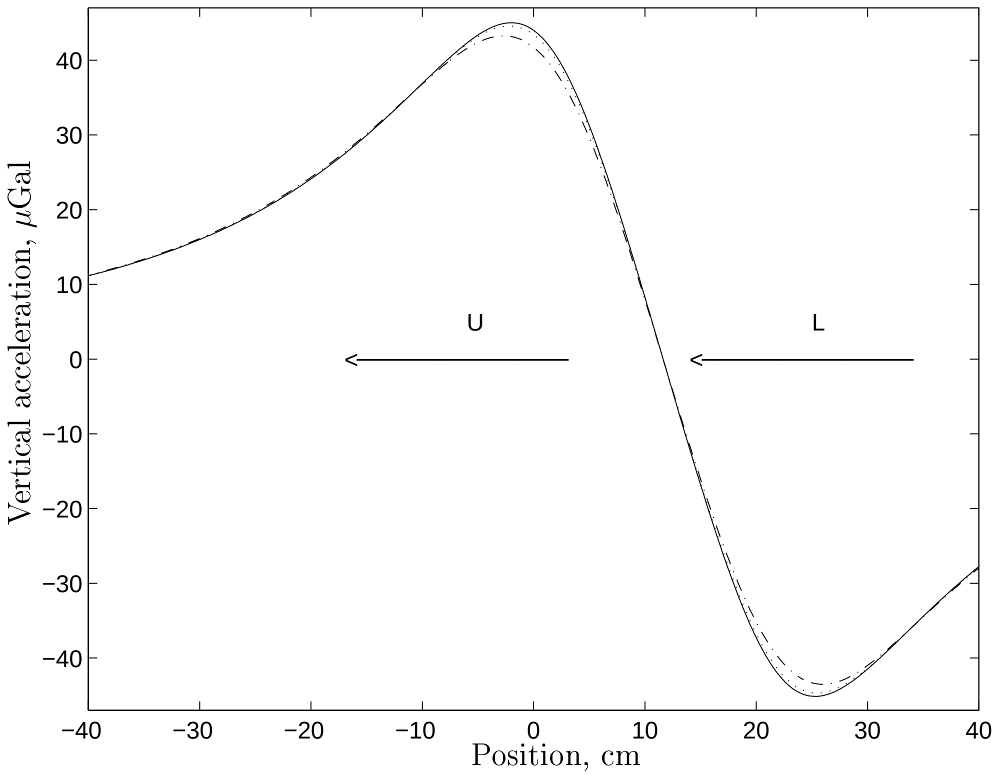

Figure 2.1: Vertical acceleration of a test mass due to the source mass. Plotted against the test mass position above the bottom of the source mass. A point mass on axis (···), 2 cm off axis (—), and the acceleration of the actual proof mass of the experiment (–·–). The acceleration of the test mass was less than that experienced by a point mass because of its vertical extent. The lines marked by "L" and "U" indicate the region of the field that the proof mass fell through when the source mass was in its lower or upper optimal position, respectively. Note that the field magnitude increased with distance from the axis. The field is assumed to be cylindrically symmetric.

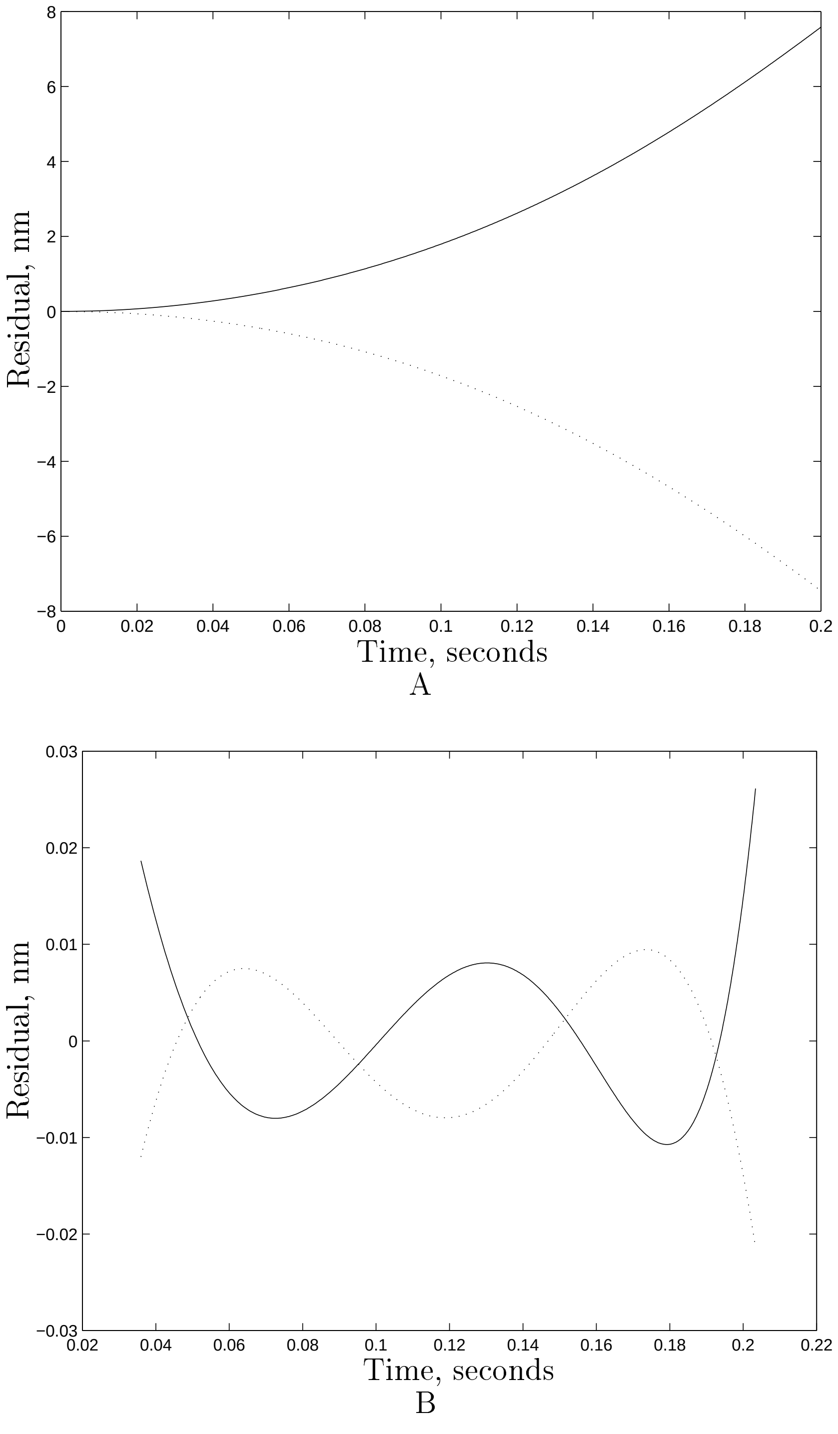

Figure 2.2: Source mass perturbation (position as a function of time) to the theoretical trajectory for the freely falling test mass. With the source mass in its lower (——) and upper(···) positions. A) The total perturbation. B) The perturbation with parabolic components removed.

# CHAPTER 3

# EXPERIMENTAL APPARATUS

This chapter will present the basic design of the apparatus and some of its subtleties. We have used different incarnations of the experimental apparatus described here in three data runs. The first was a proof-of-concept experiment that used a relatively light source mass. This "bronze mass data run" is described in Section 6.1.1. Our experience with this preliminary set up inspired the main design, described in this chapter, and used for a data run in 1997. The data recorded during this run motivated several modifications that were made to the gravimeter system and source mass for a final run in 1998. The final experiment is discussed in Section 6.1.3.

## 3.1 The Measurement System

All the utility we needed to drop an object and measure its position as a function of time was provided by a+

Micro-g Solutions FG-5 Free Fall Absolute Gravimeter. Free fall gravimeters work by measuring trajectory of a falling object. By fitting a parabola to the path of the dropped object, a value for g is obtained. The FG-5 extends these simple ideas to high levels of accuracy and complexity. When used in a traditional measurement of local gravity, the FG-5 is accurate enough to sense the gravity change resulting from a vertical movement of a third of a centimeter[1] . This is roughly equivalent to a 100 picosecond change in the time necessary to fall twenty centimeters (the length of the drop). At this level of accuracy there are many pitfalls in all phases of the measurement.

Many subtleties of the g measurement exist, and most influence the G results. It is important to note that the gravimeter was designed to measure the local acceleration of gravity, not perturbations to it. This fact allowed the G-measurement to exploit the precision of the gravimeter, as opposed to its accuracy. We extended the utility of the gravimeter to a regime never before explored, sharpening our need to understand the system fully.

The description of the gravimeter is spread over three sections covering the dropping system, the interferometer, and the position reference used by the interferometer. These are not physical, so much as logical, divisions.

### 3.1.1 The Dropping System

The dropping system of the gravimeter (Fig.3.1) was designed to drop the proof mass from a well known and constant position (the "start-of-drop" or "SOD" position), and allow it to fall without any rotational velocity while shielded from non-gravitational forces. The system's success is dependent on its ability to minimize the effects of residual gas in the vacuum, magnetic fields, electrostatic charges, and thermal gradients. The dropping system is very important to the experiment. The repeatability of the start-of-drop position, the angular motion imparted to the test mass, and the alignment of the drop with the chamber influence the accuracy we can achieve with the free-fall method.

---

[1] The gravity gradient is approximately $3\mu$Gal/cm. The acceleration is falling off because the drop occurs at a greater distance from the Earth. $1\mu$Gal is the advertised uncertainty in the accuracy of the FG-5.

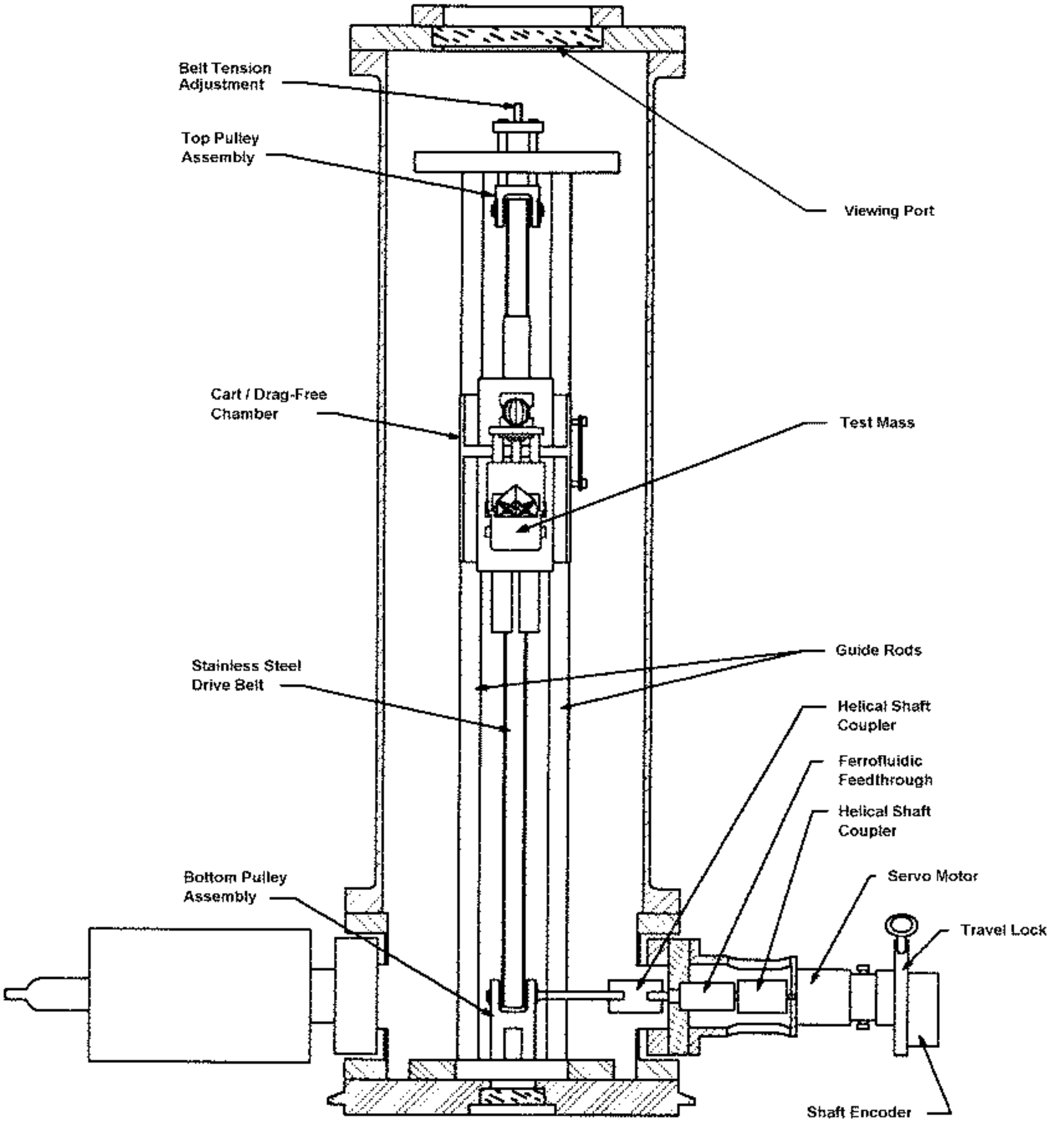

Figure 3.1: A schematic of the dropping system. The vacuum can forms a continuous conducting shell around the drop region, reducing electrostatic forces. The viewing port at the top of the chamber is made of glass with a thin conductive coating. This drawing is courtesy Micro-g Solutions, Inc.

#### 3.1.1.1 The Vacuum System

The first level of shielding from gas, thermal, and electrical signals is provided by the vacuum chamber. The chamber is made of aluminum which, besides its conductive properties, is non-magnetic and has high thermal conductivity. It forms an unbroken conductive shell around the drop region, reducing the magnitudes of stray electric fields. The can's thermal properties helps minimize temperature gradients (a discussion of thermal effects and their magnitudes may be found in Section 5.2.2). An ion pump at the bottom of the chamber maintains a vacuum of approximately $10^{-6}$ torr, reducing the effects of air to a level of 0.1 $\mu$Gal. The vacuum chamber is supported on a thick aluminum "party tray" with three legs. The party tray clamps onto the chamber to fix its orientation.

The dropping can of the FG-5 incorporates a few "bonus features". The can is equipped with an optically flat window at its top. The window provides a port for optical determinations of the position of the proof mass inside the can, or for measurement of the proof mass rotation during a drop. The window is coated with a conductive layer and is grounded to the rest of the chamber.

In the G experiment we used a custom chamber dimensioned so that the source mass could be positioned as near to the drop as possible. During the data runs the vacuum can was covered with a layer of nylon mesh and aluminum foil, decreasing the sensitivity of the dropping system to thermal signals.

#### 3.1.1.2 The Co-falling Chamber

The structure that executes the drop and catch of the test mass is located within the vacuum can. Three stainless steel ground rods guide an "elevator" that supports the test mass. This elevator, or "co-falling chamber," is servoed to follow the test mass during the drop, providing a zero-g environment that minimizes the effects of residual gas in the chamber. The co-falling chamber provides a secondary level of thermal, electrical, and magnetic shielding. Because it surrounds the test mass it does not have a strong effect on the test mass acceleration ($\ll 1\mu$Gal). The quality of the servo is so poor ($\approx \pm 0.01$ mm) that there is no concern that there could be a systematic differential bias in our results from this source.

A simple mechanical system is used to drive the co-falling chamber. A DC servo motor drives a belt (via a pulley) that moves the lift along its guides. A shaft encoder registers the angular position of the pulley, and thus a relative vertical position of the co-falling cart. Before each drop the co-falling chamber rests on a stop at the bottom of the vacuum can. At this position the shaft encoder is reset. This allows referencing of the vertical position of the cart both at the stop and at the SOD position[2] . The SOD position is an important parameter in the G experiment, which requires that it be constant[3] . Because the shaft encoder is reset at the known position of the stop, there can be no cumulative slip between the belt and the drive pulley. It is not possible that there be slip between the time that the shaft encoder is reset and the time that the cart is lifted to the SOD position. This is because the cart could not consistently track the falling mass if the belt was significantly loose. If the drop is not completely botched, then there will be no problem with the relatively gentle lift of the cart to the SOD position.

The drop begins with the initialization of the time standard and data storage boards of the gravimeter computer system. The co-falling cart motion is controlled by several analog servos, each controlling a different phase of the movement.

In a 20-30 ms “lift off” phase the co-falling cart is accelerated downwards at 2g, resulting in a test mass – cart separation of 3 mm. As soon as the drop starts, the whole dropping chamber rebounds upwards due to the weight change arising from the cart’s acceleration. This rebound motion is discussed in depth in Sec. 5.2.1.

The drop continues for 20 cm with the cart tracking the position of the proof

---

[2] The shaft encoder/motor system is servoed to match a voltage output by the encoder with a reference voltage. The reference voltage defines the distance from the reference stop to the SOD position.

[3] The SOD position is also important in absolute gravity measurements, but at a lower level than in the G measurement.

mass, and ends with a “soft-catch, ” in which the cart gently rises to meet the proof mass. The cart and test mass are decelerated and set against the reference stop where the shaft encoder is reset. The cart is then servoed to the SOD position where vibrations die down until the next drop sequence starts.

### 3.1.2 The Interferometer System

The measurement of the test mass position during the drop is made with an interferometer. The test mass acts as one arm of the interferometer, resulting in a correlation between its position and the number of fringes observed at the interference output. Figures 1.4 and 3.2 contain schematic views of the interferometer.

The light source for the interferometer is a He-Ne laser locked to an optical hyperfine absorption peak in $I_2$ (red light, $\lambda \approx$633 nm). The iodine peak defines a frequency standard so the wavelength of the laser can be used as a length standard without calibration.

The interferometer output during a drop is a chirped sinusoid in light intensity superimposed with a constant light intensity. The sinusoid arises from the motion of the test mass [4] . This signal is monitored with an avalanche photo diode that converts the intensity signal into a voltage signal, allowing a high-speed discriminator to identify fringe crossings.

The photo diode voltage is high-pass filtered (with a 700Hz corner) to remove any DC voltage offset[5] . Thus, at frequencies above 700 Hz each transition of the

---

[4] The time for the test mass to travel a distance corresponding to a fringe decreases is proportional to its velocity. The velocity increases linearly with time. This is why the sinusoidal signal is chirped. The constant light intensity occurs because there is a slight difference in the light power sent down each arm of the interferometer. Thus only some fraction of the light interferes.

[5] Voltage offsets are removed to help ensure that the discriminator is triggered when the slew rate of the intensity signal is maximum. This reduces the sensitivity of the trigger to noise on the signal.

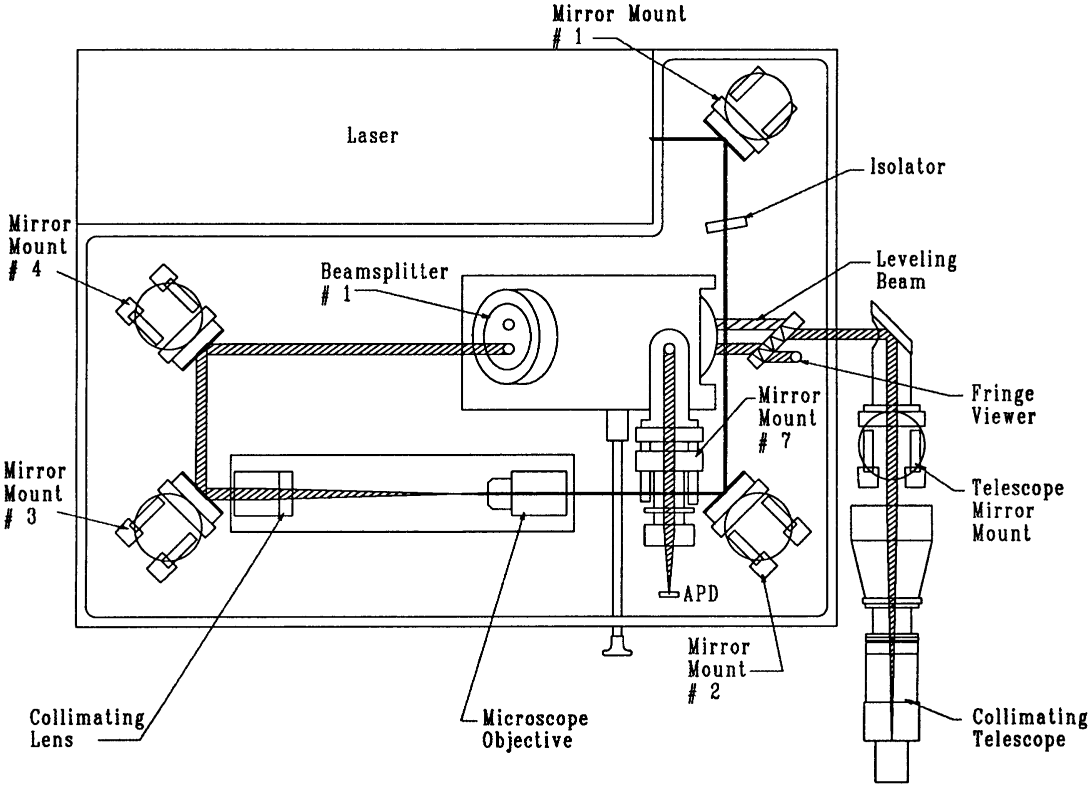

Figure 3.2: Schematic of the standard FG-5 interferometer. The drawing lies in the horizontal plane. Thus the laser beam extends out of the page to illuminate the proof mass, and into the page to strike the reference mirror. This drawing is courtesy Micro-g Solutions, Inc.

voltage from positive to negative represents a light fringe. Each fringe represents a shift in length between the two arms of the interferometer of $\delta z = \frac{\lambda}{2}$. The number of fringes (actually zero-crossings) that occur are counted, and a scaling factor, $n$, is applied to the fringes; the time of each n$^{th}$ fringe is recorded. Because of software limitations, the minimum scaling factor is 500. This corresponds to a time/position datum at every 1/3 mm of travel, providing approximately 650 data points for each 20 cm drop. The fact that the data are equally spaced in position implies that they are chirped in time – the data are more dense at the end of the drop than at its start (in time).

The stabilization scheme used to lock the laser requires that its frequency be modulated over 6MHz at 1.2 kHz [29]. This dither is seen as a high frequency sinusoidal position signal, but by fitting for a sinusoid at the appropriate frequency, the effect of the dither on the data is minimized. Ideally the laser light would be provided without any dither, to avoid the additional processing and fitting errors associated with removing this signal.

As an aside, note that the errors in the measurement arising from the light pressure of the laser beam on the test mass, time delays due to the finite speed of light, and Doppler shifting of the laser frequency are all common mode errors that don't affect the experiment.

### 3.1.3 The FABIO system

In a data run in 1998 the interferometer of the gravimeter was replaced with a fiber-optic system, called the Fiber Absolute Interferometer (FABIO). FABIO uses a fiber-optic link to pipe laser light to the interferometer arms (the laser is placed a few meters from the dropping chamber). FABIO reduces the number of mirrors used in the interferometer, thereby improving the stability of the verticality of the laser beam.

When we used FABIO a polarization-maintaining (PM) fiber was used. To our surprise, the set-to-set scatter acceleration values doubled. This was especially unexpected, because the short-term drop-to-drop scatter did not increase. At the time we suspected the FABIO system, and specifically the PM fibers. Tim Niebauer suggested a mechanism to explain the increase in scatter at the longer time scale of sets that involved drifts of the polarization carried by the fiber.

Testing of the gravimeter and FABIO system after the G measurement was over showed that the set-to-set scatter was normal and that there was no dependence of g on the polarization carried by the fiber (at levels interesting in absolute determinations of g). Thus the choice to use FABIO appears to be unrelated to the increased scatter. Section 6.1.3 includes discussion about possible sources of the noise.

### 3.1.4 Phase Shifts at the Discriminator Input

Frequency dependent phase errors introduced in the fringe signal by the electronics of the discriminator/APD system result in position/time signals that may mimic accelerations of the proof mass. Phase shifts could be introduced by electronic filters or by the limited bandwidth of the APD. In the FG-5 the APD has a bandwidth of 50 MHz so the phase errors introduced at 6 MHz (the maximum frequency of the interferometer signal) are very small (corresponding to a error in g of approximately 0.1 $\mu$Gal).

The phase error problem doesn't affect the differential signal unless the error is dependent on the source mass position. We don't expect any such dependency because the APD/filter/discriminator circuit was positioned within the interferometer, far from the source mass and doubly shielded from its direct thermal signature.

The fact that phase errors don't affect the G measurement (unless they are truly gigantic) raised an interesting possibility. By limiting the bandwidth of the APD circuit we could reduce its statistical noise in the measurement of the fringe crossings. This would reduce the drop-to-drop scatter in g-values. Truncation of the bandwidth necessarily results in phase bumps in the circuit, but in the differential mode, this was not a concern. The filter would have the same effect as increasing the data sampling rate[6] .

I wrote a software simulation that showed that a four-fold decrease in the

---

[6] We could not simply increase the data density because of software limitations in the gravimeter system. In the future experimenters would be well served to put in the work required to convert the software system to a form that would support storage of arbitrarily dense data.

bandwidth (achieved by placing a low-pass filter with a corner of 12.5 MHz between the APD output and the discriminator input) would cause only a 10 $\mu$Gal shift in absolute gravity and negligible bias in our results. If the noise introduced by the large bandwidth of the APD were the main source of drop-to-drop scatter then this filter would win a factor of close to 2 in scatter, and thus the same factor in the integration time required to reach a given precision in G. This was a reasonable expectation because the residuals in least squares fits to drop data correspond well with the actual scatter observed.

We tested a low-pass filter at 12.5 MHz for use in a data run in 1998. The scatter did not decrease as quickly as expected. There was no significant decrease in the size of the residuals until we used a filter corner frequency of only 8 MHz. Worried that the filters were acting as antennas and injecting additional noise into the system, we decided to forgo the use of the filter altogether.

#### 3.1.4.1 The Test Mass

The test mass is a complicated object designed to fulfill several criteria. It incorporates a mirror, a spherical lens, and a counterweight. The test mass is 9 cm long, approximately 2 cm wide, and is made of aluminum, tungsten, vespel, glass and beryllium copper. The test mass used in the G-experiment weighed 101.2 grams. Different test masses generally weigh within a gram of 101 grams.

The test mass includes a corner cube retroreflector. Corner cubes have the property that incoming light rays are reflected anti-parallel and offset from their incoming paths. The reflected ray is insensitive to rotations of the corner cube so long as the rotations occur around a point known as the “optical center” of the cube. To minimize path length errors (and the associated acceleration bias) due to the inevitable rotations of the freely falling test mass, the optical center of the corner cube must as close as possible to the center of mass of the entire falling object. Therefore the test mass incorporates a counterweight that is used to align the center-of-mass to within 4 microns of the optical center of the reflector.

To allow the co-falling chamber to track the test mass as it falls, the test mass contains a small optical glass sphere at its upper end. The sphere acts as a lens that focuses the light of an LED onto a linear position sensor. Both the LED and the detector are hard mounted to the co-falling chamber. The output of this position sensor is used in the servo loop that controls the drive motor.

Three tungsten balls support the test mass on matching tungsten vees on the co-falling chamber. Tungsten is used to reduce wear in the balls resulting from the catch phase of the drop. The balls and vees are placed and oriented to impart minimal rotational and horizontal velocity to the test mass at the start of the drop. The fact that the balls do wear and change the mass distribution within the test mass is discussed in Sec. 5.2.5.

The framework that holds these components is made of aluminum. The aluminum aids in reducing electrostatic forces, but is subject to eddy-current forces. Mark Zumberge suggested constructing the proof mass from non-conductive material, but was concerned about increasing the effects of thermal signals [30]. Theory and experiment have shown that the eddy-current effects are negligible in normal conditions. Because aluminum has low magnetic susceptibility the test mass is not strongly influenced by direct attraction to magnetic fields.

### 3.1.5 The Position Reference System

A stable reference is required to make any position measurement. In the FG-5 this reference is provided by a “super spring” one-dimensional active isolation unit. The super spring was originally built by Robert Rinker as a dissertation project with James Faller [23]. Since its conception it has undergone many refinements, finally resulting in the super spring used in the G-measurement. Figure 3.3

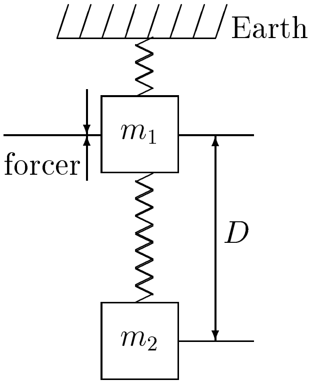

Figure 3.3: Schematic of the super spring one-dimensional isolation system.

shows a schematic of the design of this system.

The super spring may be considered as normal spring that has been fooled into acting like it is very long ($\approx 1$ km). A servo loop applies a force to $m_1$, trying to keep $D$ constant (to some level of gain). Thus $m_1$ tracks $m_2$, effectively servoing the portion of the spring between the two masses as though it was the last few coils of a much longer spring. Because the period of a spring depends on the amount it is stretched ($S$) in the following way:

$$\begin{aligned} mg &= kS \\ \frac{m}{k} &= \frac{S}{g} \\ T &= 2\pi\sqrt{\frac{m}{k}} \\ T &= 2\pi\sqrt{\frac{S}{g}}, \end{aligned}$$

$m_2$ is isolated from much lower frequency vibration signals than would be filtered by a simple spring system of the same physical length as the super spring.

The super spring supports the reference arm of the interferometer system, and therefore has direct influence on the level of scatter observed in the acceleration measurements. The effective period of the super spring is nearly 60 seconds, so the amplitude of oscillation must be kept under 5 nm to insure that the peak acceleration signal introduced by the reference is less than 5 $\mu$Gal. The super spring system succeeds in this goal, an impressive achievement considering that this corresponds to a 200-fold decrease in the vibratory acceleration signal of the earth at the fundamental frequency of the spring. For information about how the super spring reacts to the source mass position see Section 5.2.6.

The super spring is supported below the dropping system by a tripod (that also holds the interferometer). There is no contact between the dropping system and this tripod lest the vibrations triggered by the drop excite the super spring. At the Table Mountain Gravity Observatory, where our data was taken, there was additional isolation of the spring system. The interferometer tripod was placed on a pier of concrete embedded[7] in the floor. This reduced coupling of vibrations through the floor.

## 3.2 The Source Mass

A hollow cylindrical ring-shaped source mass was first used in a G experiment by Michael Hulett, working on a senior thesis project under Jim Faller. He used two bronze rings fashioned from the bushings for a ship's screw propeller. Later, in the mid-seventies, William Koldewyn[8] [31] used this same pair of cylinders in a G experiment that used a magnetically supported torsion pendulum. We used the identical masses in a preliminary version of our experiment, described in Section 6.1.1.

Hollow cylinders allow much laxer positioning requirements for G experiments because they produce a gravitational field with extremum values, as discussed in Sec. 2.3. Figure 2.1 shows the axial acceleration field for a hollow cylinder. At a certain distance from the center of the cylinder the field on axis

---

[7] The piers extended approximately 5 feet below the floor, and were surrounded with Styrofoam.

[8] Koldewyn also worked on his Ph.D. with Jim Faller, at Wesleyan University, 1976

reaches a maximal value that doesn't change with position. Thus the extrema represent areas in which the field is changing much more slowly than the traditional $1/r^2$ roll-off of the field produced by a spherical mass.

The axial force is also unchanging with respect to radial translations (from the axis of the cylinder). This is expected from symmetry considerations — the force must get either larger or smaller (than it is on axis) as you move off axis in any direction. The axial force increases closer to the inner walls of the cylinder, so the axis represents a minimum in axial force as a function of radius.

Thus a ring-shaped mass generates a field insensitive to translations of the mass in any direction (at two points). The G-experiment, however, integrates the field of the source mass over a finite distance — the length of the drop. Although the absolute position insensitivity of the field exists at only two points, the extrema result in two SOD positions that maximize the perturbation to the test mass trajectory. These positions correspond to the upper and lower source mass positions, the one decreasing g, the other increasing it.

These properties of the source mass were essential to the success of the experiment. Let's examine the situation if we were forced to use a spherical source mass, and contrived to place it above and below the drop path. The differential acceleration of a point test mass due to a sphere placed in two reasonable positions, above and below the dropping region[9] is strongly affected by positioning errors. A 1.0 mm error in positioning would result in a signal error of 1.5%. The same positioning error in our ring-mass system (correctly set up) would result in a signal change of less than 0.003%, 500 times less signal error. The sphere design is not even an option for the free-fall method.

The inner and outer radius and the height of the cylindrical source mass

---

[9] For this example, I assume that a sphere of the same mass and density of our source mass could be placed within 4cm of the top or bottom of the drop.

were determined by our requirements for the experiment. If the cylinder were too tall, for example, it would be physically impossible to place the source mass in its lower optimal point without very drastic modifications to the dropping system. On the other hand, if the mass were shorter than the greatest possible length, we would loose signal-to-noise.

The inner radius of the source mass is roughly inversely proportional to the signal magnitude — a smaller inner radius increases the signal. This parameter is limited by the size of the vacuum can and the clearance required between both the vacuum can and the co-falling chamber, and the can and the source mass. To minimize the inner radius we constructed a thin-walled chamber with a minimum of clearance.

The ring's outer radius affects both the signal size and the position of the acceleration extrema. This choice of particular parameter was based on both the ability of a single robust person to setup the mass, and the importance of the additional signal achieved by increasing the radius. As the ring increases in radius the signal gain is only linear, but the mass increases with the radius squared.

The approximate dimensions of the cylinder were 50 cm diameter, 27 cm height, 16 cm inner radius. Our source mass weighed approximately 521 kg. This geometry produced an acceleration signal that peaked at a value a bit larger than 43 $\mu$Gal. The total signal sensed by the gravimeter was approximately 82 $\mu$Gal. This is smaller than twice the peak signal of the source mass because of the extent of the test mass and the averaging action of measuring the acceleration over the length of the drop.

Once the approximate dimensions for the ring were fixed we concerned ourselves with limiting possible density variations throughout the mass. The most straightforward manner of determining the density structure within an uncharacterized mass is to chop it into small pieces and measure the density of each small bit. The amount of density information extracted depends on the size of the bits (minced tells you more than chopped). We decided to split the mass into 12 cylindrical pieces, as in Figs. 3.4 and 3.5.

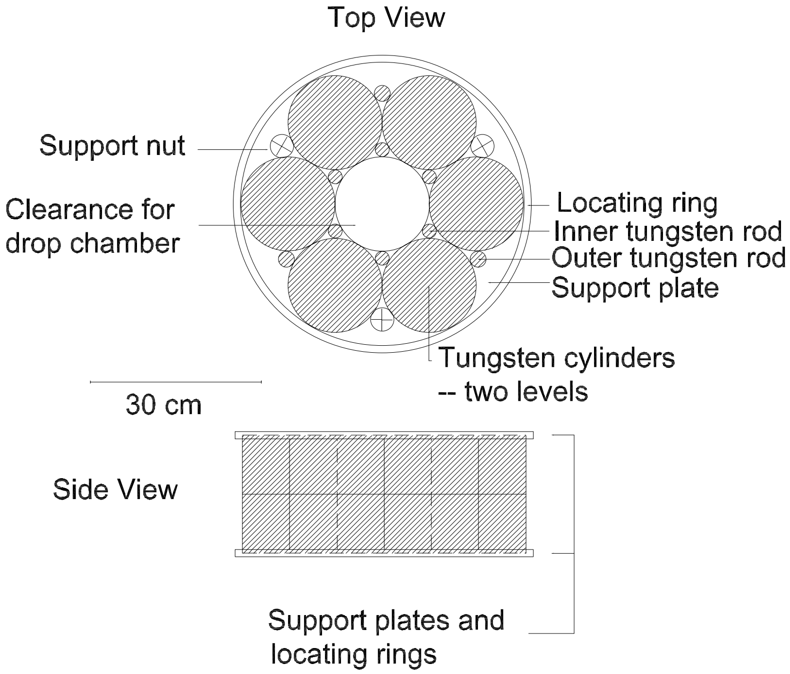

Figure 3.4: Schematic of the source mass. The source mass is constructed of non-magnetic materials including tungsten, aluminum, titanium, and bronze. Some stainless steel fixtures were also used.

Cylinders were chosen (instead of cubes, or irregular geometries) because of their rotational symmetry and amenability to form a ring shape. Cylinders can be characterized by more than just their density. Linear and angular density variations can be measured (as discussed in the next Section, 3.2.1).

The 12 cylindrical tungsten billets were mounted in two levels. Cylinders can be oriented in many ways so we were able to arrange them to best mimic a homogeneous set; any linear or quadratic gradients in the density over the whole height of the source mass were minimized. The gaps between the cylinders were filled with small tungsten rods, increasing the net density of the source mass.

Aluminum plates were used to sandwich the cylinders together. The plates

Figure 3.5: Photo of the source mass. The locating ring of the lower plate is clearly visible. Note how little clearance there was between the source mass and the vacuum can.

had rims with radii three times that of the cylinders (plus $\approx 200\ \mu$m clearance), insuring that the masses were precisely located in the radial direction. The upper plate provided additional strength, reducing flex of the bottom plate and deformation of the source mass.

The plates were bound together with tensioning rods and bolts tapped into the small tungsten rods. Throughout the design of the source mass we tried to preserve as much flexibility in mass positioning and support as possible, while maintaining symmetry to ease modeling tasks. The source mass was originally designed so that the top and bottom plate would be interchangeable, preserving its vertical symmetry. As the experiments progressed and modifications were made this symmetry was broken.

### 3.2.1 The Tungsten Masses

The tungsten cylinders were custom made for us by Schwarzkopft in Austria. They are made of Densimet 18k — a sintered metal of 95% tungsten with 5% copper and nickel as binding material. This material has good magnetic properties; it has volume susceptibility of 0.00066 (MKS) and is paramagnetic [32, 33]. We ordered the cylinders slightly oversized and had them finished in house. Blaine Horner, of the JILA instrument shop, insured that the cylinders would be as regular as possible and dimensionally consistent from piece to piece.

The cylinders were machined to 4.080" (10.363 cm) in height and 6.530" (16.586 cm) in diameter. Their diameters and heights are all consistent to 0.001" (0.002 cm), with masses of approximately 39700 grams. The mean density of the cylinders is 17.724 g/cm$^3$ with a standard deviation of 0.008 g/cm$^3$ ( 0.04% ). The peak to peak density variation was 0.02 g/cm$^3$ ( 0.12% ). Details of the cylinder masses and volumes are provided in Appendix A.

To determine whether the cylinders were cylindrically symmetric they were placed on an air bearing. Any inhomogeneity with angular dependence would result in a torque along the axis of rotation. The 'light' side of the cylinder was marked and then the frequency of oscillation due to the un-balancing torque was measured. It is possible to model an angular density variation as a bubble in the material. With the cylinder axis oriented along the $\hat{z}$ direction

$$\omega = \sqrt{\frac{mgr}{I}}$$

where $\omega$ is the angular frequency of oscillation due to a bubble of mass $m$ at radius $r$. $I$ is the moment-of-inertia of the cylinder.

The results of this test showed that 11 of the 12 masses had an angular density variation equivalent to a 25 gram surplus at the outer radius. This suggests that the variation is not due to bubbles (a bubble larger than 1 cc is very unlikely to occur) but rather a density gradient. Such a gradient was most probably a result of cooling effects. The billets were cut from 3 long cylinders that had been cooled on their sides. It is possible to find out more about the angular distribution of mass in the cylinders, but this test was sufficient to bound possible angular density variations.

Density variations along the length of the cylinders were also measured, as in Fig. 3.6. Given this information I was able to arrange the cylinders so that there was only a very small net linear density change from the bottom to the top of each layer of tungsten. This measurement was sufficient to limit linear and quadratic density dependence along the height of the whole source mass.

Using the information about density variations from one cylinder to the next, from one side of each cylinder to the other, and from their tops to their bottoms, I was able to make an error estimate for the assumption (made in our models) that the masses were homogeneous. The error from this source forms approximately a quarter of our net uncertainty. In a new experiment I would suggest constructing the source mass out of much smaller cylinders, spheres, or cubes than we used this time around. By decreasing the size of the individual components density variations could be better controlled.

### 3.2.2 The Drive/Support Structure

The support structure for the source mass consisted of a large aluminum tripod that supported three screws synchronously rotated by a stepper motor. The tripod was designed to allow easy disassembly for transportation purposes. Each leg was bolted into a thick "main plate" that formed the acme of the tripod. The legs had adjustable leveling feet. Tensioning wires ran from the plate to the legs increasing the rigidity of the structure and preventing twisting motions.

On top of the main plate of the tripod rested the "drive plate" that sup-

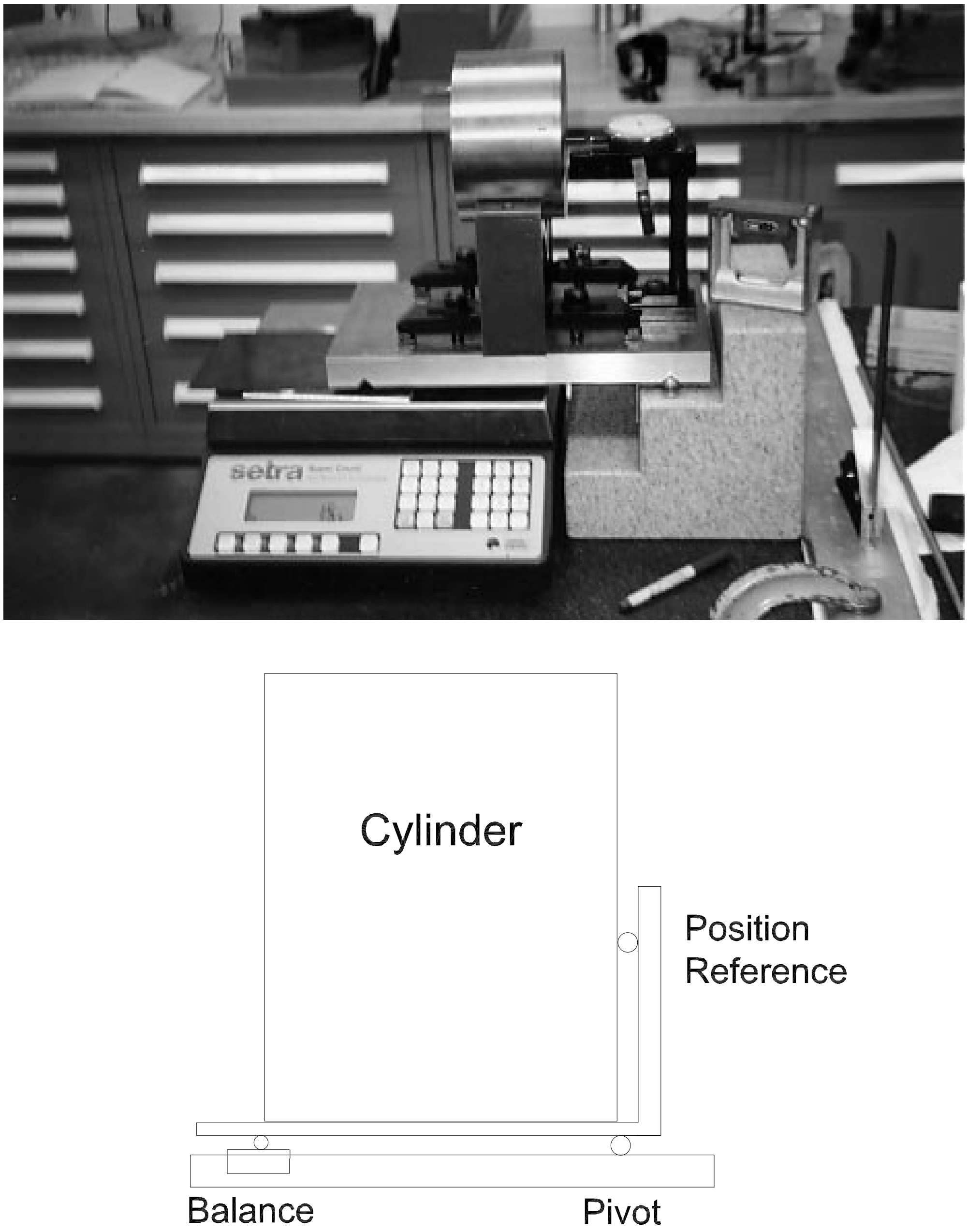

Figure 3.6: Photo and schematic of the pivot and balance system used to measure density variations along the length of the tungsten cylinders. Two 3/4" ball bearings were used to define the pivot line.

ported the screws and drive structure. The drive plate could be moved 2 cm in the horizontal plane to position the source mass concentrically with the dropping chamber (clearance for the screws was cut into the main plate). The drive plate was also equipped with a central retractable pivot that could be used to produce a pure rotation of the plate and screws in the vertical direction. This degree of freedom was incorporated in the design to insure that the screws could be positioned about the FG-5 with maximum clearance. After position adjustments the drive plate was clamped to the main plate to prevent creep.

The screws were supported by bolts riding on cylindrical roller bearings located in aluminum towers bolted to the drive plate (Fig.3.7). The towers provide space for a secondary set of cylindrical roller bearings that increased the rigidity with which the screws were held. Attached to each screw was a plastic sprocket keyed to prevent slippage. The three screw/sprocket assemblies were linked to each other with a stainless steel chain that was annealed to reduce its magnetic susceptibility. This chain cycle was driven by a sprocket rotated by a separate chain loop connected to a stepper motor. This constrained the screws to rotate synchronously (in the limit that there was no slack). The worst case phase shift between screws is equivalent to a single link misplacement because the sprockets provide, in some sense, a quantized positioning mechanism. Even this worst case shift was negligible.

The stepper motor was bolted to the main plate of the tripod as far from the FG-5 as possible. It was held with vibration isolating mounts The drive chain was turned through a rubber shaft attached to the motor. These isolating measures were taken to minimize the vibration of the ground due to the drive system, which could disturb the gravimeter. Although the vibrations were of too high a frequency to excite the super spring much, no vibration is good vibration.

Figure 3.7: Photo of the screw drive/support system. A) The drive plate. B) The main support plate. C) A tower supporting one of the screws. D) One of three clamps.

### 3.3 Superconducting Relative Gravimeter

Local acceleration may be affected through many mechanisms[10] . Atmospheric effects, for example, can change in gravity either by changing the mass of the air above the observation site, or by compressing the ground[11] . This signal has been calculated to be approximately -0.40 $\mu$Gal /mbar at Boulder ([24, 35]).

Tides, ground water changes, continental uplift and ocean loading can change gravity as well. Tides, by far the largest source of gravity signals ($\approx$ 150 $\mu$Gal), occur on a much longer time scale than the modulation of our source mass. Tides

---

[10] People have thought of many ways gravity measurements may be affected. It has been suggested that atmospheric pressure associated with solar eclipses could affect gravity[34]. The umbra moves with supersonic speed across the surface of the earth, creating a transient pressure disturbance due to the decrease in air temperature within the sunspot. The pressure change would then change the value of the local acceleration. Luckily solar eclipses don't happen every few minutes!

[11] The corresponding change in the distance to the center of the Earth increase the local acceleration.

are approximately biurnal (6 hour period), while our source mass position was alternated every 20 minutes, at the slowest. Thus tides did not correlate strongly with our signal. Some faster environmental signals, however, might have randomly correlated with the source mass position and increased the scatter in our results. These signals would not have systematically biased our final value.

To avoid unnecessary scatter we used a superconducting relative gravimeter (SRG) to record real time varying gravity signals concurrently with the G experiment. The SRG cannot provide an absolute value for the local acceleration (something like 9.8 m/s$^2$) but can only track relative changes in g. For example, between time $t$ and $T$, the relative meter might give a measurement equivalent to: $g(T) = g(t) + 12.345\ \mu\mathrm{Gal}$. We subtracted the gravity signal (as recorded with the SRG) from the acceleration values extracted from the absolute drop data. This reduced the scatter introduced into our experiment by real time varying gravity signals due to environmental sources.

The SRG works by measuring displacements of a mass on a spring. As the local gravity decreases, the mass is lifted by the spring. As the local gravity increases, the spring is stretched, lowering the mass. The change in equilibrium position can be related to the change in the weight (due to the change in gravity) of the mass through Hooke's law. A schematic of the system is seen in Figure 3.8. The mass in the SRG system is a superconducting niobium sphere and the spring is actually provided by a magnetic field generated by persistent currents running in two superconducting coils. The motion of the equilibrium position of the sphere is recorded with an AC capacitance bridge surrounding the sphere.

The spring constant of the SRG system must be calibrated before the position of the spring/mass equilibrium can be related to changes in gravity. The output can be calibrated in a variety of ways, but the SRG we used was calibrated

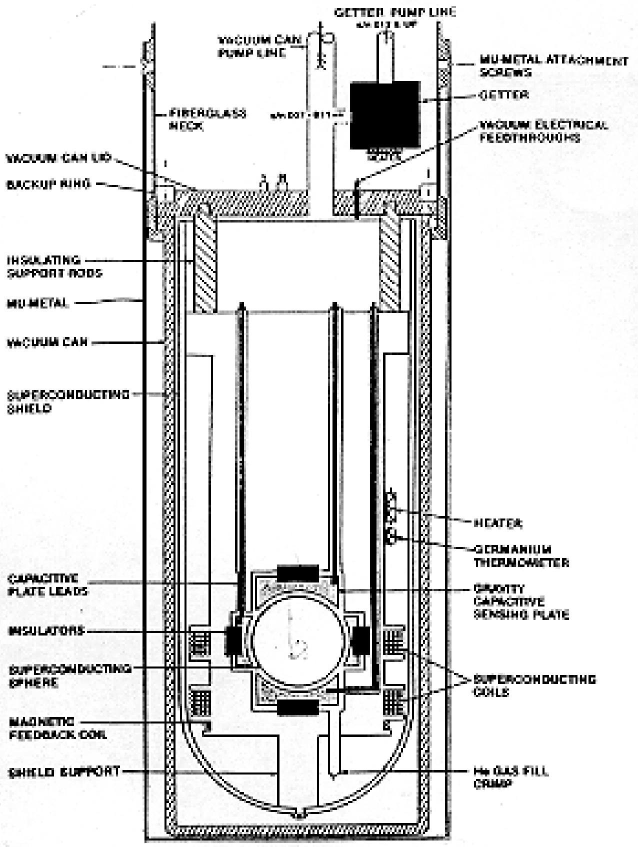

Figure 3.8: Schematic of the superconducting relative gravimeter used to record real time varying gravity signals. This drawing is courtesy GWR Instruments.

from another SRG[12] . The two systems were placed side by side and allowed to measure environmental signals concurrently. Comparison of the results completed the calibration. Any errors in the calibration would lead only to residual environmental signals in our data. It is important to note that the SRG system could not remove time varying signals arising from drifting errors in the free-fall gravimeter

---

[12] This second SRG was previously calibrated with a mechanical system that physically accelerated the entire SRG apparatus at known rates. Both calibrations were done by NOAA personnel independently of the G-measurement. The quality of the SRG raises the question "Why not do the free fall measurement with out the free fall? Just use a SRG." This is by no means an unreasonable question, and in fact the idea is good. There is no reason why this experiment should not be carried out. One issue that limits the utility of the SRG for a G measurement, however, is the difficulty of calibrating the output. Currently SRGs can only be calibrated to several parts in $10^4$.

system that actually recorded the acceleration signal of the source mass.

The SRG is subject to drifts and steps in its output. Some drifts result from mass changes of the niobium sphere (it adsorbs helium). Throughout our data run we performed linear least squares fitting for the drift and determined that it was less than 0.2 $\mu$Gal per day — having negligible impact on our values for the G.

# CHAPTER 4

# ANALYSIS

A central task that we faced with the free fall method was implementing the software system used to extract G from gravimeter data. This chapter describes the algorithms we used to this end. Preliminary work was discussed in Chapter 2. Section 2.1 included the calculation of mutual attraction of the test mass and source mass over the large range of relative positions in which they are placed. In Sec. 2.2 the method of numerically integrating the equation of motion of the test mass was presented.

## 4.1 A Big Least Squares Solution

A statistically correct way to extract G from observed data is to calculate a least-squares solution in which G is a fitting parameter of the problem.

One might imagine fitting the parabolic path of the dropped object to a function, $z(t)$ composed of a standard solution for a falling object (as in Section 2.2), and a term explicitly dependent on G:

$$z(t) = \frac{1}{2}g(t^2 + \frac{\gamma t^4}{12}) + V_0(t + \frac{\gamma t^3}{6}) + X_0(1 + \frac{1}{2}\gamma t^2) + \mathrm{G\ f}(t)$$

where $\mathrm{f}(t)$ is a basis function describing the effect of the gravitational interaction between the source and proof masses. Unfortunately this was not reasonable because $\mathrm{f}(t)$ looked very much like a parabola; the correlation between the perturbation we were trying to measure and the effect of the local acceleration was strong (as is evident in Fig.2.2). For this reason the problem had to be posed with the differential nature of the data evident. We did this by folding all the information from drops with the source mass in both positions into one "big least-squares solution" (LSS).

The LSS had to convert the information of the observations (the position/time points for each drop), the superconducting relative gravimeter (SRG) data (essentially an acceleration value), and the gravitational signal of the source mass into a single form that would allow them to be compared. Least-squares fitting minimizes the total chi-squared error between individual data points and a fitting function. In our case the individual data points were position/time pairs from drop data. The fitting function was a fourth-degree polynomial describing the motion of a freely falling object in a simple gravity field (Eqn.2.10).

It is not immediately clear how all this information can be combined to generate a chi-squared value that depends on the choice of the fitting parameters. The problem was complicated by the many different relationships between the observations and the various fitting parameters. For example, $X_o, V_o$, and $g$ are local to the data within a single drop. On the other hand, the variable G, the offset from the SRG from the absolute local acceleration ($O$), and a drift parameter for the SRG, $D$[1] , were global to the whole problem. An individual datum is associated with all the other data of its drop in one way, in a different way with data sharing the source mass position, all the remaining data in yet another way. Even data within a single set is separated in time — environmental gravity signals change appreciably on a time scale of minutes.

The LSS began with the removal of the laser dither signal from the drop

---

[1] To remove environmental signals, data from a superconducting relative gravimeter (SRG) is included in the procedure. Unfortunately relative meters can only give information about changes in local gravity – an offset between the relative value and the absolute value must be included in the fit. Relative meters also suffer from small drifts, which must be fit for as well. See Sec. 3.3.

data. The dither of the laser signal (Sec. 3.1.2) correlated very weakly with G, which is why it was dealt with before applying LSS. Fitting the data of each drop for:

$$z(t) = \frac{1}{2}g'(t^2 + \frac{\gamma t^4}{12}) + V_0(t + \frac{\gamma t^3}{6}) + Z_0(1 + \frac{1}{2}\gamma t^2) + A\sin\omega_d t + B\cos\omega_d t$$

where $\omega_d$ is the dither angular frequency ($\approx$ 1200 Hz), allowed only the dither signal to be removed. Note that this "pre-cleaning" was only possible because the dither basis function was of such high frequency that it was nearly orthogonal to the other basis functions.

The fit for the dither provided starting values for g', $V_0$, and $Z_0$. These values were used to set up the design matrix of the problem. $g'$ was corrected with the acceleration value from the super conductor, $g_{\text{sc}}$, appropriate for the time of the drop. $g'$ was also corrected with the global values of the offset and drift:

$$g_{\text{effective}} = g' + O + Dt + g_{\text{sc}}$$

The design matrix also must include information about our gravity signal. This was included, for each datum, by integrating the equation of motion (Eqn. 2.11) with the global value of G. It was the position value returned by this integration that was used in the design matrix for the G parameter.

Since the base unit of information dealt with in the LSS was a single position-time datum and because there were more than 650 such data per drop, and more than 150,000 drops in our data sets, the least squares matrix was necessarily large. The matrix resulting from our set up had more than 16,000,000 observations and requires nearly 200,000 adjusted parameters. Dealing with such a large matrix requires greater addressing capacities than possessed by desktop computers — extra cleverness is required.

Because none of the parameters local to a drop were correlated with the equivalent parameters of other drops, the design matrix was sparse[2] . The matrix was therefore largely empty; it had a banded-block structure, in which the only non-zero elements of the matrix were in bands at its edges and in blocks along its diagonal. Algorithms developed to deal with sparse-matrices made the problem tractable – it could be solved in about two weeks with a desktop workstation [36, 37].

## 4.2 The Method of Parallels

A more intuitive method of extracting the value of G from the observed data exists. The method of parallels (MOP) was faster than the LSS, but included less information about correlations between the initial conditions of drops and the value of G. In MOP a theoretical prediction of the change in observed gravity due to the source mass was compared to a measured change in g.

MOP required that an assumed value of the constant of gravity, $G_t$, be adopted so that the magnitude of the source mass signal on the measured local acceleration could be predicted. The prediction, $\delta g_t$, was found by fitting parabolas to theoretical position-time curves[3] generated modeling the source mass in its two positions. The magnitude of $\delta g_t$ was linear in $G_t$ so it was easily related to an experimentally observed change in gravity, $\delta g_o$:

$$\frac{\delta g_t}{G_t} = \frac{\delta g_o}{G}. \tag{4.1}$$

Of course the fitting functions used to generate the prediction of the signal had to be the same functions used to fit the actual drop data.

It was only because G correlated so weakly with the other parameters of the

---

[2] Only the value of the constant, the value of the offset to the relative meter, and its drift were global to the whole problem.

[3] Describing the motion of the test mass, as generated in Sec. 2.2.

free-fall problem that MOP was successful. As we saw from the correlation matrices from the LSS[4] , the correlation between G and any other fitting parameter (used in the LSS) was less than 0.1. MOP didn't juggle all the information we had in a single least squares solution, but the information it dealt with was sufficiently independent to allow the solution to be partitioned. First the position/time pairs of each drop were fit for an acceleration value. Second an analysis of the acceleration values produced a $\delta g_o$ value. Third $\delta g_o$ and $\delta g_t$ were compared, producing a value for G. Because LSS and MOP produced highly consistent results, MOP was used in the final analysis.

### 4.2.1 Differencing Techniques

We used a variety of methods to extract the experimental $\delta g_o$ value from the data. The simplest way to calculate the difference was to subtract the average the value of the local acceleration measured with the source in its lower position from the average with the mass in the upper position. This method is not optimal; it does not recognize underlying time varying signals in the local acceleration resulting in increased scatter.

A second method that we used involved taking individual differences, as shown in Fig.4.1. This was essentially the same as the first method, but allowed identification of outlying difference values, so that they could be removed. With this method the differences we measured were not completely uncorrelated — each set of data was used to calculate two difference values. Therefore we had to be careful in our analysis of statistical uncertainty.

We used a third method to avoid the effects of linear drifts on the scatter of the differences (Fig.4.1). It involved estimating the drift of the local acceleration across three sets of data by averaging two consecutive sets that shared a common

---

[4] And qualitatively from self-consistency tests with MOP.

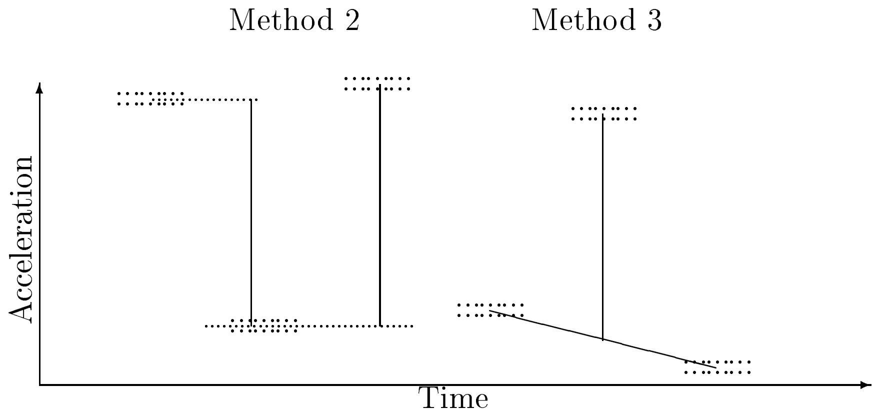

Figure 4.1: Two methods of calculating $\delta g_o$ given acceleration data. (:::::) represents a set of acceleration data with the source mass in either its upper or lower position. The vertical lines represent the measured difference value associated with the pair or trio of sets.

source mass position. By taking the difference of this average with respect to the intervening set (with the source mass in its other position), the effect of linear drifts on the differences was minimized. Method three had even stronger correlations between the differences than method two, for three difference values shared information from one set.

A statistically correct implementation of the third method was used in our final analysis. First uncertainty values were associated with the time and acceleration of each drop, allowing the importance of the information of each drop to be appropriately weighted. The uncertainty value was based on the chi-squared value of the parabolic fit to that particular drop. A line was fit, with linear least squares, to each pair of subsequent sets sharing a common source mass position. Then the weighted mean of the intervening set was removed from the value of the line at that time[5] . This system produced a statistically correct estimate for the error in each difference value. The final $\delta g_o$ was formed by the weighted mean

---

[5] There is no reason that the time of each drop cannot be weighted according to the uncertainty of the drop. Thus it was possible to associate a "weighted mean time," a single time best representing the data in the set.

value of these difference results, with an error estimate taken from the weighted mean standard deviation of the individual differences.

## 4.3 Dependence of $\delta g_o$ on First Fringe Fit

The methods of MOP and LSS destroyed a great deal of information. MOP reduced the approximately 96 billion position/time pairs of the experiment into a series of less than 2000 measurements of the experimental $\delta g_o$. These differences were then averaged to return a signal best estimate for $\delta g_o$. Yet it was possible to extract other information about the free-fall system. This section outlines an approach (using MOP) that I used to extract information about the position of the source mass with respect to the SOD position. In Secs. 3.1.1.2 and 5.1.2 an alternate "direct" measurement of the SOD is presented.

The gravimeter system recorded approximately 650 usable position/time for the test mass during each drop. By varying the set of data within each drop that was fit the SOD could be found by analysis of the dependence of $\delta g_o$ on the choice of the sub set. A reasonable manner of altering the subset was to change the first or last fringe that was fit. It was more useful to modify the first fit fringe (FFF) than the last fit fringe, because the effect of the acceleration parameter is most obvious at the start of the drop.

The $\delta g_o$ value extracted from the data had a very similar dependency on the FFF as the acceleration field of the source mass had on position. Imagine an acceleration field that contains a step increase occurring in the middle of the drop region (in the spatial middle of recorded data). As the FFF approaches this step, the extracted value of g will increase. As soon as the first fringe is beyond the step, the value of g will no longer change with the fringe number. Clearly the position of the step can be determined by analysis of the gravimeter data.

In a very similar manner the changing (in space) acceleration field of the source mass left a signature dependence of $\delta g_o$ on the FFF. By comparing theoretical curves, generated assuming different SOD positions, to the observed dependence, a best-agreement SOD position was found[6] . Fig. 4.2 shows the quality of agreement for different SOD positions on different days of the experiment. By scaling the best-fit theoretical curve, generated at the extracted SOD, to the data (with a single multiplicative factor), a scaling of theoretical value of G used in our models could also be made.

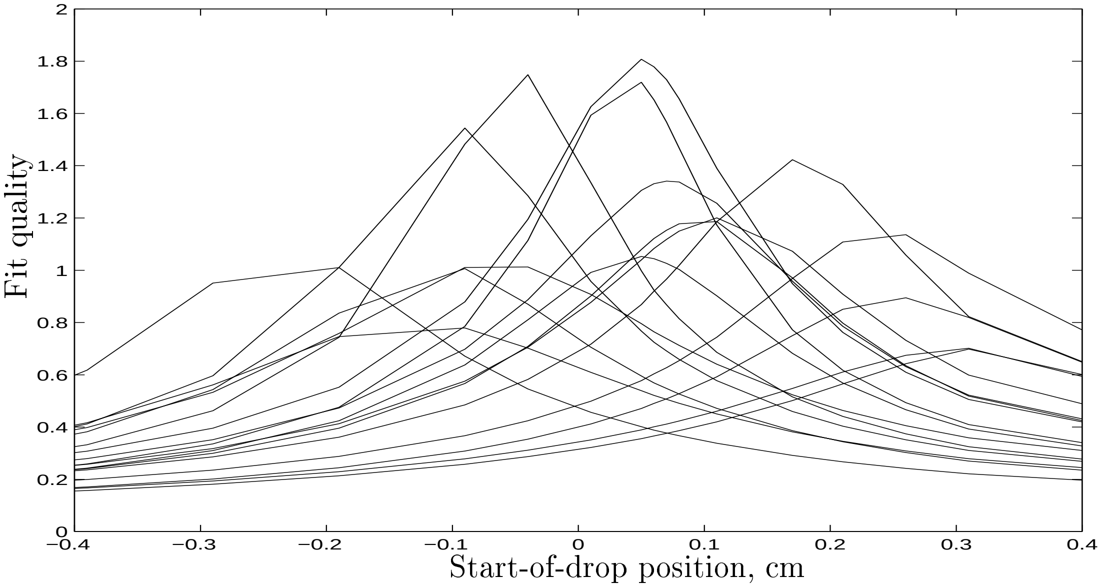

Figure 4.2: Here the quality of a fit of theoretical data to experimental data is plotted. The curves that were fit represented the dependence of $\delta g$ on the FFF in the position/time data recorded by the gravimeter. Each line plotted here represents the quality of the agreement between theory and experiment, for a particular day of the 1998 experiment. The weighting/quality assessment was based on the chi-squared value in a linear least squares routine that fit the theoretical curve (at a given start-of-drop position) to the experimentally derived curve. The fit was in one-dimensional (for a scaling factor).

Noise in the data results in greater and greater deterioration of the $\delta g_o$ value extracted with less and less data fit [7] . This constrained the region over which the

---

[6] In the free-fall measurement the translation of the source mass between its upper and lower positions was very well known compared to the mass's position relative to the SOD.

[7] There are two reasons for this deterioration. The first is that the statistical uncertainty

FFF was varied to the fringes between the earliest usable data in each drop and the fringe where the uncertainty in $\delta g_o$ became large. We were fortunate that this sub-set encompassed the region where the second derivative of $\delta g_o$ with respect to the FFF was greatest. If the second derivative were small the correlation between the scaling factor for the theoretical G and the SOD position would increase, as would the uncertainty in the best-fit SOD value.

This method to find the SOD position was applied to two independent data runs. In the first run the extracted SOD position was consistent with the "direct" measurement (Sec. 5.1.2). In the second run, however, the two values were inconsistent, disagreeing by nearly 2 mm — about 4 standard deviations. I attribute this discrepancy to the fact that in the second data run changes in the shaft-encoder voltage were monitored. Conceivably, as in quantum physics, the observer affected the observed, and changed the SOD position. Thus the extracted SOD position was used for the final determinations of G in both data runs.

The extracted SOD value is more appropriate than the direct value. Examination of the values of G obtained for a set of FFF values for the two different SOD positions results in Figure 4.3. There is no physical dependence of G on FFF, but the directly reference value suggested that there is — because the direct reference was incorrect. Note that the G values extracted for FFF about fringe 18 agree well between the two SOD positions. This agreement is due to our lack of sensitivity to positioning errors, and is a consequence of the extrema of the source mass field. In some sense the positioning error doesn't matter if a reasonable FFF is chosen for analysis.

To check for a systematic drift or signal in the SOD position during a data run (conceivably due to ball wear, Sec. 5.2.5) the best-agreement SOD position

---

(inversely proportional to $\sqrt{N}$ where $N$ is the number of data points fit) increases. The second is that the correlation between g and the other fitting parameters increases as the beginning of the drop is excluded from the fit.

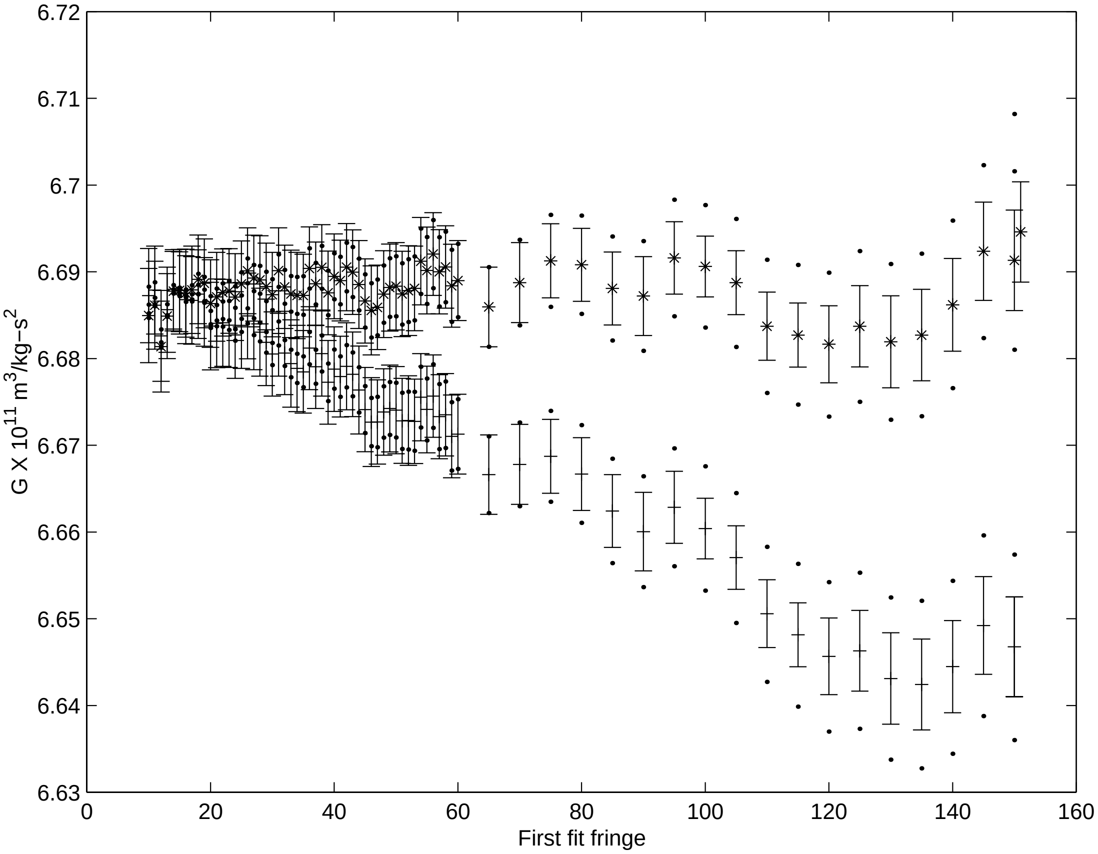

Figure 4.3: The value of G extracted from the data as a function of the first fringe fit. The points marked with asterisks are generated using the SOD value extracted from drop data. The points marked with crosses use the directly referenced SOD position. The small points bounding each set of error bars show the G value using the appropriate SOD $\pm 1\sigma$.

for each day is plotted in Fig.4.4. There is no significant drift. There is also no correlation between the value of G produced by a day of data, and its best-fit SOD.

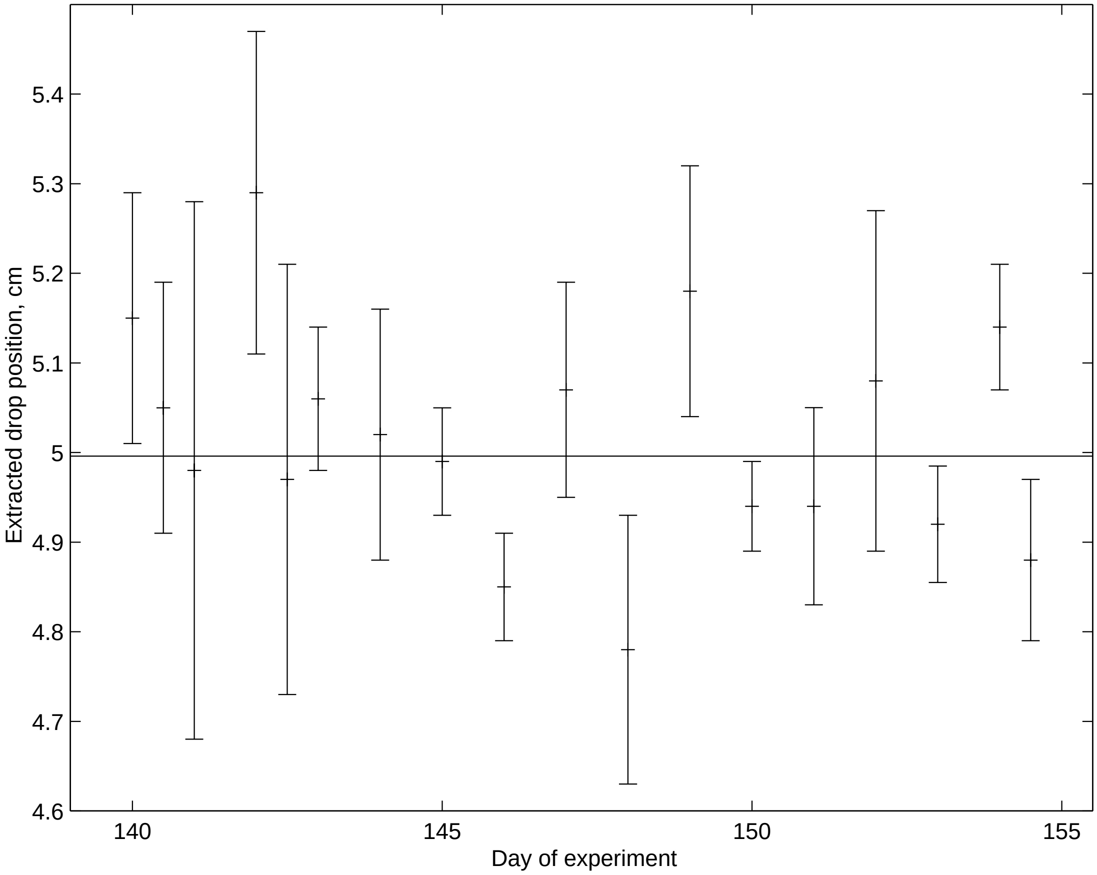

Figure 4.4: The start-of-drop position extracted from each day of the 1998 experiment. The error bars are based on the chi-squared agreement of the least-squares-fit of the data to theory. The error bars are used only for weighting purposes. The horizontal line shows the weighted mean position.

# CHAPTER 5

# ERROR ANALYSIS

All mechanisms that introduce errors to the G experiment lead to one result — the breakdown of the connection between the theoretical model of the experiment and its physical reality. The careful calculation, determination, and, in some cases, estimation of the magnitudes of the errors associated with our experiment is of the utmost importance in describing our results. Because the standard used to evaluate the level of agreement between experimental results is the number of standard errors between their values (the t-test), the uncertainty associated with our results will affect the way we perceive agreement levels.

A discussion and summary of the main sources of error in the free-fall experiment is in presented in Section 5.1. I have chosen to present some systematic error sources in depth in section, Sec. 5.2. Some techniques that we have used to search for indicators of systematic errors are presented in the last section of this chapter. The "hard" presentation of significant errors, including the values used in determining their magnitudes is provided in Appendix B.

## 5.1 General Error Analysis

### 5.1.1 Common mode errors

Many error signals fall into the class called "common mode". These signals affect the absolute accuracy of the FG-5 system, but have little impact on its differential precision. Mechanisms that influence the absolute accuracy of the gravimeter are easy to imagine—and become even more so when you start trying to think of errors capable of acting on the gravimeter differentially.

Consider the effect of the building that housed the experiment. This building certainly affected the acceleration of the test mass, probably at the level of 5 $\mu$Gal in the common mode. Yet we don't expect it to introduce a change our measured source mass signal on a level greater than 5 parts in $10^9$ because it was on this level that the differential equation describing the motion of the test mass was invalidated. A general list of common mode effects that are not important in the differential mode includes:

- gravitational attraction of the co-falling chamber
- drag effects of residual gas in the vacuum
- light pressure of the laser sensing the test mass position
- forces due to magnetic field of the earth
- gravitational attraction of stationary apparatus
- slowly varying gravitational effects due to:
  —Lunar Tides
  —Earth Tides
  —Ocean Loading
  —Atmospheric pressure changes
  —Water table changes or snow fall
  —Temperature drift effects
  —Continental uplift
- slowly varying machine dependent drifts:
  —Laser verticality
  —Laser frequency or time standards drifts

—Laser intensity changes

—Vacuum pressure changes

Although common mode errors don't bias our results, they could strongly influence the scatter in the free fall measurement if they modulated the g-signal on a time scale close to the source mass modulation. Two data runs with different modulation rates were made. The first, in 1997, modulated the source mass every twenty minutes. During the first 17 minutes of each "set", 100 drops were measured with 10 seconds between each drop. In a second data run in 1998, the source mass was modulated at 11 minutes, with 90 drops per set (5 seconds between drops). Scatter in this second data run would only be strongly sensitive to common mode signals changing at periods less than about 30 minutes.

### 5.1.2 Positioning Errors

Errors made in positioning the source and proof masses resulted in systematic errors that were not ameliorated by the differential nature of the experiment. The analysis of these positioning errors is divided into a treatment of the source and proof masses separately.

Errors in the source mass vertical position with respect to the start-of-drop (SOD) biased the calculation of the acceleration experienced by the test mass and our value of G. This type of errors was introduced by wear in the support nuts of the source mass, by inaccuracy in referencing the mass to the vacuum chamber, and uncertainty in the SOD position within the chamber. Because we operated at the extrema positions of the source mass field, however, positioning errors were not a major source of error in the experiment. The uncertainties associated with the source mass positioning issues are fully presented in Sec. B.1.1, in Appendix

B. The net effect of vertical positioning errors was only 10 ppm.

Error positioning the tungsten cylinders within the source mass was a much more important source of uncertainty. Because the radial position of the large tungsten cylinders was determined by the locating lip of the sandwiching plates (which allowed some clearance) the cylinders' radii from the drop were not absolutely defined. The plate that supported the tungsten mass distorted under their weight producing additional uncertainty. Density inhomogeneities, so carefully dealt with in Sec. 3.2.1, had the same effect as misplacing elements of the source mass. These sources of error were responsible for nearly 100 ppms of uncertainty.

The complicated proof mass, which underwent free fall motion, was a greater source of positioning errors than the source mass. Most important was the radial position of the proof mass, which depended on horizontal velocities (that could never be made identically zero), and the centering of the proof mass within the dropping chamber. Estimates of radial positioning errors were made with a simplified model of the proof mass that was increasingly miss-positioned horizontally. The variation in acceleration signal with the radial offset of the proof mass from the symmetry axis is roughly quadratic. Figure 5.1 displays the effect on the vertical acceleration of the proof mass by moving it off the axis of symmetry of the source mass.

The proof mass optical center was "directly" referenced to the source mass only through a long chain of measurements:

- Optical center of corner cube to tungsten balls (within test mass)
- Tungsten balls to tungsten vees (test mass –> co-falling chamber).
- Tungsten vees to bottom of co-falling chamber.
  (within co-falling chamber).
- Co-falling chamber to stop at bottom of dropping chamber.

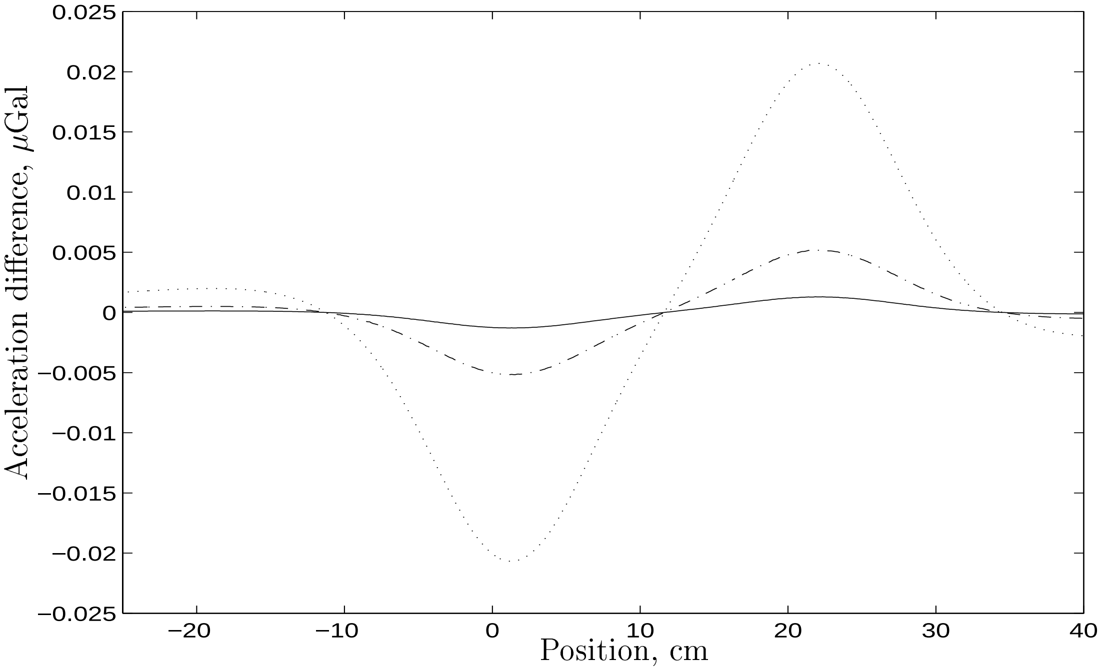

Figure 5.1: Difference in vertical acceleration (due to the source mass) sensed by a simple proof mass (8 cm long hollow cylinder with 1 cm diameter and 1 mm wall) falling on axis and (—) 0.1 cm, (·–·) 0.2 cm, (· · ·) 0.4 cm off axis. Position is with respect to the source mass. Note that radial position errors have precisely the same effect as a scaling of G.

assembly (via shaft encoder servo).

- Gravimeter bottom stop to bottom of gravimeter vacuum.

  (within drop chamber) chamber.

- Bottom of dropping chamber assembly to top of lower flange on

  vacuum can.

- Top of flange to bottom of the source mass

  in its lower position.

These measurements were made directly[1] , with the vacuum chamber open to air. This trail of references added error at every step. Alternatively information about

---

[1] For the most part. The shaft encoder travel to the SOD was interpolated from the diameter of the drive pulley and calibrations of the shaft encoder output.

the position of the test mass could be extracted from the data (as in Section 4.3).

In a data run in 1997 experiment the two independent determinations (extracted and directly measured) of the position agreed well, but in another run in 1998 they were not consistent. The set-to-set variation in the position, as measured by the shaft-encoder, was the same magnitude as this disagreement (in the 1998 experiment). Possibly the system that was used to monitor the shaft-encoder voltage throughout the 1998 measurement may have affected the system. For these reasons we adopted the position value extracted from the data (Sec. 4.3 includes a discussion of why this was reasonable). Using the value given by the "direct" measurement changes the final value by less than 1/2 sigma.

### 5.1.3 Modeling Errors

Errors in the measurement of masses contributed weakly to our final error estimates. The direct measurement of the masses of the tungsten cylinders and the two aluminum plates was the largest source of error. Buoyancy corrections were applied for these objects (Sec. B.3.1). The smaller components of the source mass (nuts and bolts) could be weighed with higher precision because of their small mass. The total uncertainty associated with errors of this type was about 40 ppm.

Although the total mass of the test mass had no bearing on the acceleration difference we measured, its mass distribution did. Thus it was important that the relative densities and positions of the various components of the test mass were correctly modeled. Although there was essentially no error introduced during the modeling of the source mass[2] , modeling the test mass was very difficult because of the complexity of its design. Errors in the relative masses ($\approx 0.05$ g) and positions

---

[2] Certain approximations were made during the modeling of screw threads, bolt heads, and groups of bolts, as discussed in Appendix A. These approximations were very good.

($\approx$ 0.01 cm) of the components of the proof mass contribute about 90 ppm to our uncertainty.

Over the course of the free fall experiment the tungsten balls that supported the test mass experienced some wear. This introduced three errors: Firstly a change in the relative mass of the balls to the rest of the test mass, secondly a change in the mass distribution within the balls themselves, and thirdly a change in the SOD position. These are all very small errors, and are discussed in Sec. 5.2.5.

### 5.1.4 Numerical Techniques

A primary assumption of the free-fall method of measuring G was that the theoretical framework we built was accurate enough to describe the experiment to better accuracy than it could be carried out. Position versus time data for the test mass lacked meaning if we could not relate them and their variations to the source mass and G. There were many levels at which our numerical approximations may have differed from reality. I think it reasonable to start the discussion of possible errors with the integration over the source mass.

The Romberg quadrature algorithms we used to evaluate the integrations over the source and proof mass incorporated an error estimating functionality (Sec. 2.1). We specified that the individual integrations return a value good to better than 1 part in $10^8$. The individual integrations agreed at this level with analytic test cases. The error introduced by this limit of accuracy was overshadowed by the approximation we made in integrating over an interpolation field (Sec. 2.1). By specifying a sufficiently dense grid, however, this source of error could be controlled to arbitrary precision. The final grid precision we used corresponded to an uncertainty of 20 ppm.

To reduce the interpolation field to a two-dimensional grid we assumed that the gravitational field produced by the source mass was cylindrically symmetric. This was very good approximation to a level of 20 of ppm.

### 5.1.5 Spurious Signals

Thermal and magnetic effects were among the hardest sources of uncertainty to quantify. These sources of discussed in depth later in this chapter, within Sec. 5.2. Here a very brief discussion is included.

We had to perform secondary experiments to get the magnitude of signals arising from these two areas. A test for thermal effects was made by placing modulated heat sources around the gravimeter, recording the power incident on the gravimeter and the resulting g signal. The modulation frequency matched the modulation rate in the 1997 experiment, 20 minutes per set. This would overestimate the thermal signal in a 1998 data run in which only 11 minutes were allocated per set.

We bounded the magnitudes of the magnetic signals both by calculating the effect (for eddy current damping during the drop) and by experimentation (for the force of the magnetic AC signals). The theoretical calculations were based on measurements of the DC magnetic field in the region of the dropping chamber and on the susceptibility and (simplified) geometry of the source and test masses. The experiment is presented in Sec. 5.2.8 on page 96.

### 5.1.6 Contaminated Data

There were several ways data could be ruined. Earthquakes resulted in huge scatter in the measurement of acceleration values. When the scatter was large enough (several hundred $\mu$Gal ) the source mass signal could be completely swamped out. Occasionally fringes were miscounted, ruining individual drops (Sec. 5.2.9, pg. 101). Rarely the laser lost its frequency lock, resulting in a position measurement made with a uncalibrated "ruler".

Drops contaminated by missed fringes were easily identified and removed from the set of drops used in the differencing. Some unreasonable data was not so obvious. The criterion that we chose to remove this data was simple: Drops that produced g values more than 3 standard deviations from the mean g-value for the particular set were removed.

Our treatment of earthquake contaminated data was even more casual. Earthquakes were removed by eye. Generally just the beginning of the earthquake was removed, leaving several sets with large scatter due to the motion of the super spring. The difference values produced from these sets were "automatically" associated with greater uncertainty with the differencing algorithm discussed in Sec. 4.2.1. Entire earthquakes were left in the data to test the method, and no significant change ($> 0.2\sigma$) in any days' G result was observed. Figure 5.2 summarizes our feelings about earthquake contaminated data.

### Totaled Non-statistical Error Estimates

Table 5.1 presents a summary of the major systematic error sources of the free-fall experiment. The table is split into two sections for the two data runs because some errors were better controlled in the 1998 run.

## 5.2 Sources of Systematic Error

There are many sources of real gravity changes that are sensed by free fall and super conducting gravimeters (tides, atmospheric signals, water table changes...). These sources do not complete the set of mechanisms that influence measured gravity; instrumental errors are sources of false signals that can have equal bearing on the results of the acceleration measurement as real gravitational effects. All the systematic non-gravitational signals we have discovered in the

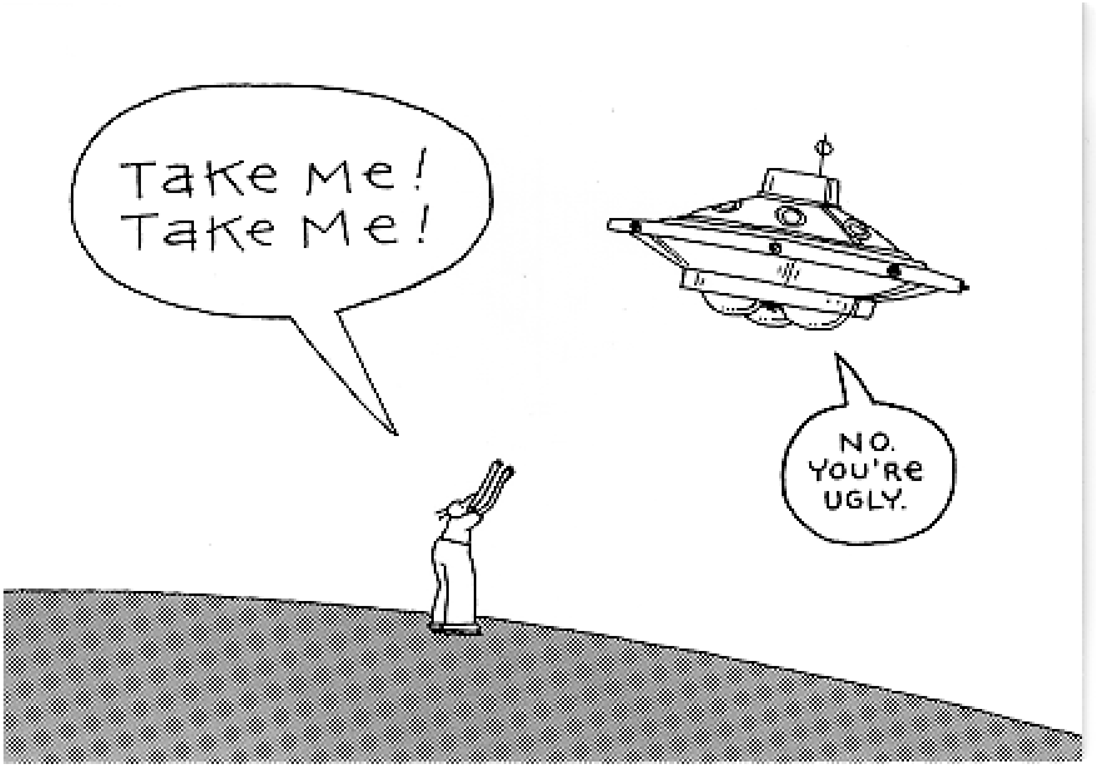

Figure 5.2: A Hallmark postcard – commentary on our data analysis technique? Because our results don't change by more than a tenth of a standard uncertainty whether we take or leave the little fellow, we don't think it much matters.

| Source of Uncertainty | 1997 Error | 1998 Error |
|---|---|---|
| *Positioning Errors* | | |
| Vertical positioning | 10 ppm | 10 ppm |
| Radial positioning | 85 ppm | 60 ppm |
| Internal positioning | 85 ppm | 45 ppm |
| RSS TOTAL: | 120 ppm | 75 ppm |
| *Modeling Errors* | | |
| Granularity of mass models | 52 ppm | 52 ppm |
| Symmetry Assumption | 20 ppm | 20 ppm |
| Interpolation Density | 20 ppm | 20 ppm |
| Modeling | 90 ppm | 90 ppm |
| Source mass density variations: | | |
| Point mass | 60 ppm | 60 ppm |
| Linear | 50 ppm | 50 ppm |
| Quadratic | 60 ppm | 60 ppm |
| Angular | 25 ppm | 25 ppm |
| RSS TOTAL: | 145 ppm | 145 ppm |
| Thermal Signals | 60 ppm | 60 ppm |
| Airgap | 75 ppm | 75 ppm |

Table 5.1: A table of the magnitudes of the important error sources. Error estimates are separated between two data runs in 1997 and 1998. Generally the error estimates are the same or better in the 1998 run because this run incorporated more robust support plates for the source mass and more precise alignment of the source mass and dropping system.

free fall G-measurement were consequences of differential modulation of these mechanisms.

This section contains discussion of some sources of error in the measurement of the local acceleration, and the manner that the G experiment might modulate the errors to create systematic bias in our results. The subsections are arranged by the magnitude of the uncertainty due to the mechanism. One or two of the subsections discuss broader subjects than a single error source (Secs. 5.2.9 and 5.2.10 ).

More complete discussion of all the error sources (including common mode) in the free fall gravimeter may be found in [30, 24, 38]. Only errors springing from the FG-5 system are discussed here because we don't expect (or see evidence of) any systematic connection between the free fall measurement and the super conducting system.

### 5.2.1 Air Gap Modulation

Because the dropping chamber is in high vacuum whilst the rest of the gravimeter is in air, an air-vacuum interface exists between the arms of the interferometer. The index of refraction of air is slightly larger than the index of vacuum, so motions of the interface (the "airgap") result in phase shifts of the fringe signal[39, 38]. If the interface moved upwards by an amount $\delta$ the laser beam would pass through a distance $\delta$ where vacuum had been replaced by air. This would result in a phase shift mimicking a motion of the test mass upwards, away from the interface. If the interface moved downwards, there would be a corresponding false motion of the proof mass towards the interface.

At the start of the drop the co-falling chamber is accelerated quickly from rest jarring of the dropping chamber and introducing a vibration in the airgap that couples into the g measurement in just this way — these vibrations necessitate the separation of the interferometer/spring system from the dropper least the super spring be excited. Figure 5.3 is a plot of the vertical position of the interface as a function of time averaged over 90 drops.

This noise signal is systematically linked to the drop — it is triggered by the drop motion. Power spectral analysis of the motion (Figure 5.4) shows that the airgap motion might be modeled as a sinusoid with frequency 63 Hz (a very bad approximation). A sinusoidal motion at this frequency has a small but non-zero correlation with the acceleration parameter of the linear fit for gravity.

The effect of the airgap modulation was not completely common mode be-

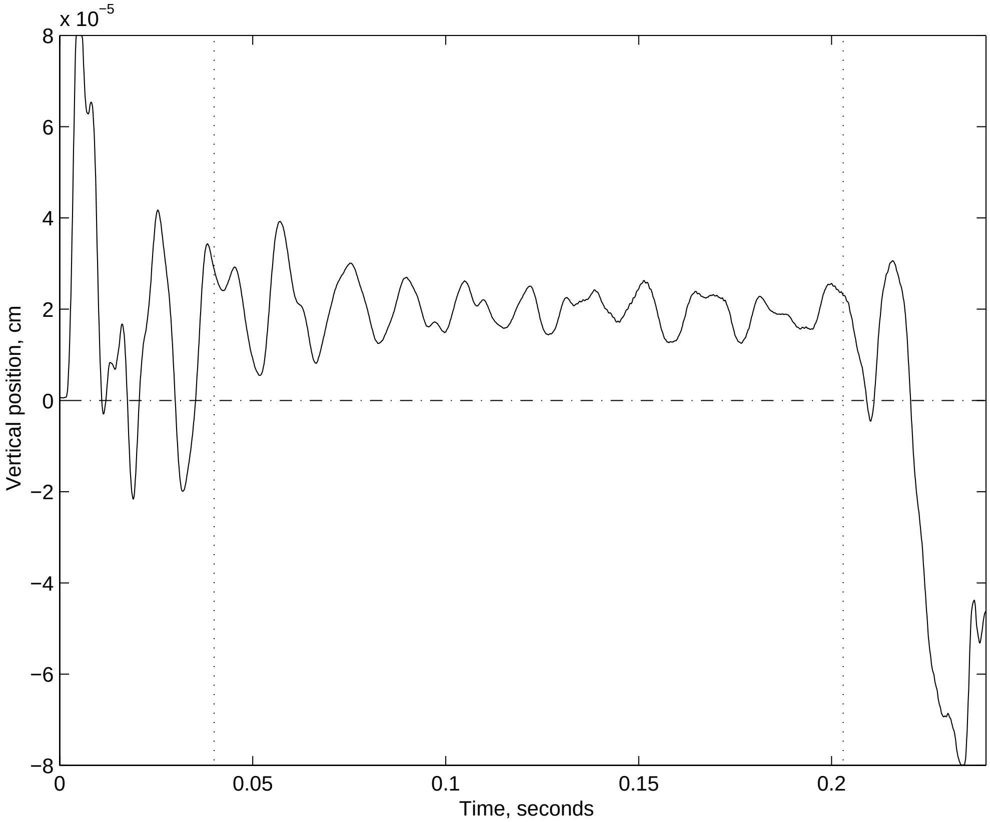

Figure 5.3: Vertical motion of the air-vacuum interface between the dropping chamber and the interferometer. This trace was averaged over 90 drops of the test mass. The two vertical dotted lines represent the typical start and stop positions for the fit for local acceleration. Note that the mean position of the interface is non-zero during the drop because the test mass and its co-falling chamber became weightless during each drop causing the rest of the tripod/dropping assembly to jump up on its spring-like legs. Because the test mass is in free fall at this point other effects of the weight change are unimportant.

cause the motion of the interface was affected by a damping force dependent on the source mass position. In its lower position the source mass was placed close to the lower flange of the dropping chamber, resulting in an increase in air-damping of the motion. In this position the source mass was near to the ion pump and its quickly-changing magnetic field. The ion pump magnets (which were rigidly connected to the dropping can) induced eddy currents within the conducting source mass. This magnetically damped the airgap motion differentially.

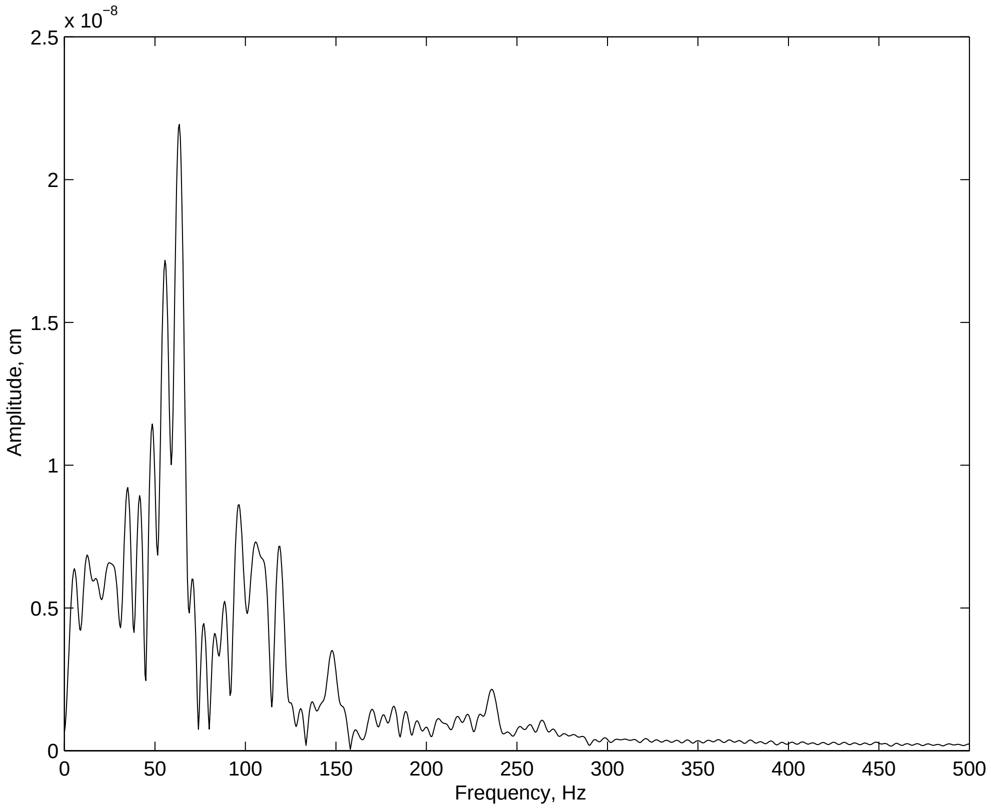

Figure 5.4: The amplitude spectrum of the airgap motion – the square-root of the power spectrum. The data analyzed was averaged over approximately 11,000 drops. The analysis included 0.24 seconds of data following the drop trigger. Thus it incorporates data that is not seen in the fit for gravity.

We measured the motion of the interface throughout a data run in 1998. A split-photo diode and high-intensity LED were supported by a rigid aluminum tube bolted to the lifting assembly. A knife edge bolted to the top of the dropping chamber blocked some of the light (from the LED) from one half of the photodiode. The whole arrangement was shielded from stray light by a telescoping cover, insuring that the source mass position would not directly influence the measurement.

We attempted to model the effect of the airgap by fitting a parabola to the apparent test mass motion that would have been introduced by the interface vibrations:

$$z_a = 2(n-1)z_{ag} \tag{5.1}$$

where $z_a$ is the apparent motion of the test mass, $z_{ag}$ is the actual motion of the air/vacuum interface, and $n$ is the index of refraction of air in Colorado (1.00026). The factor of two is included because the laser beam passed through the air/vacuum interface twice, once in each direction. Einstein said “Everything should be made as simple as possible, but not more so.” Unfortunately Equation 5.1 crosses the line of proper simplicity.

We can compare the “expected apparent” proof mass motion, the $z_a$ of Eqn. 5.1, to the residuals of the fit to drop data, which are roughly equivalent to a “measured apparent” motion[3] . The agreement between the expected and actual motion would be a good measure of the correctness of the simple model. Figure 5.5 contains such a comparison. Although the simple model agrees well (except for a scaling factor) at the beginning of the drop, the model does not successfully describe the apparent motion throughout the drop.

The scaling factor might be due to our assumption that when the air/vacuum

---

[3] The measured apparent motion, as recorded by the residuals to the fit, would naturally have all parabolic components removed.

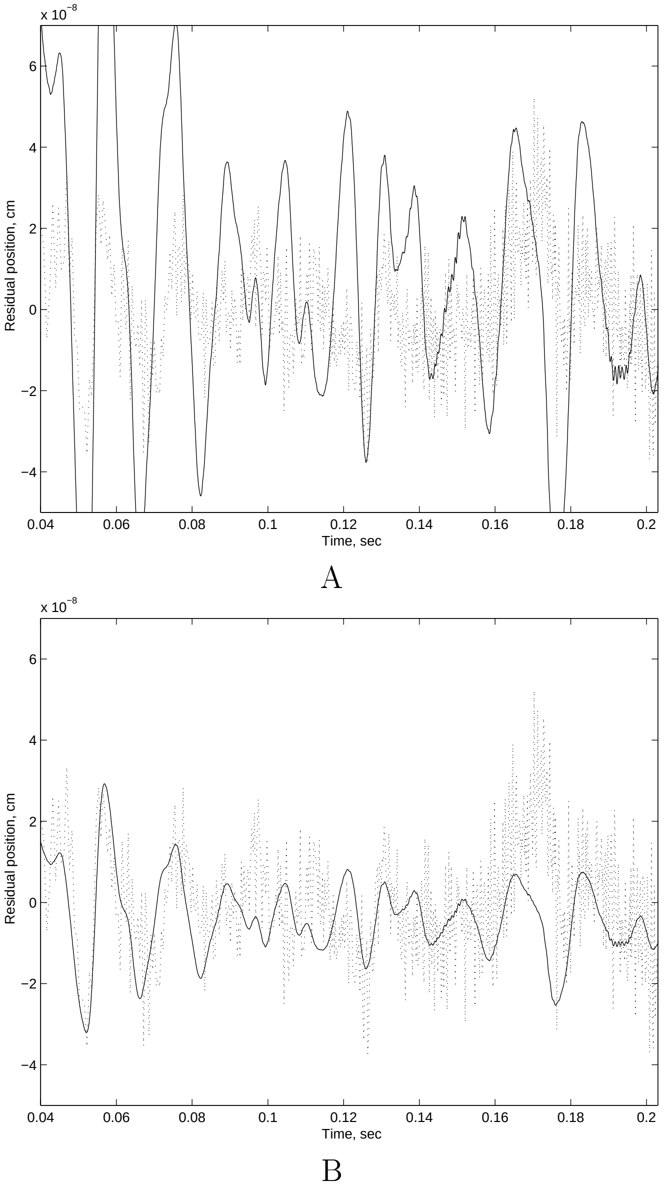

Figure 5.5: Comparing the expected false motion of the test mass arising from airgap motion to residuals from the fit for g. The solid curve is the expected signal, calculated as in Equation 5.1 from the measured motion of the airgap averaged over 90 drops. The dotted line is the residuals to the fit of the same 90 drops. A) The modeled motion is scaled according to the model. B) the modeled motion is scaled for best agreement with the residuals.

interface moved the displaced air was not compressed but only displaced from the laser path. This assumption might not be valid. The index of refraction of air is directly proportional its density, so unless air was moved out of the path of the laser there would be no phase error. This might not have occurred, for example, in a sealed column of air, where one end was a vibrating plunger. The degree that the air was being compressed rather than displaced would be indicated by the measured signal that is seen in the residuals.

I cannot explain why the model appears reasonable at the beginning of the drop, up to about 0.08 seconds, but not for other portions of the drop. This disagreement was significant. Fitting the expected apparent motion, $z_a$, with a parabola to extract an acceleration correction for each set of data gave very unexpected results. The corrections were very close to sinusoids and consistently (day to day) had the same period (about an hour and a half) and amplitude (about $1.5\mu$Gal ). Examination of the airgap data showed that phase shifts in the airgap motion occurring around the middle of the drop were responsible for this signal. We have no idea how the phase shifts were modulated in such a way as to produce the sinusoidal time dependence. Clearly, however, the actual acceleration data recorded by the gravimeter did not exhibit any such underlying signal.

To find out if any useful information about the magnitude of the differential airgap error source could be extracted from the data, I added a weighting function to the model to decrease sensitivity to the less reasonable information. I fit this weighted model (Fig. 5.6) with a parabola in the same way as before. The correction values extracted from the weighted model were much more reasonable. When I removed the acceleration corrections for each set from the actual measured values of g the set-to-set scatter in the g-values decreased slightly. This showed that there was some correspondence between the information in the airgap motion and the data recorded by the gravimeter.

At this point I processed the airgap corrections for a $\delta g$ correction, by using difference method two (Sec. 4.2.1). This introduced a new problem, however. The magnitude of the computed corrections to $\delta g$ and g was highly dependent

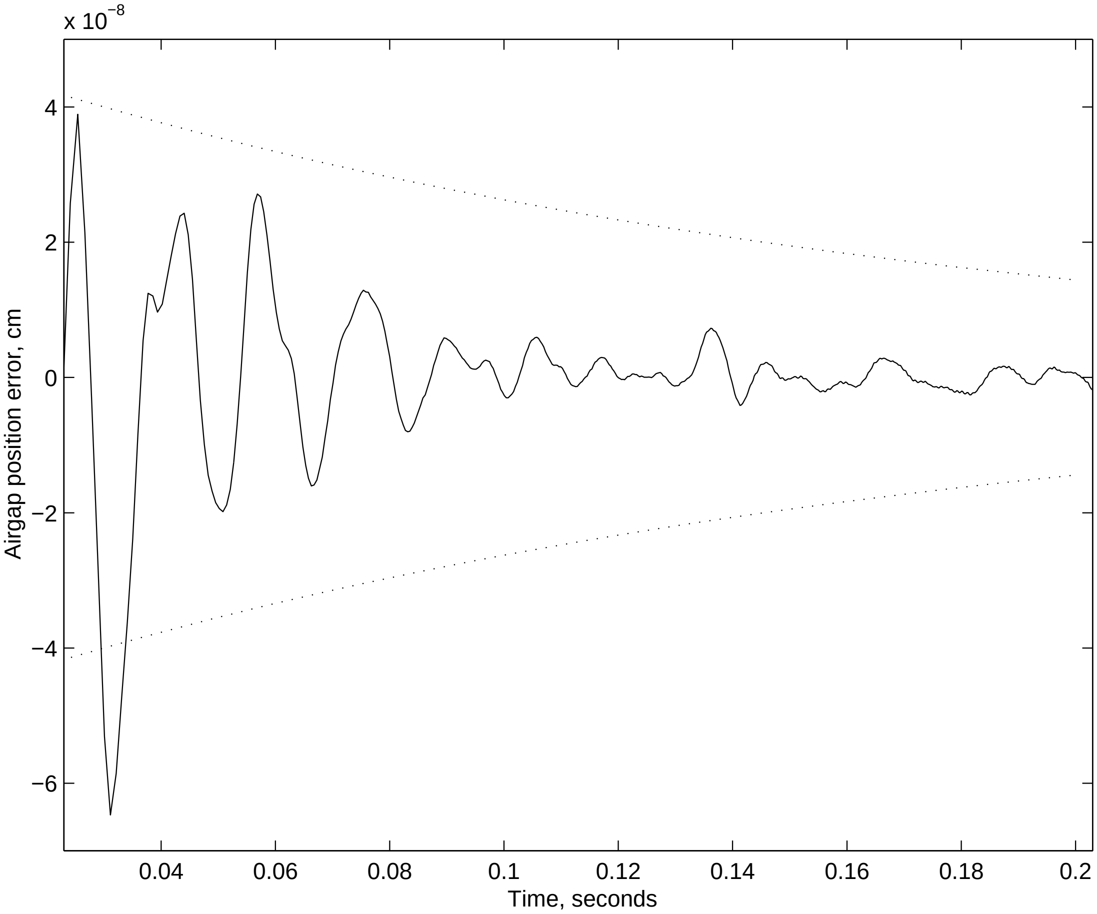

Figure 5.6: The weighted expected false position signal of the proof mass due to the airgap vibration. The dotted lines represent an exponential weighting of the airgap data. This weighting served to decrease the influence of the airgap data at the end of the drop.

on the weighting function used to curb the disagreement between the theoretical and observed airgap signal. How was the correct damping function to be found? Because the airgap signal accounted for a very small portion of the scatter in g-values, it would very difficult to test different damping coefficients to find a "best fit".

To avoid this dependence on the weighting function I assumed a single damping coefficient and calculated the correction to $\delta$g as a function of the first fringe fit (FFF). This is exactly analogous to the work in Sec. 4.3. One reason this was a good idea is that parameter we modified (the first fit fringe) only varied in a range where the agreement between the theoretical airgap motion agreed well with that observed in the residuals. This gave an expected correction to our data as a function of the FFF: $\delta g_{\mathrm{a}}$(FFF). This curve, which looked roughly like a sinusoid with a constant offset from zero, was, in turn, compared to the residuals of the $\delta g_{\mathrm{o}}$ as a function of FFF (obtained from the gravimeter data with the theoretical dependence of $\delta g_{\mathrm{o}}$ on FFF removed). Figure 5.7 shows the two curves. One is derived from the free fall data (we know our models of the free-fall motion are very good). The other comes from airgap data (with a questionable model), scaled to match up.

Now the trouble was that the residual to the observed dependence of $\delta g_{\mathrm{o}}$ on FFF would have no information about a net bias — any mean value or offset would have been removed with the theoretical curve. Our best estimate for the bias was the offset as calculated with the airgap information, because our result was averaged over the $\delta$g values for each start fringe (Discussed in Sec. 6.1.2).

To summarize up to this point: We have a model for the airgap's effect on gravity as measured with the FG-5. This model unfortunately incorporates a (to this point) arbitrary weighting function that strongly influenced the calculations of the magnitude of the airgap signal. We have found a way to compare changes in the theoretical airgap signal as a function of FFF (looks like a sinusoid in FFF) to actual observed anomalous changes in $\delta g$ as a function of FFF (which also looked something like a sinusoid in FFF). Since we can only compare changes in these two signals as a function of FFF, there can be no direct comparison of the bias of the airgap signal. Of course if we could extract the bias from the free fall data directly, we would never have to measure the airgap motion independently. Thus the bias must be taken from the airgap motion and model.

By calculating different $\delta g_{\mathrm{a}}$(FFF) curves using different damping functions,

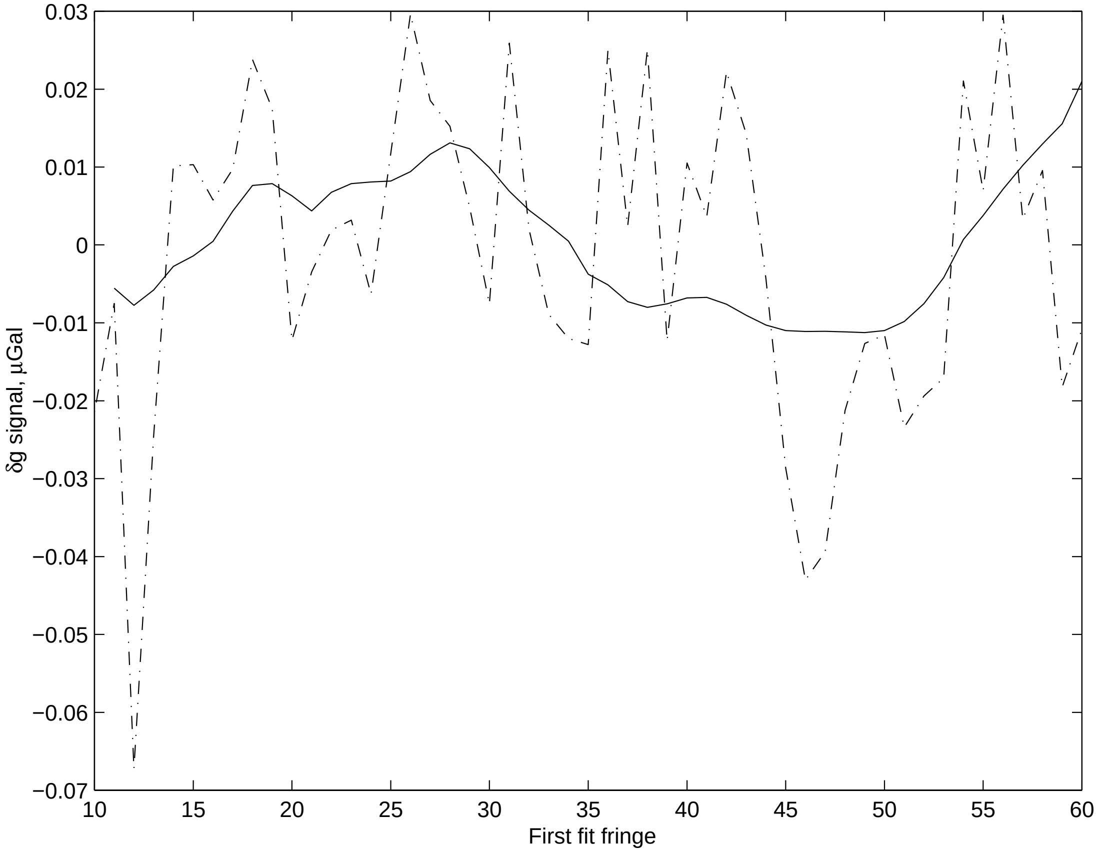

Figure 5.7: Scaling the theoretical $\delta$g correction derived from airgap motion data. (–·–) $\delta$g as a function of start fringe from free-fall data, with theoretical value removed. (—) $\delta$g as a function of start fringe from airgap data, and scaled for best agreement with the free-fall data. An offset has been removed from both curves. An additional offset has been removed from the airgap derived curve as part of the fit.

I was able to show that the bias in $\delta g_{\mathrm{a}}$ was linearly dependent on the amplitude of the sinusoid. We were able to extract from free-fall data the amplitude of the sinusoid, and thereby fix the bias value. The important point is that I was able to show that the calculated airgap systematic bias, calculated in this way, was independent of the choice of damping function used in the model.

In this convoluted way the effect of the airgap on $\delta$g was seen to be 0.006 $\mu$Gal with an uncertainty (derived from the fit) of 0.0005$\mu$Gal. The whole airgap motion caused approximately a 1 $\mu$Gal shift in the absolute value of g extracted from the drop data. This means that the source mass modulates the magnitude of the vibrations by about 1%. An additional measurement strengthens these conclusions. By integrating the power spectra density calculated from the airgap motion an estimate for the power of the motion is made. By averaging the airgap motion for the mass in upper and lower position, and then taking the difference, the change in power between the two positions could be calculated. This measurement showed that the differential motion was 1% of the power of the net motion, as expected from the model. Figure 5.8 is a plot of the relative motions of the airgap.

Because of the weakness of the model the entire 0.006 $\mu$Gal effect was adopted as the error estimate arising from differential airgap damping (also, a correction of this magnitude is made). In the 1997 experiment the airgap motion was not measured, so we can't use this method for that data. We do know that the damping was smaller in the 1997 experiment because the source mass was not placed as close to the gravimeter as it was in the 1998 experiment. Thus an error estimate of 0.006 $\mu$Gal (75 ppm) was adopted for the airgap effect in that run, too.

### 5.2.2 Thermal Signals

The source mass had a large thermal mass so it did not readily change temperature. Therefore it acted as heat reservoir and could introduce a thermal signature into the signal we were trying to measure. The source mass position could thermally couple into the gravimeter in two ways. The mass could either carry a thermal signature (due to the temperature gradient of the air in the room) and heat or cool different portions of the vacuum can or ion pump, or it could block radiation incident on the gravimeter and thereby perform a cooling function. The second mechanism is unimportant in the free fall measurement because no

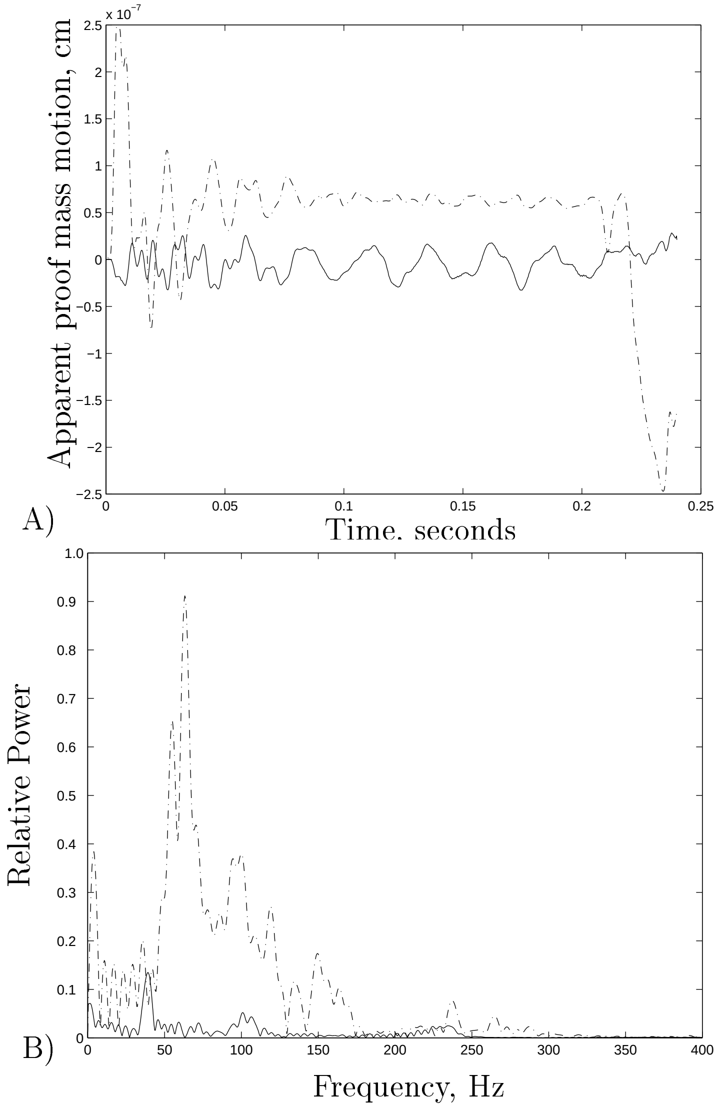

Figure 5.8: Comparing the net airgap motion to the difference in motion between the two source mass positions. The motion has been averaged over all the airgap data of a two week data run in 1998 (approximately 170,000 drops). A) Airgap motion: (–·–) Net airgap motion. (—) Difference signal, multiplied by a factor of 10. B) Amplitude spectral density of the airgap motion. (–·–) for the net motion. (—) for the differential motion.

significant localized sources of infrared radiation were located close to the system.

Thermal gradients can cause large shifts in acceleration measured with the FG-5 gravimeter. A thermal gradient creates a pressure gradient (in the residual gas of the vacuum system) across the proof mass. This gradient results in a buoyant force on the test mass. Niebauer *et al.* [38] cite a coefficient of 0.40 $\mu$Gal/$^o$C over the length of the proof mass. The temperature at the surface of the proof mass is also related to the "kick" that a gas molecule bouncing off the surface is given. If the upper and lower portions of the proof mass are at different temperatures there would be a greater transfer of momentum and energy in one direction than in the other, causing a net force on the test mass.

It is difficult to place a theoretical limit on thermal signals, so I did a simple experiment to test the response of the gravimeter. A modulated heat source made of heating tape was hung in a ring about the upper half of the vacuum can. A crude parabolic aluminum reflector focused its power (80 watts) on the upper half the dropping chamber. The tape was turned on and off at the same frequency as the source mass modulation (in the 1997 experiment), thereby mimicking the actual thermal signal of the source mass on a single portion of the vacuum chamber[4] . The vacuum can was covered with a layer of nylon mesh and aluminum foil, just as it was in the G measurement. The temperature of the can was measured with a small thermistor taped under the nylon/aluminum shield.

The temperature signal recorded with the thermistor had less than a 0.25$^o$ C amplitude, as may be seen in Figure 5.9. The set-averaged temperature (the average temperature registered by the thermistor for a 20 minute set of 100 drops) varied from set-to-set by less than 0.03 $^o$C. The resulting differential signal in g was less than 0.7 $\mu$Gal.

A second test was done with the heating tape arranged about the lower

---

[4] The heat was on for twenty minutes, then off for twenty minutes, and so on.

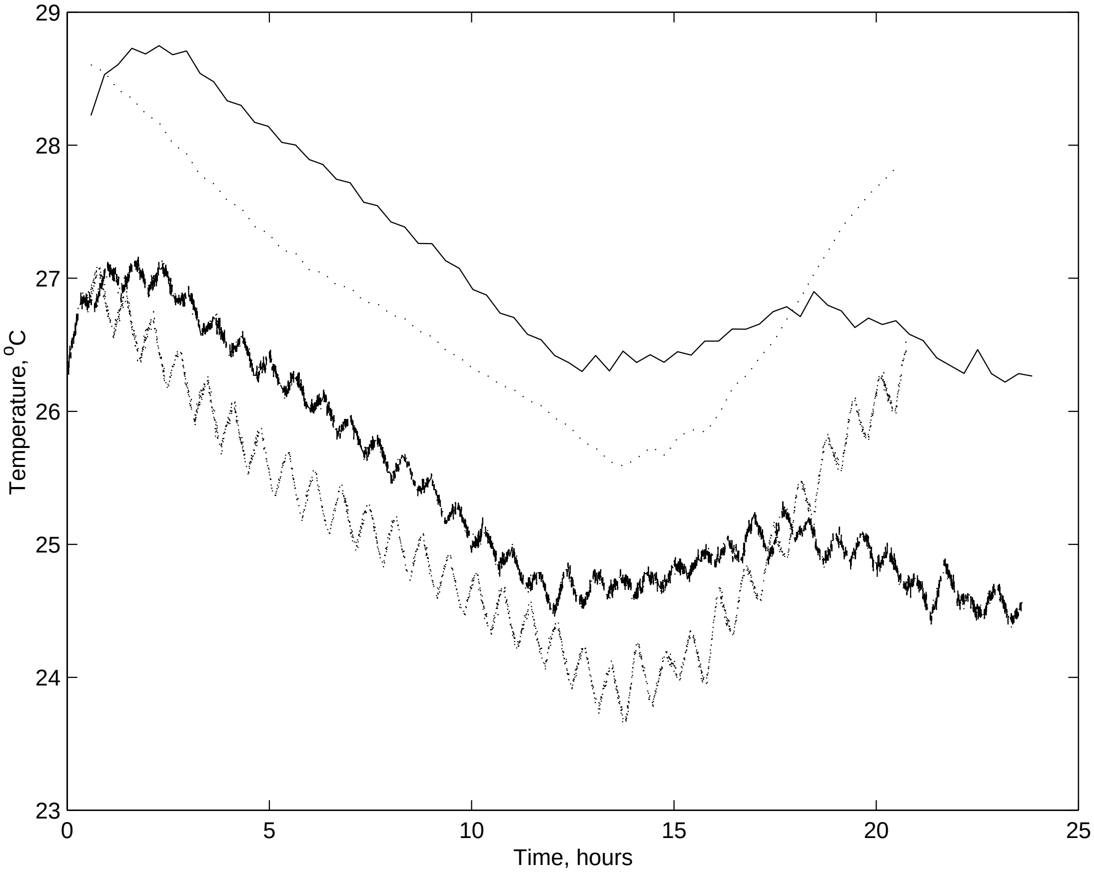

Figure 5.9: Temperature recorded by a thermistor taped to the dropping chamber during two test of thermal sensitivity. (···) - Upper portion of the can heated. The upper dotted curve is the curve of the average temperature for each 20 minute set, with an offset included for clarity. (—) - Lower portion of the can heated. Once again the upper solid line is the temperatures averaged over 100 drops, to provide the average temperature for each set.

portion of the vacuum can, to simulate the lower source mass position. In this run (the temperature signal is again seen in Figure 5.9) the temperature signal had less than a 0.2 $^o$C amplitude, with the set averages varying by less than 0.05$^o$C due to the modulation of the tape. The resulting differential signal in g was less than 0.15 $\mu$Gal.

We can calculate the worst case power incident on the dropping chamber of the gravimeter due to black body radiation emitted by the source mass. The

Stefan-Boltzmann law gives

$$P = \sigma e A(T_s^4 - T_c^4)$$

where $P$ is the power, $\sigma$ is the Stefan-Boltzmann constant (5.6e-8 W $\mathrm{m}^{-2}$ $\mathrm{K}^{-4}$), $e$ is the emissivity (the worst case value is 1), and $A$ is the surface area between the source mass and the vacuum chamber (about 0.12 $\mathrm{m}^2$). $T$ is the temperature. I assume a (generous) $0.5^o$ C temperature difference between the source mass and the vacuum can in either of its two positions. This is based on a measured $1.5^o$C temperature gradient from the floor to the ceiling of the building, coupled with the assumption that the source mass will carry an average temperature between its upper and lower positions. These values lead to a value of 0.4 watts for the power radiatively transfered to the can.

Convective transfer of heat is also a concern. I assume a worst case scenario — that the body of air between the vacuum can and the source mass is held at one position, maximizing heat flow. Then the heat transfer to the can would be the flow from the source mass through the air to the can:

$$\frac{\Delta Q}{\Delta t} = \frac{KA(T_s - T_c)}{w}$$

where $K$ is the thermal conductivity of air (0.026 W/m-$^o$C), and $w$ is the width of the layer of air (about 0.2 cm). The $0.5^o$C temperature difference results in a flow of 0.01 W by convection/conduction.

Assuming a linear dependence of g on incident power, we can immediately see that the source mass thermal signal must be less than:

$$0.7\mu Gal\frac{(.4 + .01\mathrm{W})}{80\mathrm{W}} = 0.004\ \mu\mathrm{Gal}$$

in its upper position, and less than

$$\delta g_{\mathrm{Thermal}} = 0.15\mu\mathrm{Gal}\frac{(.4 + .01\mathrm{W})}{80\mathrm{W}} = 0.001\ \mu\mathrm{Gal}$$

in its lower position. Thus the total thermal effect of the source mass is less than 0.005 $\mu$Gal or 60 ppm.

It was possible that there was a correlation between the $\delta g_o$ values and a diurnal thermal signal. We didn't expect any such dependence, but to check it the difference values were averaged in time. Every difference that was measured between 2 and 3 pm (Rocky Mountain Time) was averaged together to give a time-binned picture of the differences at around 2:30. This picture is in Figure 5.10. The larger error bars around 8 and 9 in the morning are due to the small amount of data at those times. Traditionally I would reset the gravimeter every morning at about 8:30.

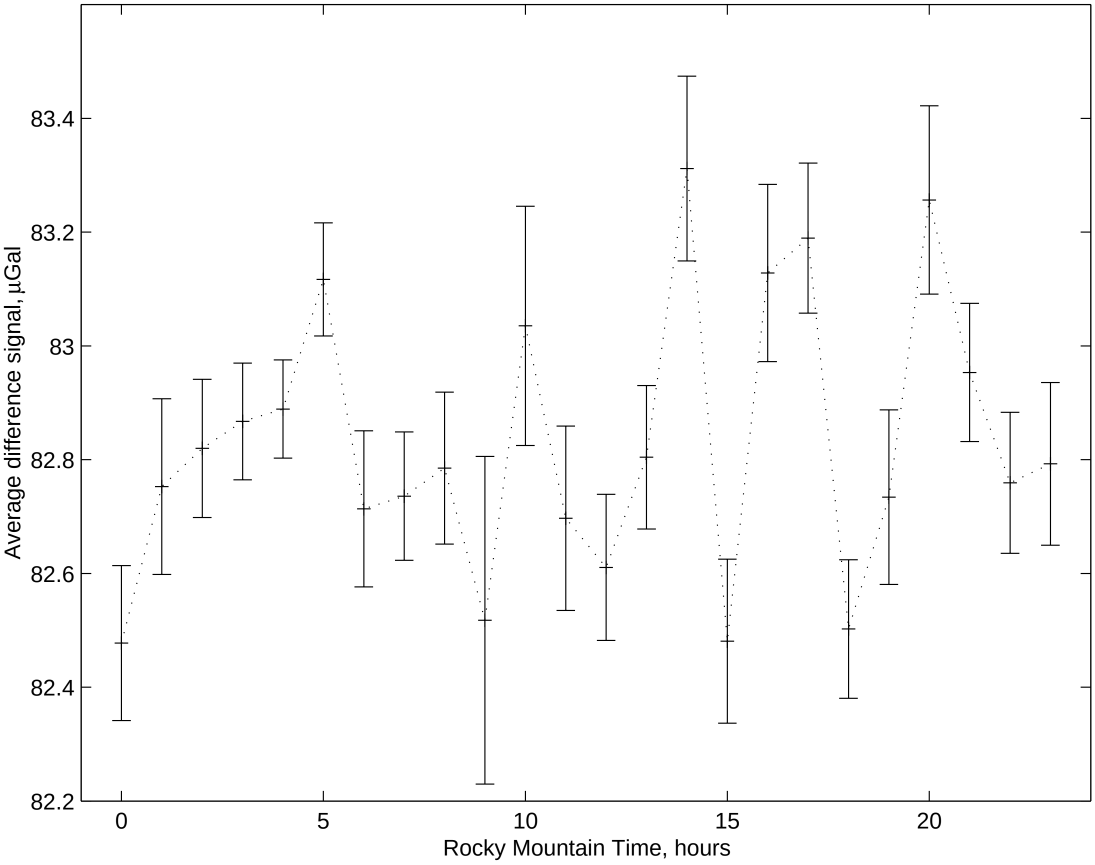

Figure 5.10: Time binned differences from the 1998 experiment. The times are for Rocky Mountain time zone. I reset the gravimeter at approximately 8:30 every day. This explains the larger error bars at those times.

### 5.2.3 Systematic Laser Excitation

High-precision lasers do not like to be bumped. When the laser of the FG-5 is tapped, it undergoes an oscillation in frequency at ≈ 100 Hz (the corner frequency of the piezo servo). The vibration of the drop and the associated sound impulse wave provide a tap that excites this response in the laser. This frequency modulation signal is triggered by the start of the drop and therefore systematically influences the fit for g.

The sound wave that strikes the laser was affected by the position of the source mass. Fig. 5.11 is a plot of 6300 averaged, corrected and differenced residuals — the difference in the average residuals with the mass up and the mass down. Difference residuals only show signals arising from systematic errors. These residuals clearly showed that one-tenth of the laser signal was either damped by the source mass in its lower position or amplified by it in its upper position. We fit for the "laser bauble" signal in the differenced residuals, and extracted information about the amplitude and phase of the oscillation. In a second data run the laser was located far away from the dropping chamber and its light was introduced to the interferometer through a fiber-optic (Sec. 3.1.3). In this system the power in the signal was observed to decrease by 50%.

Modeling this signal in a simulation of the system shows that the differential effect in our signal was 0.0015 $\mu$Gal . This corresponds to 20 ppm, about 1/30 of our statistical uncertainty.

### 5.2.4 Laser Verticality and Floor Tilts

For the interferometer fringes to represent vertical position measurements the laser beam must be parallel to the local vertical. If this condition is not satisfied and the beam deviates from vertical by a small angle $\theta$, a cosine scaling

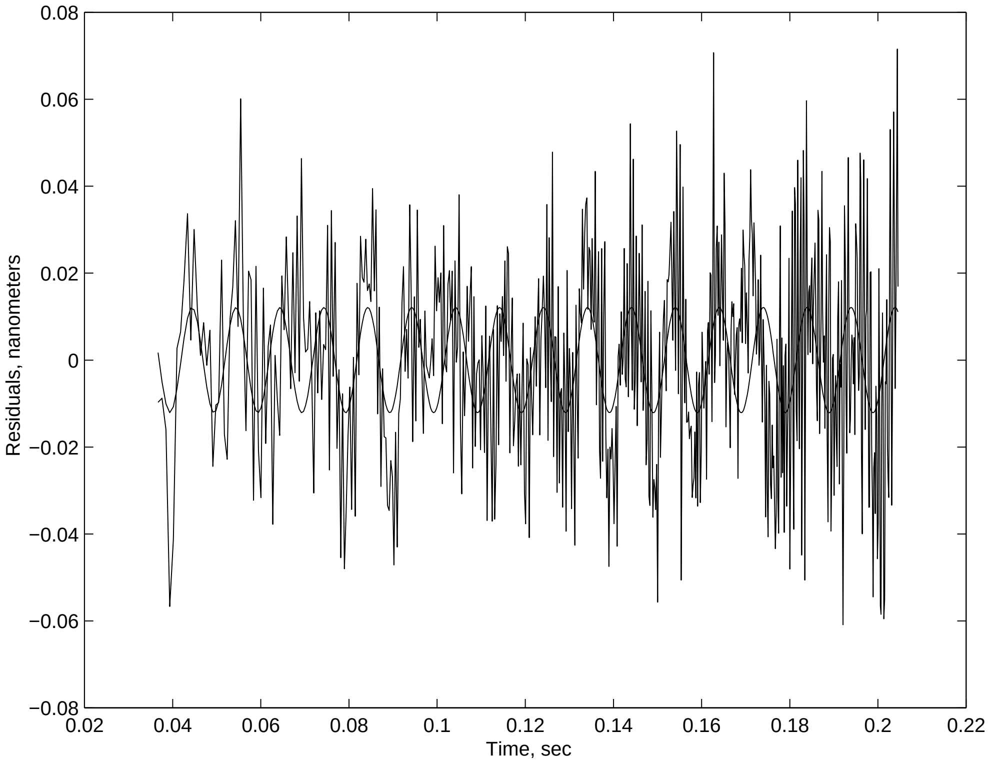

Figure 5.11: Corrected and differenced residuals from 64 sets of the 1997 data. Residuals from drops with the source mass in its lower position were averaged and then subtracted from the averaged residuals of the drops from the upper position. This "differenced residual" was then corrected by removing a theoretical curve representing the difference in residuals due to the source mass perturbation. The sine fit has a frequency of 100.3 Hz and an amplitude of 12 picometers.

error of magnitude

$$\frac{\delta g}{g} = \frac{\theta^2}{2} \tag{5.2}$$

occurs.

Verticality shifts are caused by tilts of the components of the interferometer, of the laser, or of the interferometer supports. These tilts can be introduced by ground tilt or thermal expansion signals. Although no differential signal is introduced by a steady common mode error the verticality may change synchronously with the G measurement due to random correlation of environmental thermal effects. If the verticality could, in fact, respond to temperature signals at the high frequency of the source mass modulation, it would influence the scatter of our results. It is possible that there is significant power in the temperature signal at this high frequency but because the environment was not phase locked with our experiment only the day to day scatter of our results would have been influenced.

The verticality of the gravimeter system can not be measured while the gravimeter is running[5] . This means that we could not directly measure changes verticality at scales that were important to our results, nor could we effectively monitor the verticality throughout our data runs. Therefore it was not possible to do more than conjecture about the random effects of verticality on scatter.

The likelihood that the thermal signal of the source mass affected verticality is small. The interferometer optics were shielded from the source mass by a 1/4" thick aluminum box and the thick aluminum party tray of the gravimeter. The interferometer was approximately 60 cm below the lower source mass position.

The verticality could have been systematically modulated by floor tilts coupled with the free fall measurement. The source mass was moved between its two optimal positions with as little horizontal movement as possible, minimizing systematic floor tilts. The weight of the source mass was sufficient to constrain the support screws to hang within 0.6 mRad of vertical. This was measured by examining the separation of both the screws to a long rod suspended from a thin wire, and the source mass to the dropping chamber[6] . An angle of 0.6 mRad in the screws corresponded to a horizontal source mass motion of 0.02 cm between its two positions.

To bound the magnitude of systematic floor tilt I measured the tilt of the pier[7] as I shifted weights on the floor. I used a prototype opto-electric bubble

---

[5] The verticality can only be measured to a precision of 0.2 $\mu$Gal (about 0.02 mRad) [40]

[6] Differential thermal expansion of the lifter legs is a negligible influence on the vertical motion of the source mass

[7] The interferometer was supported on a 5 foot pier of concrete embedded into the floor.

level ([41]) to measure the pier tilt, which was measured in two directions to avoid undo sensitivity to reinforcing bars in the concrete floor. The tilt was checked at a period matching the possible floor loading signal from the G-experiment.

To connect the tilt of the screws to a floor loading, I assumed that the tilt of the floor was linearly proportional to the horizontal displacement of the center of mass of the source mass. Thus the measurements of floor tilts from different weights placed at different distances from the pier showed that the pier tilted 0.5 $\mu$radians for a 1 cm horizontal movement of the source mass. This gives an estimate of 10 nanoradians systematic floor tilting synchronously linked to the G-measurement.

The experimental error due to a tilt of $d\theta$ depends on the mean value of the verticality of the laser, $\theta$ — the differential error we are concerned with results from the change in the absolute error of the verticality:

$$\frac{\delta(\delta g)}{g} = \theta d\theta \tag{5.3}$$

Assigning a base angular verticality error corresponding to 1 $\mu$Gal , the worst case error arising from systematic floor tilt is only 15 ppm. This is negligible.

### 5.2.5 Ball Wear

The tungsten balls that support the proof mass on the co-falling chamber wear with time. This introduced two possible difficulties for the G measurement. Firstly, the wear changed the relative position of the start-of-drop and the source mass. Secondly, as the tungsten wore the mass distribution in the proof mass changed, weakening the connection between our model and the actual test mass. Both mechanisms introduced little error in the G measurement. Their combined contribution was 12 ppm.

### 5.2.6 Phase Coherent Excitation of the Super Spring

It is possible to view the super spring as a very long ($\approx$ 1 km) simple spring; the temperature response of the equilibrium position of the spring/mass system follows this model. We were concerned that such a 'soft' spring would respond to the shift in gravitational potential resulting from the translation of the source mass. When the source mass was moved to its lower position closer to the spring, the proof mass would 'suddenly' be subject to an increase in the upward gravitational attraction of the source mass. This would cause the equilibrium position to rise. When the source mass moved to the other location, the opposite would occur, and the super spring would 'fall' back to its old equilibrium. A calculation incorporating the source mass field and information about the spring's fundamental frequency shows that the acceleration amplitude resulting from these excitations would be about $1\mu$Gal.

The acceleration signal of the excited super spring is a damped sine wave. The super spring would oscillate for approximately three periods before the amplitude of the harmonic motion would become small enough to loose phase coherency [42]. Although the drop to drop scatter of the FG-5 was too large for this underlying error signal to be seen in a single data set, the differential signal would have been preserved over the whole experiment. Because the integral of a damped sine wave over 3 oscillations is non-zero, this super spring excitation would bias the $\delta g_{\rm o}$ measurement.

To decrease this coupling the source mass was moved slowly compared to the period of the super spring. This allowed the equilibrium position of the spring to change slowly while keeping the amplitude of oscillation as small as possible. Approximately 30-40 seconds of time were allowed after each move for the super spring to damp down from whatever excitations it may have experienced.

As a quick test for this coupling we examined drop data from the beginning of each set of data to its end, looking for a damped sinusoid. Figure 5.12 shows the results for data runs in 1997 and 1998. This analysis, although too noisy to place a bound on the super spring excitation, is interesting because it would reflect any trends in the data. Also, within smaller averaging groups (only 20 sets instead of all the data of the experiment) some low frequency trends were observed. These, discussed in more depth in Sec. 5.2.10, could be the result of a higher frequency mode of the super spring beating with the drop measurements.

To bound this error compare the theoretical amplitude of a spring excited instantaneously and one excited (roughly) adiabatically, following the discussion in Faller[22]. The ratio of the Fourier components at the resonant frequency of the spring when released in these two ways will be equal to the amplitude of motion at that frequency, so:

$$\frac{A_{\text{Sudden}}}{A_{\text{Slow}}} = \frac{\int\limits_{-\infty}^{0} e^{-i\omega_o t} dt}{\int\limits_{-\infty}^{0} e^{-i\omega_o t} dt + \int\limits_{0}^{\infty} e^{-kt} e^{-i\omega_o t} dt}$$

where $\omega_o$ is the fundamental frequency of the super spring (about 0.1 rad/sec), and $k$ is the decay rate for the equilibrium position (approximately 0.03 rad/sec). Plugging in the numbers we find that the amplitude of the slowly-release spring would be approximately one twentieth of amplitude of the suddenly released spring. Thus an approximation of the signal amplitude would be $1\mu\text{Gal}/20 = 0.05\mu\text{Gal}$. A worst case scenario would be that a single drop would consistently be skewed by this whole amount in each set. This would introduce a bias of $0.05/100 = 0.0005\mu\text{Gal}$ in each set (100 drops per set), and a difference bias of 10 ppm.

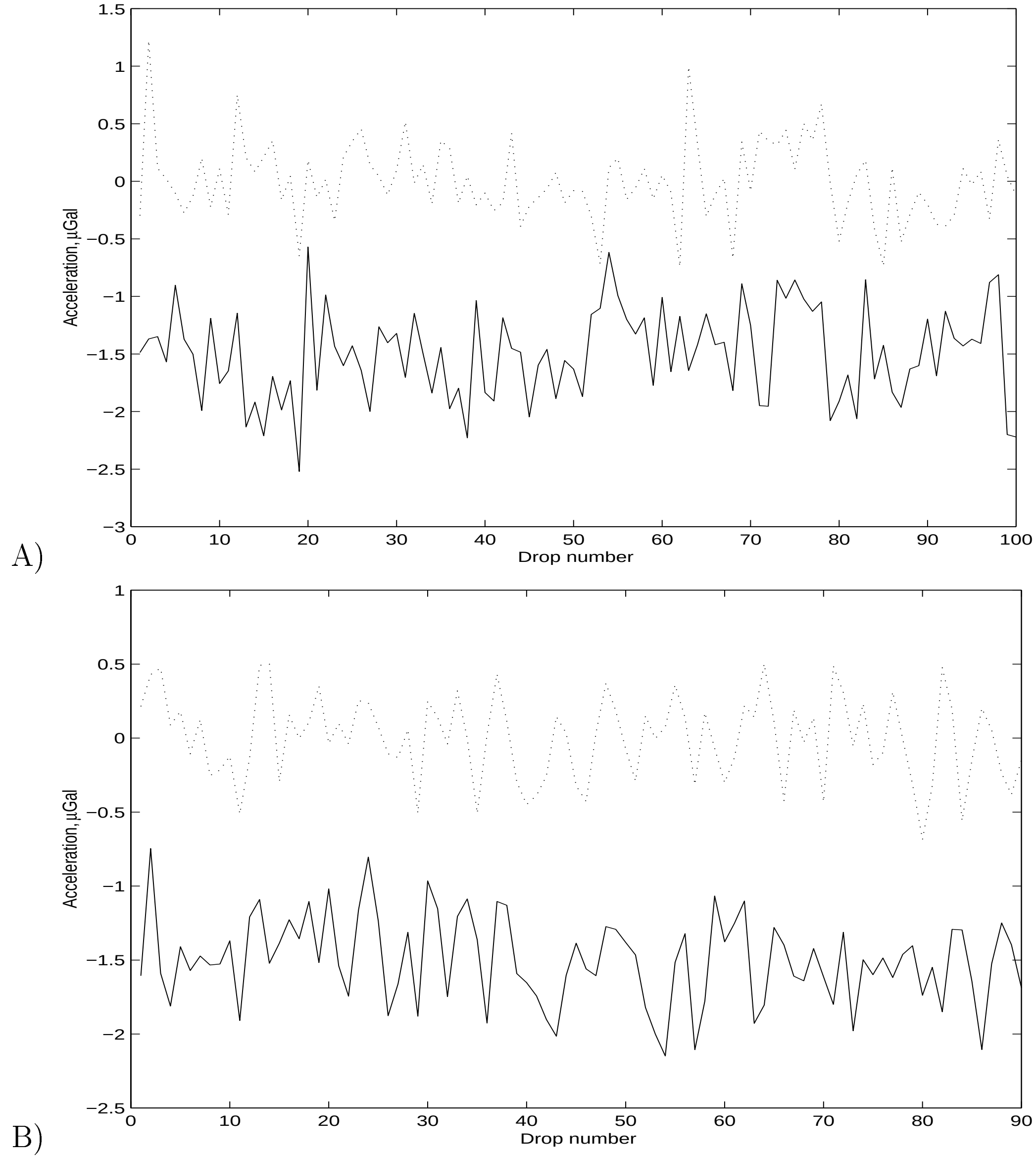

Figure 5.12: Plots of drop-wise-averaged sets. (···) Source mass in its upper position, with mean value removed. (—) — source mass in its lower position with mean value and 1.5 $\mu$Gal removed. A) Sets averaged for the 1997 data run. B) Sets averaged for the 1998 data run.

### 5.2.7 Magnetic Effects - Static Fields

An external magnetic field will induce magnetization within any object with non-zero magnetic susceptibility, resulting in a force on the object. This force is the "direct attraction" of the object to the external field. The magnetization will also result in a perturbation to the original field that depends on the susceptibility, geometry, and position of the object.

In the free fall measurement a static magnetic field, $B_{ext}$, was generated by the Earth and the permanent magnets of the ion pump and drive motor. The source mass had a susceptibility of $\chi = 0.00066$ in MKS units. Thus the source mass underwent some magnetization — it looked like a magnet that produced a field of approximate magnitude $\chi B_{ext}$. This static magnetic field could differentially influence the acceleration of the proof mass.

If a conducting object, such as the proof mass, is in motion through a spatially variant magnetic field an eddy current damping effect will occur. Eddy current damping is a frictional loss resulting from the dissipation of energy by the action of an electric current induced in a current loop by a time varying magnetic flux. From Faraday's law we see that an electro-motive force (emf), $\varepsilon$ is generated:

$$\varepsilon = \frac{d\Phi}{dt} = A\frac{d|\mathbf{B}|}{dt} \tag{5.4}$$

for a loop of area $A$ within a time changing magnetic field, $\mathbf{B}$, if the magnetic flux, $\Phi$, penetrating the loop is $A\mathbf{B}$. Thus a loop moving through temporally static yet spatially dynamic field with velocity $v$ will experience an emf related to the rate of change of the field. If that the loop is moving in the $\hat{z}$ direction:

$$\begin{aligned} \frac{d\mathbf{B}}{dt} &= \frac{dB}{dz}\frac{dz}{dt} \\ &= v\frac{dB}{dz}, \quad \text{so :} \\ \varepsilon &= vA\frac{dB}{dz} \end{aligned}$$

For a loop of metal with resistance $R$ the emf will result in a current I, and a power dissipation, P, of:

$$\begin{aligned} I &= \frac{\varepsilon}{R} = \frac{vA\frac{dB}{dz}}{R} \\ P &= \frac{\varepsilon^2}{R} = \frac{v^2A^2(\frac{dB}{dz})^2}{R}. \end{aligned}$$

The power dissipated by the current is equal to the force acting on the object times its velocity, so the eddy current force must be proportional to the velocity and the gradient squared:

$$F = \frac{P}{v} = \frac{vA^2(\frac{dB}{dz})^2}{R}$$

The actual magnitude of the fields associated with the source mass, and their spatial dependence, were directly measured without the gravimeter present. These measurements and the detailed calculation of the differential eddy current effect are presented in Sec. B.2.1. Differential eddy current damping arising from all static fields associated with the source mass introduce error into the G measurement only at the levels below pGal.

### 5.2.8 Magnetic Effects – Dynamic Fields

Time varying magnetic fields also exert forces on conducting loops. Although the magnetic susceptibility of the source mass is very moderate, as discussed in the previous section, its conductive characteristics cause it to shield the proof mass from most AC magnetic fields — there is no ameliorating factor of 0.0006 (the susceptibility) to reduce the signal. The entire force contribution of any AC magnetic field modulated by the source mass would be represented as a differential error. After considerable work (described here) we found that errors arising from AC fields were thousands of times smaller than our uncertainties.

The source mass only shields the test mass from fields propagating from the direction of the source mass towards the test mass. Magnetic fields were produced by AC currents flowing in anything from a fan to the power conduits around the experiment. The most important source of an AC magnetic field was the servo motor used to drive the co-falling chamber. This motor was located below, yet close to, the region of free fall. Its field would be largely shielded only when the source mass was in its lower position.

Alternating magnetic fields acted on the test mass in three ways. They caused a sinusoidal force that sprang from the sinusoidal variation in the flux intersecting the cross section of the proof mass, a repulsive force that was dependent on the inductance of the proof mass, and a damping component that arose from the eddy current damping associated with the necessary spatial dependence of the A.C field. The last was discussed in the previous section.

The sinusoidal and constant forces can be calculated in the following way, following [43, 44, 45]. A time variant magnetic field, $B \sin(wt)$, impinges on a current loop with cross sectional area $A$, resistance $R$, and impedance $L$. Using Lenz's, Faraday's and Kirchoff's laws we see that the current, $I$ in the circuit satisfies:

$$Bw \cos wt = IR + L\frac{dI}{dt}$$

A solution to this differential equation is:

$$I = \frac{BAw}{R^2 + w^2L^2}(R \cos wt + wL \sin wt) \tag{5.5}$$

the vertical force $F_v$ on the loop is then

$$\begin{aligned} F_v &= (IXB)_v \\ &= IB_r \end{aligned}$$

where $B_r$ is the radial field. Assuming that the AC B-field is generated by an oscillating magnetic dipole, it is reasonable to use (for a small current loop) this expression:

$$B_r = \frac{B_o \sin \omega t}{h^3} \tag{5.6}$$

where $h$ is the height of the loop above the source of the magnetic field. Combining Equations 5.6 and 5.5, we get an expression for the force on a current loop falling through the magnetic field produced by an oscillating dipole:

$$\begin{aligned} F &= \frac{B_o \sin \omega t}{h^3} \frac{B_0 A \omega}{R^2 + \omega^2 L^2} (R \cos \omega t + \omega L \sin \omega t) \\ &= \frac{B_o^2 A \omega^2 L \sin^2 \omega t}{h^3 (R^2 + \omega^2 L^2)} + \frac{B_o^2 A \omega R \cos(\omega t) \sin(\omega t)}{h^3 (R^2 + \omega^2 L^2)} \end{aligned} \tag{5.7}$$

The second term of this equation represents an oscillating signal, while the time-average of the first term is:

$$F_{\mathrm{r}} = \frac{1}{2} \frac{B_o^2 A \omega^2 L}{h^3 (R^2 + \omega^2 L^2)}.$$

Thus $F_{\mathrm{r}}$ is a repulsive force acting to push the loop away from the oscillating dipole that generates the field. This derivation is only accurate for a small range of motions. If life were simple we could express the field produced by the motor as an expansion of oscillating dipoles and then calculate, in theory, the resultant force on the test mass. Unfortunately our system was so complicated that it was nigh well impossible to perform the calculation.

To calculate the force it is necessary to know the time varying amplitude of the radial and vertical magnetic fields at the position of the test mass. To do this we must first create a model for the field produced by the drive motor. Direct measurement showed that the motor creates a field containing two frequencies. The lower frequency is the same frequency as the rotation of the spindle. The other is 13 times higher. These fields are caused by permanent magnetizations within the motor (which has 13-fold symmetry). Thus the motor is easily modeled as a series of oscillating dipoles. The amplitude of the fields depend only on the speed of the motor.

This information only lets us model the fields outside of the vacuum can. Inside the can, and inside the co-falling chamber where the test mass is truly located, the situation is more complex. The skin depth, or thickness at which a conductor will damp out approximately 65% of the amplitude of the field is:

$$\delta = \sqrt{\frac{2}{\mu\sigma\omega}}$$

where $\mu$ and $\sigma$ are the permittivity and conductivity of the shielding material. The attenuation of the field depends on both the thickness of the shield and the frequency of the signal. Because the motor signal is chirped the frequency and amplitude of the original signal changes. The vacuum can is cylindrical so the amount of shielding varies across its length. Because the proof mass falls, the angle at which the signal intercepts the vacuum can changes, changing the thickness of the shield even as the field amplitude increases. Of course the relative proportion of the vertical and radial components of the field that make it through the shield change as well.

We could (and did) directly measure the field at each point in the can, for each position/velocity of the proof mass (if we ignored the effect of the co-falling chamber). This doesn't help with a theoretical solution because of the complexity of the proof mass, which is a far cry from a ring with a well defined area, impedance, or inductance. It contains aluminum, beryllium copper, tungsten and glass. Portions of it are threaded. Portions are bored, bent, burnished, slitted, slotted, slanted. So much for theory.

Presented with such a difficult theoretical situation it was necessary to experimentally determine the magnitude of the acceleration signal of the AC magnetic fields. Figure 5.13 is a picture and schematic of the apparatus used to do this.

The apparatus consisted of a high precision balance[8] that supported a Plexiglas beam. The beam was coated with a fine carbon power to reduced electro-static effects. It was enclosed within a conductive shell, shielding it from air currents

---

[8] This balance was previously used in an experiment to check whether gravity diminishes above a spinning disk, [46].

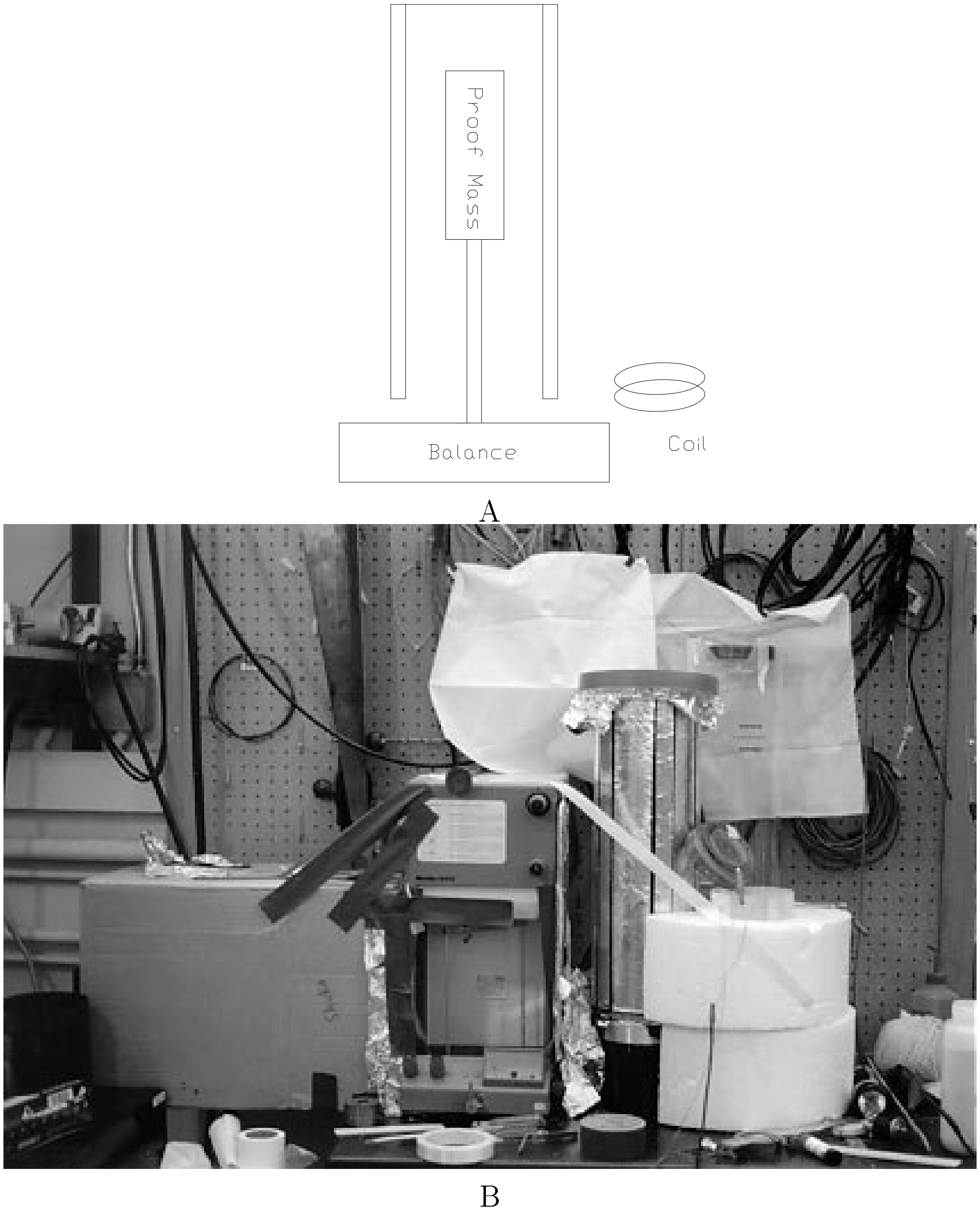

Figure 5.13: The apparatus used to measure the force of AC magnetic fields acting on the test mass. A) A schematic of the system. B) A photo of the apparatus. A balance (center) with precision 0.0001 gram, or 1 part in $10^6$ of the mass of the test mass. The balance supported a beam that extended past its sides, into the vacuum can (upside down, on the right) and a cardboard box lined with aluminum foil (on the left). In the box the beam supported a non-conducting counter weight. In the vacuum can the beam supported an actual test mass from an FG-5 system (also upside down). Two coils (positioned around the vacuum can) provided AC magnetic fields at a variety of frequencies. The change in the balance reading represents the magnetic force on the proof mass. The balance, alone, was not sensitive to the fields.

and electric fields. On one side of the beam was an actual FG-5 proof mass, on the other side was a non-conducting counterweight. The proof mass was placed on a pedestal on the beam so that it was positioned within the same vacuum can (open to air) used in the G experiment.

Magnetic fields were produced by voice coils positioned around the vacuum can and measured without the test mass in position. The fields were measured at three positions inside the vacuum can at frequencies of 5, 10, 20, 40, 80, 160, 300 and 600 Hz. The low frequency component of the drive motor field chirps from 0 to 40 Hz during a drop. The field amplitude generated by the coils was as large as could be produced with the amplifier we used. The balance showed no response to these fields.

After this "field calibration" the proof mass was placed on the beam at the same three positions. The resulting forces, measured by the balance, were used to place limits on the drive motor's effect on the test mass during the G measurement. The largest force generated by this system was approximately 1.5 mg. At very low frequency (where the force is small) and at frequencies higher than 300 Hz (where our amplifier had trouble driving the voice coils) the balance gave null results. Ground stainless rods were placed in the vacuum chamber to simulate the effect of the guide rods in the dropping system. The entire signal of the servo motor was 4 orders of magnitude smaller than the precision reached with the G experiment.

### 5.2.9 Contaminated Fringes

Generally neither the points at the very beginning nor those at the very end of the drop are used in the fit for local acceleration. Data at the beginning is very noisy due to airgap noise (Section 5.2.1) and missed fringes. When real fringes were missed by the discriminator[9] , the fringes recorded by the gravimeter are incorrectly scaled. Missed fringes are very easily identified — either by the acceleration value they produce, or by the chi-squared of the fit. Figure 5.14 shows the acceleration parameter from fits to drop data, some of which was contaminated. Only about 10% of the data has a missed fringe beyond fringe 15. That data was always removed for the final analysis. At the other end of the drop the data could be contaminated by the servoing of the co-falling chamber to catch the test mass.

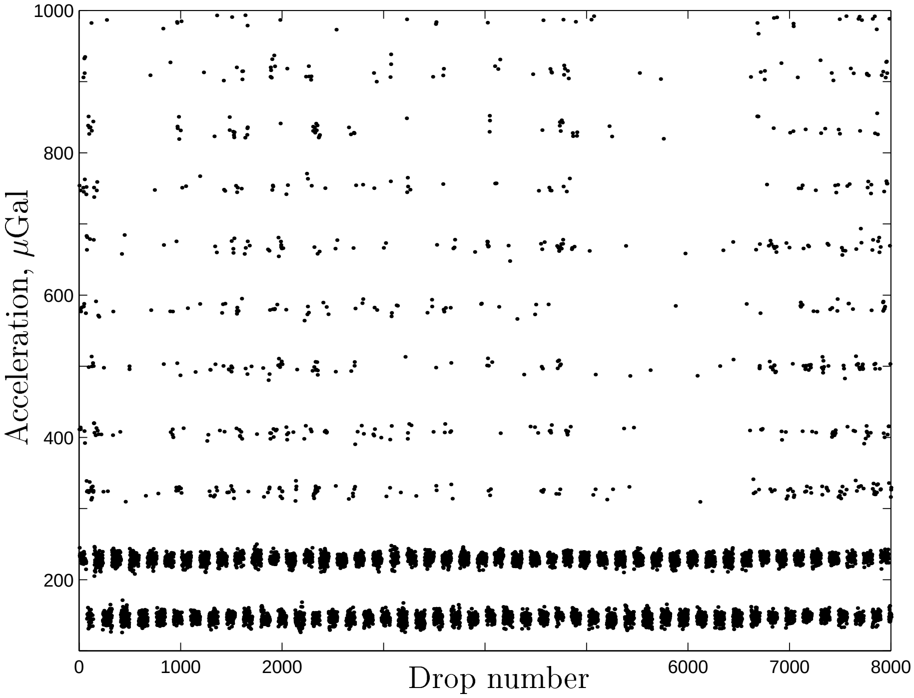

Figure 5.14: Plot of data with missed fringes. Banding due to the quantized nature of missed fringes is easily seen. A single missed fringe results in a bias of approximately 170 $\mu$Gal. The bias varies by $\approx$5 $\mu$Gal depending on which fringe was missed. The occasional lack of contamination (e.g. at drop 6000) occurs when the amplitude of the interferometer output increases. Note that if the fits for g were started just a few fringes later in the drop no mis-scaled fringes would be included and no banding would occur.

---

[9] Fringes were only missed before fringe #18. By processing data with an FFF beyond that, the problem could be completely avoided. Of course that would mean giving up some information…

The measurement of the absolute acceleration is much more sensitive to errors arising from the inclusion of contaminated data than was the free fall G measurement. In the differential mode there is much greater freedom to choose the data to fit. A typical "start fringe" is (scaled) fringe #20, while a typical "end fringe" is #640.

At some choice of start and stop fringes all the data too poor to use (even in the differential mode) lay beyond the boundary fringes. It is not necessarily clear, however, that the entire region of reasonable data should have been fit. The quality of the data can vary from the beginning of the drop to the end. As earlier and earlier fringes are fit, more and more drops become contaminated by missed fringes. Although the statistical uncertainty in the fit is inversely proportional to the square root of the number of data points used in the analysis, more points do not necessarily better results make.

One way to identify the fringes bounding good data was to evaluate the dependence of the local acceleration on the set of data fit — a good start or stop fringe lies in a region where the value of g is independent of the choice of fringe. This is a technique commonly used in absolute gravity measurements. Figure 5.15 contains a plot such as might used in this method. A similar system involves examining the residuals to the fit and directly identifying the point at which the catch, for example, begins.

Because it is not the absolute value of the g value that interested us we used a very simple method to decide which data to use. The choice of start fringe that caused the uncertainty in the value of G (as opposed to g) to increase sharply defined the edge of "forbidden territory." The boundary fringes were #10 – #150 for the start fringe and #580 – #670 for the end fringe.

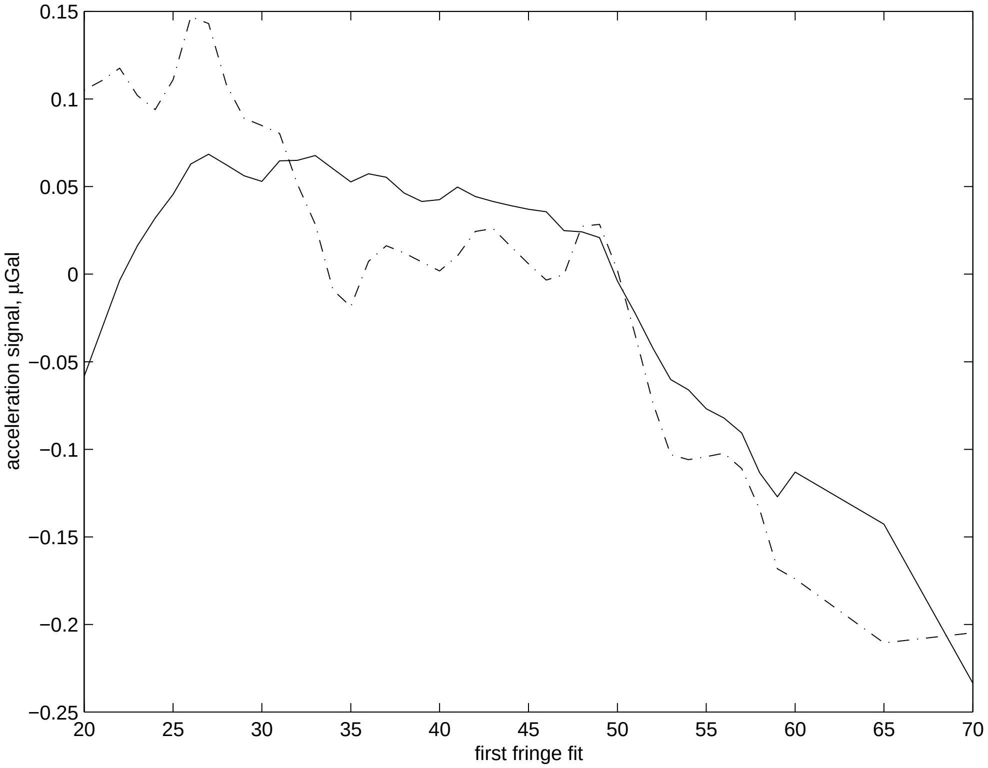

Figure 5.15: Dependence of g and $\delta g_o$ on the first fringe fit. (–·–) The absolute acceleration, g (source mass in its upper position), as a function of the first fringe fit (an offset value has been removed). (—) The acceleration difference signal from the free-fall experiment as a function of first fringe fit (with offset removed). In both curves the last fringe fit was N$^{o.}$ 640. Note that the curvature of the solid line and some drift of the dot-dashed line, is a signal generated by the source mass – and is expected.

### 5.2.10 Unquantified Error Sources

We have thought of several poorly defined mechanisms that could have influenced our results but that we couldn't (and/or didn't) test. When the results of the 1998 run displayed high set-to-set scatter (but not drop-to-drop scatter), we tried to think of sources of systematic error that could change our measured value for G on the time scale of a day. In this section a few of the possible mechanisms we thought of are presented.

One of the first mechanisms that came to our minds was a grounding problem between the experimental apparatus of the free-fall experiment and the FG-5. Errors in the measurement of g as large as 10$\mu$Gal have been attributed by Micro-g Solutions Inc. to unspecified grounding errors, generally involving the super spring system. The mechanism that would result in a mismeasurement of the absolute acceleration is not clear.

There certainly were opportunities for ground loops to occur in our last measurement. The drop initialization trigger was used in the airgap measuring apparatus, in the FG-5 system, and in the shaft encoder output recording system. The shaft encoder voltage was actually read by the FG-5 in place of the super spring position. Additionally, the aluminum layer surrounding the dropping chamber was held at 1.5 volts over a ground referenced to the chassis of a power supply itself ground to the wall.

During the experiment, worried about such ground loops, I disconnected the shaft encoder recording system for a quarter day, but didn't see any change in drop-to-drop scatter. Since it was our set-to-set scatter that was surprising, this really doesn't tell us much. Unfortunately the question of how ground loops might affect the scatter is left unanswered. It is very difficult to imagine a non-pathological mechanism that would link any grounding problems to the source mass position.

A second mechanism that could influence low-frequency drifts in our experiment was a random coupling of a higher order mode of the super spring to the measurement. The super spring has a mode in which the spring that supports the reference mirror twists. This mode has a frequency of approximately 0.3 Hz. An amplitude of 7 $\mu$Gal would correspond to drop-to-drop scatter of 5 $\mu$Gal. The decay constant of this mode is approximately 9 minutes. The twist mode is responsible for the majority of the g signal injected to the system by energy in the super spring [47].

It is possible that the movements of the source mass maintained energy in the twist mode without strongly changing its phase. Because a small vertical torque is sensed by the floor when the source mass was moved, the excitation would by systematic. Also, this would explain why the scatter in our G-values increased in the data run of 1998, where there source mass was moved more frequently.

This mechanism is not very likely, however, because the amplitude of the effect would be very small. The period of the torsion mode was observed to be $3.93 \pm 0.1$ sec. At this frequency the worst case bias to the difference signal would be 0.17 $\mu$Gal. The signal we saw in the data had a much larger amplitude than this. The fact that no increased scatter was observed in the beginning of each set as opposed to the end of the set (Section 5.3) seems to indicate that this wasn't an important effect. Finally, the gravimeter has been run continuously throughout the movement of the source mass. As soon as the source mass motion ended, the scatter immediately returned to its value before the move.

Let us, nevertheless consider a pathological case in which the beat frequency between the measurement rate (1/5 Hz) and the spring (the pendulum mode of the spring was close to 1 Hz) were very low (less than 0.02 Hz). Then the bias introduced by the spring would not be averaged out over many cycles in each set. In the case that the beat was 0.015 Hz, the bias could easily be 0.4 $\mu$Gal , in one set. Assuming the phase and amplitude were maintained, the next set would be biased by -0.4$\mu$Gal .

Thus, in the special case that the frequency of measurement was very close to a multiple of the spring frequency, the underlying signal could very well have been caused by phase drifts in the spring. It would not require a phase modulation on the time scale of the sets, but only on the scale of the drifts. The fact that the coherence did not clearly extend between different days of data[10] provides some

---

[10] Each morning I suspended the measurements and down loaded the previous day's data

support for this mechanism. Because the coherence was not completely continuous within a day, however, this is not a strong statement.

Examination of the Figure 5.16 shows that a low (mHz) signal can be seen in some averaged sets. The sets were averaged in a region where the coherent signal in the difference data was clearly evident. This is consistent with the idea that the spring mode was randomly phase locked with the experiment.

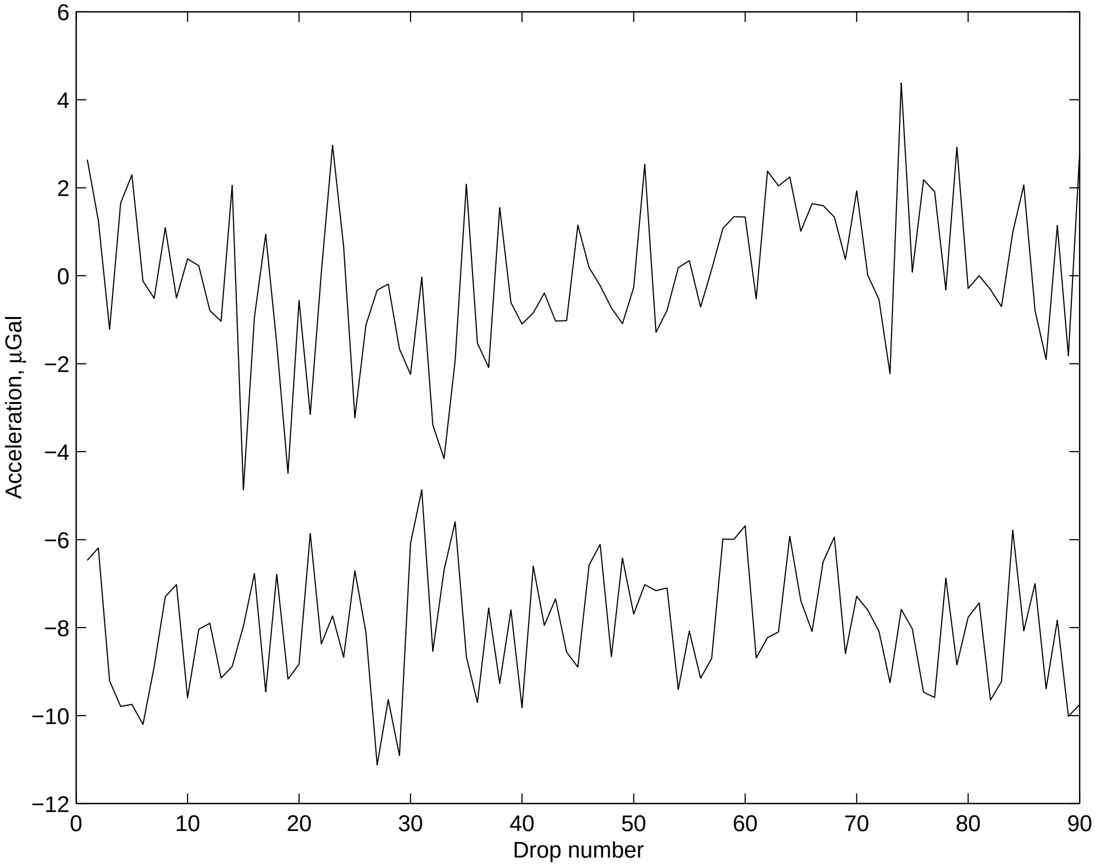

Figure 5.16: Plot of acceleration value by drop averaged over 26 sets (13 with the source mass down). Notice that there is an underlying signal in the data that suggest the presence of systematic drifts linked to the start of each set. This underlying systematic is consistent with the a random phase locking of the super spring torsion mode and the measurement cycle of the gravimeter.

---

from the gravimeter computer. Sometimes I allowed the source mass to continue its motions, because this seemed to reduce wear in the support nuts. Generally it took about an hour to down load the data and reinitialize the gravimeter.

### 5.3 Evidence of other Systematic Errors

Systematic errors that do not perfectly mimic parabolic motion would leave telltale signatures in the record of the test mass motion. For this reason I hoped to unearth evidence of systematics by looking for anomalous signals in the drop data. I used a variety of methods, which are presented here.

Any dependence of G on the portion of the drop we analyzed is evidence of a systematic error. This is related to the work in Secs. 4.3 and 5.2.1, where the examination of the dependence of G on the first fit fringe (FFF) was used to extract information about the position of the start of drop and the airgap signal. Plots of the dependence of G on FFF for two data runs are shown in Figures 6.7 and 6.1.3. It is also possible to look for the dependence on the last fringe fit, as in Figure 5.17, but it was more reasonable to analyze dependence on start fringe than on end fringe because the start of the drop influenced the fit for acceleration much more strongly than the end. In fact the first half of the data accounts for 90% of the information about the acceleration. Also the source mass signal was much more clear at the beginning of the drop than at the end.

Other signs of corrupting signals may be found by analyzing the g values measured with the mass up, as opposed to the mass down. A different amount of drop-to-drop or set-to-set scatter could indicate a systematic effect. No significant differences were found. The drop-to-drop scatter was also compared between the beginnings and ends of sets of data, and was identical, suggesting that there was no appreciable excitation of the super spring during the movements of the source mass. In Section 5.2.6 sets of data representing the average set with the source mass either up or down were computed. The acceleration values of the $n^{th}$ drop of every mass-up set were averaged together to give the value of the $n^{th}$ drop of the average mass-up set. This was also done for the source mass in its lower

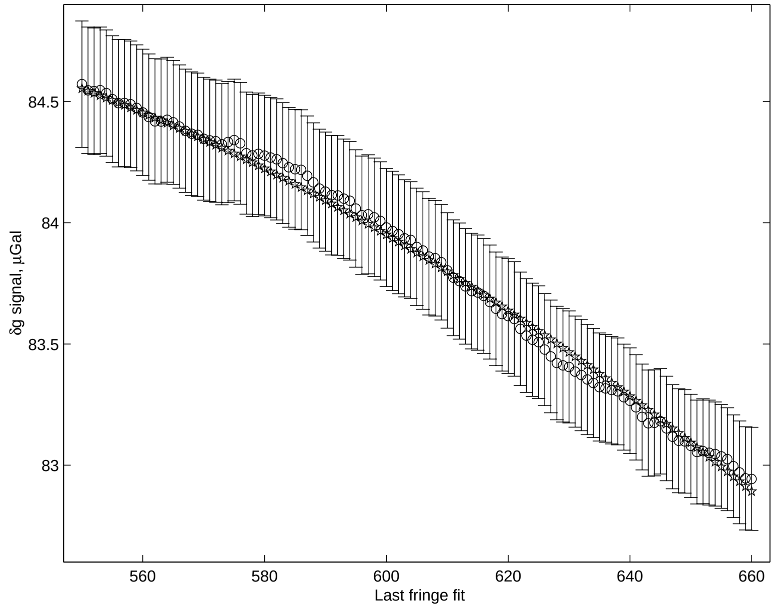

Figure 5.17: A comparison of delta g as a function of last fringe fit to theory. The first fringe fit was fringe 20. This data is extracted from a single day of data in the 1998 data run. The plot with error bars and circles is the experimental curve, while the smooth line of stars represents theory. Note the small sinusoidal signal in the data. I attribute this to the oscillating airgap signal.

position. The averaged sets are shown in Figure 5.12. These sets would reflect the presence of any systematic error parameter that would shift from one value to another over the time of a single set. Thermal signals coupled to the source mass position, for example, could slowly change the temperature of the ion pump, in turn changing its efficiency, the vacuum pressure, and the residual gas forces on the test mass. No evidence of these drifts is seen in the averaged results. Figure 5.16 shows the set-average for a short segment of suspicious data. Less than 20 sets were averaged for this plot which does display drifts.

Another test for systematics involves using the only half the data: Computing the differences using just the second half of each set and comparing them to the differences calculated using just the first half of each set would allow linear drifts (in g, as a function of the time from the start of the sets) to be identified. Processing all the 1998 data in this way resulted in two values for G (one value using the first half of set data, one value with the second half of set data). The two values were consistent. The difference between them was (0.007 ± 0.01) x $10^{-11}$ $m^3/kg\text{-}s^2$.

### 5.3.1 Residual Analysis

Valuable information remains in the residuals to each fit of drop data. Each fit produces values for the parameters of the parabolic function Eqn. 2.10. By subtracting the curve specified by these parameters from the data, a set of residual values is found, as in Fig. 5.18.

Information about various systematic errors may be extracted from these residuals. In the method of Klopping [39] the set of decaying sinusoids is assumed to describe many systematic errors in the measurement of g. Decaying sinusoidal signals might arise from vibrations excited by the drop, as in Secs. 5.2.3 and 5.2.1. A damped sine wave apparent in the test mass motion would clearly not result from any reasonable gravitational source.

Klopping developed a system that fit and removed decaying sinusoids from the data. The frequencies of the sinusoids were found by spectral analysis of the residuals to the drops, then the damping rate and amplitude were found with non-linear fitting techniques. His method is cited by Micro-g Solutions as an accepted provider of corrections for the airgap effect and is used to correct for different floor responses at absolute gravity sites.

We hoped to use Klopping's software to remove the airgap effect, and any other unknown signals. I wrote a program that read in the frequencies and decay constants[11] of the four largest decaying sinusoids for each set of data and then used

---

[11] The frequencies and decay constants were provided by a modified version of the TREX.EXE software that is standard to the FG-5 system. TREX.EXE is only configured for use with low data density data (180 data points per drop). The modification allowed permitted use with our high-density data (700 data points per drop)

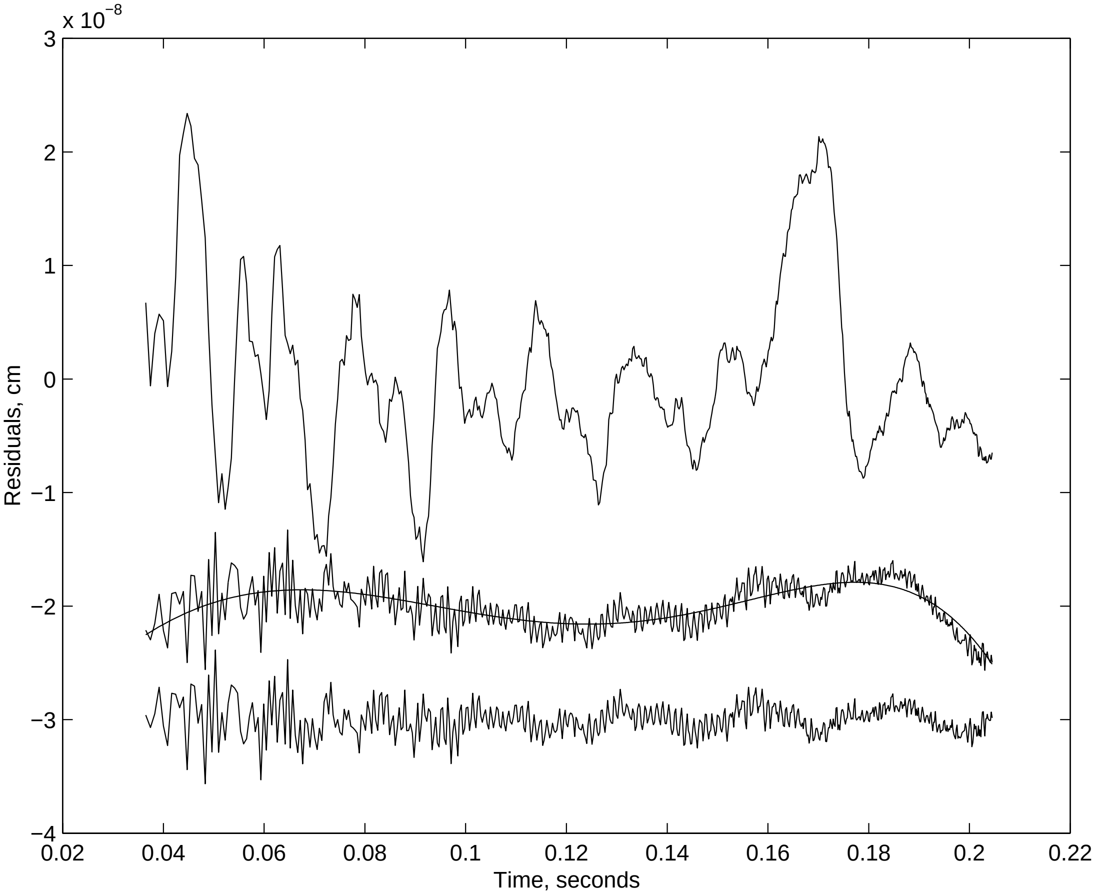

Figure 5.18: The residuals-to-drop averaged over 150,000 drops. The upper curve is the average residual, including data from both source mass positions. The choppy middle curve is the difference between the averaged residuals with the source mass in its upper and lower positions (with offset included). Note that the slight "M" shape of the differenced residuals is due to the higher order effects of the source mass (as in Fig.2.2). The theoretical expectation for the difference in residuals is shown with the smooth curve overlying the differenced residuals. The lowest curve is the differenced residuals with the model removed (and offset added). Any signal visible in the lowest curve represents the trace of a systematic error.

them to provide set corrections for the data. The set corrections would remove the airgap effect from all the data and the airgap problem would be solved.

This method of attack was unsuccessful. The set corrections did not reduce set-to-set scatter of g-values significantly, suggesting that the corrections calculated by this analysis were not valid. Also the uncertainty in $\delta g_o$ grew very large due to the inclusion of many fitting parameters (a damped cosine and sine function for each decaying sinusoid; a total of 8 extra parameters) in the least-squares fit. The lowest frequency of the sinusoids was 10 Hz — low enough to correlate strongly with the cubic and quartic components of the perturbing signal (as in Fig. 2.2, part B). This meant that the sinusoids would remove part of the source mass signal as well as any airgap errors.

# CHAPTER 6

# DATA AND RESULTS

## 6.1 Data Runs

We used the free fall method in three data runs, presented here in chronological order. The first was a proof-of-concept experiment that I call the "bronze mass run." The second acquired 9 days of data over a 13 day period in early May 1997. The third run incorporated several improvements to the apparatus and was conducted in late May of 1998.

### 6.1.1 The Bronze Mass Experiment

In the summer of 1995 David Newell and Paul Keyser, both graduates of JILA in physics, developed a system that allowed a bronze ring-shaped mass to be placed above and **far** above an FG-5 free fall gravimeter. In this way a differential measurement of the ring's gravity field could be made, but with only (at best) one half the optimal signal-to-noise. The system was built in JILA and was sufficient to show that the acceleration of gravity, as measured with a free fall gravimeter, could be perturbed with an external source mass.

I modified the apparatus in order to allow the source mass to be placed both above and below the region of the drop. The modified apparatus was portable, and was setup at the Table Mountain Gravity Observatory (TMGO), a much better (vibrationally quiet) site for gravity measurements than JILA. Figure 6.1

is a picture of the setup. This arrangement did not make provisions for high accuracy positioning of the source mass.

The source mass of this run was made of two bronze rings that had been used in two previous G experiments. The first experiment was that of Michael Hulett, who in 1969 measured the deflection of a horizontal pendulum due the gravitational attraction of the rings. His work was performed for his senior honors thesis with James Faller.

The bronze masses were reused in a G experiment that used a magnetic support system to escape the relatively stiff torsion constants of a fiber. This experiment was conducted by William Koldewyn in the mid 1970s, again with advisor Jim Faller [9]. Koldewyn had the masses precision machined and carefully measured their volumes. We used his density values in our theoretical models of the system. The two rings weighed approximately 100 Kg (combined), and produced an acceleration signal of approximately ± $10\mu$Gal. We were very lucky that the bronze rings were just large enough to fit over the vacuum chamber of the gravimeter, but we were not able to get the mass low enough to reach its lower optimal position — the rings were too tall.

The lifting arrangement relied upon a counterweight to balance the weight of the source mass. The translation of the chain and counterweight meant that the movement of the source mass could not be treated simply as a translation of the perturbing acceleration field about the start-of-drop position. This complication, coupled with an ugly system of bearings, hangers, and plates, made the mass arrangement difficult to model accurately.

The FG-5 gravimeter we used had a standard (at the time) data acquisition system that was only capable of recording 180 position-time pairs for each drop of the proof mass. Nevertheless the drop-to-drop scatter in the data was not much worse than the best data we would ever take (only about 20% greater scatter). A

Figure 6.1: A photo of the source mass and a portion of the lifting assembly of the bronze proof-of-concept experiment. Note that the mass is made only two cylinders. It was supported by a chain, and was guided by three rods.

sample of the data is plotted in Figure 6.2. This data acquisition system had some other disagreeable properties. There was a delay of approximately 30 milliseconds between the start of the drop and the start of data acquisition. This was due to the time required for the system to initialize after receiving the trigger signal indicating the start of the drop. Thus the fringes recorded by the system were not well connected to the position of the start of the drop. The system could not keep up with the fringe data from the interferometer, and would miss fringes towards the end of the drop.

Because our software implementation of the theoretical system was not completed at the time of the bronze mass experiment the source mass was not correctly placed in its optimal positions. The data from this run were taken with a variety of upper and lower source mass positions, including some scans where the source mass was slowly stepped through its range.

All in all the bronze mass run was a valuable learning experience but not much more. Figure 6.3 shows a plot of the results of this first data run. The results are clearly “in the ball park” of the correct value of G, though they are also only of proof-of-concept quality.

The bronze mass experiment illustrated the need for a robust system with improved signal-to-noise and a simpler mass arrangement (for modeling). During 1996 we worked on the completion of the software system as well as the design and construction of the apparatus to be used in the actual measurement.

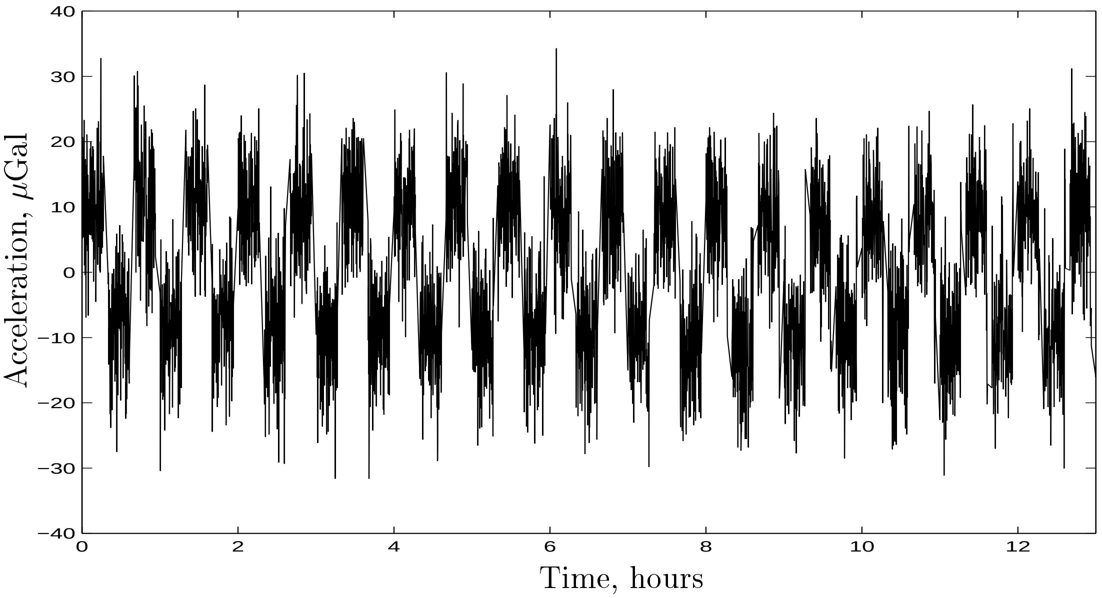

Figure 6.2: A 13 hour sample of acceleration data from the bronze proof-of-concept experiment. Note that the signal of the bronze ring source mass has an amplitude of only 10 $\mu$Gal.

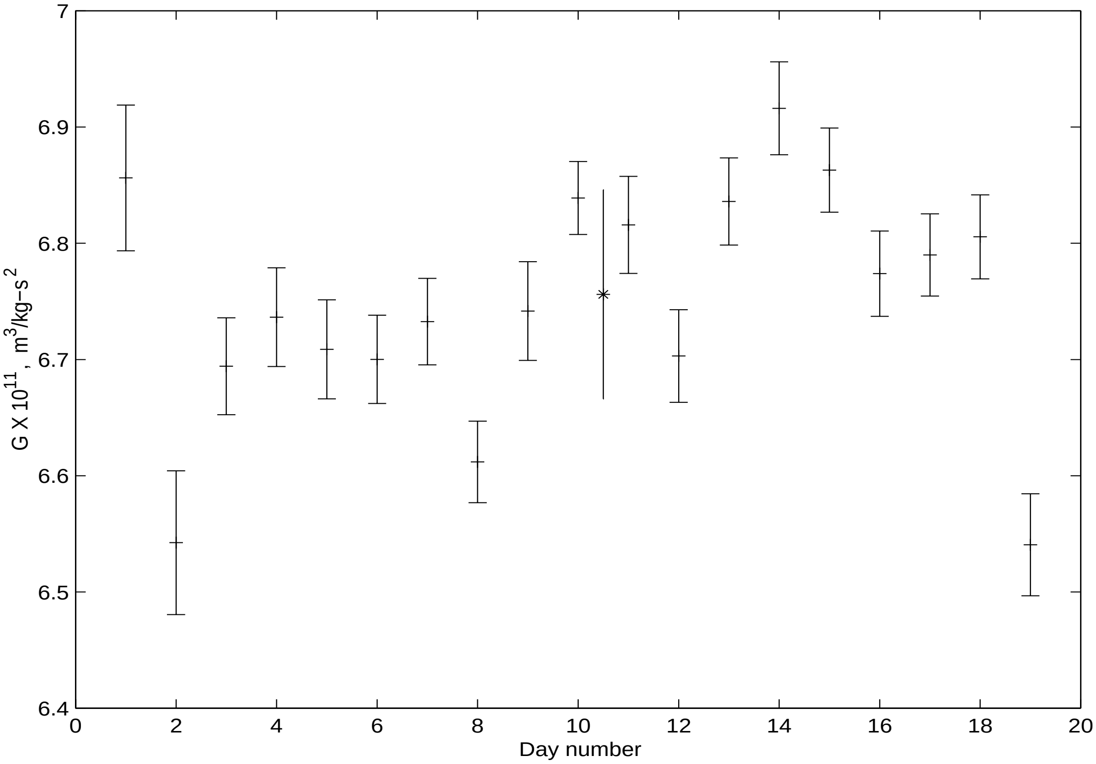

Figure 6.3: Results of the bronze mass proof-of-concept experiment. The value marked with an asterisk represents the final value of the data run. For comparison, the accepted value of G is 6.6726 ± 0.0009 X $10^{-11}$ m$^3$/kg-s$^2$.

### 6.1.2 May 1997 Experiment

The May 1997 experiment used the lifting assembly and apparatus described in Chapter 3. By this point we had developed a sophisticated software system to calculate the proper source mass positions and to analyze data. The gravimeter was equipped with a new data acquisition system that allowed four times denser data than could be recorded previously. This was expected to reduce the drop to drop scatter of acceleration measurements by close to a factor of two (sqrt(4) = 2).

The high-speed data acquisition system solved the problems with missed fringes late in the drop and the uncertainty in the delay between the start of drop and the start of data acquisition. There was still a delay for the fringe signal frequency to rise past 700 Hz (where it could trigger the discriminator) but this was a negligible error source (a fringe signal above 700 Hz is achieved in just a few microns of vertical displacement).

The nine days of data that we took (over a 13 day period) gave the results shown in Figs. 6.4 and 6.5. In order to compare the internal and external scatter of the data I averaged individual differences in a variety of bin sizes. With a bin size of 20, 30, 50, and 81 the external scatter was 1.5, 1.3, 1.6 and 1.3 times as large as the internal. Averaging these results indicates that a reasonable ratio is 1.4; there is more variation in the G value from bin to bin than would be expected from the scatter within each bin.

The difference values (Fig.6.6) produce a power spectrum that is flat, however, suggesting that there was no unusual power at low frequency (that could strongly bias our result). The lack of a clear drift over the whole data set supported this assumption. Fitting the individual difference with a line gave a drift in $\delta g_o$ equivalent to 0.20 ± 0.13 $\mu$Gal from the start of the data run to the end (13 days). The drift estimate is suggestive, but not clearly indicative of a drift.

The reduced chi-squared comparison of the daily results to a Gaussian (as presented in [48, 49]) returned $\tilde{\chi}^2 = 0.8$ (40% probability). This indicates good agreement with a Gaussian. Calculating the reduced chi-squared from the individual differences, however, returns a value of $\tilde{\chi}^2 \approx 3$ (10% probability).

These results do not damn the 1997 data run, but they do suggest the presence of either a random coupling of environmental signals to the G-experiment, or the random modulation of an unknown systematic. Because the experiment was run during a hot spell in Colorado we attributed the low-frequency scatter to air conditioning cycles correlating with the experiment. The air conditioning at the site was observed to switch on and off at slightly higher frequencies than the source mass was modulated.

An estimate of the bias introduced by the underlying signal could be made by modeling it as a sinusoid in the data and calculating the offset introduced by a fractional period. Alternately an estimate of the effect could be made by selectively removing bins of data, and recording the effect on the mean. These two methods returned estimates of the bias that agreed to 10%. Using the second method, we adopted an estimate of 450 ppm for the random drift bias error in the 1997 result.

The final result of the 1997 was calculated in a more complicated way than by simply averaging differences. Instead G was calculated as a function of the first fringe fit (FFF) from the $\delta g_o$ curve found in Section 4.3. Figure 6.7 is a plot of this curve. The value of the constant produced by the data depends on the choice of the first fringe fit. I characterize this dependence as weak because the standard deviation of the values computed with different FFFs is 1/3 of the uncertainty of each result with a single choice of FFF. A component of the "noise" between the different start fringes was due to the fact that we extract G from a slightly different sets of data for each value.

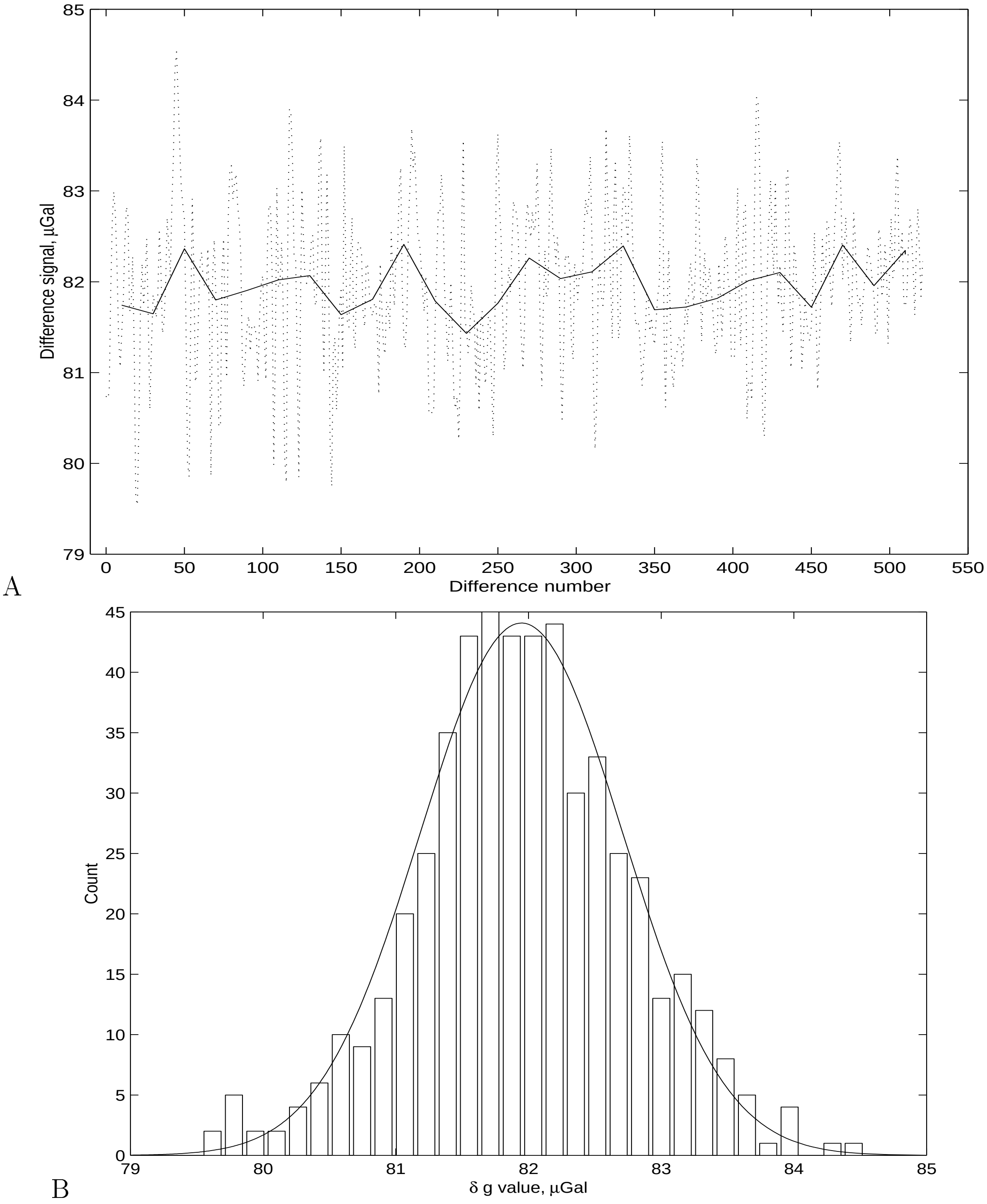

Figure 6.4: Data from the 1997 experiment. A) Differences as measured in Sec 4.2.1. The dotted line represents the individual differences, while the solid line is the difference value averaged over blocks of 20 individual values. B) Histogram of the differences. The solid line is the best fit Gaussian curve.

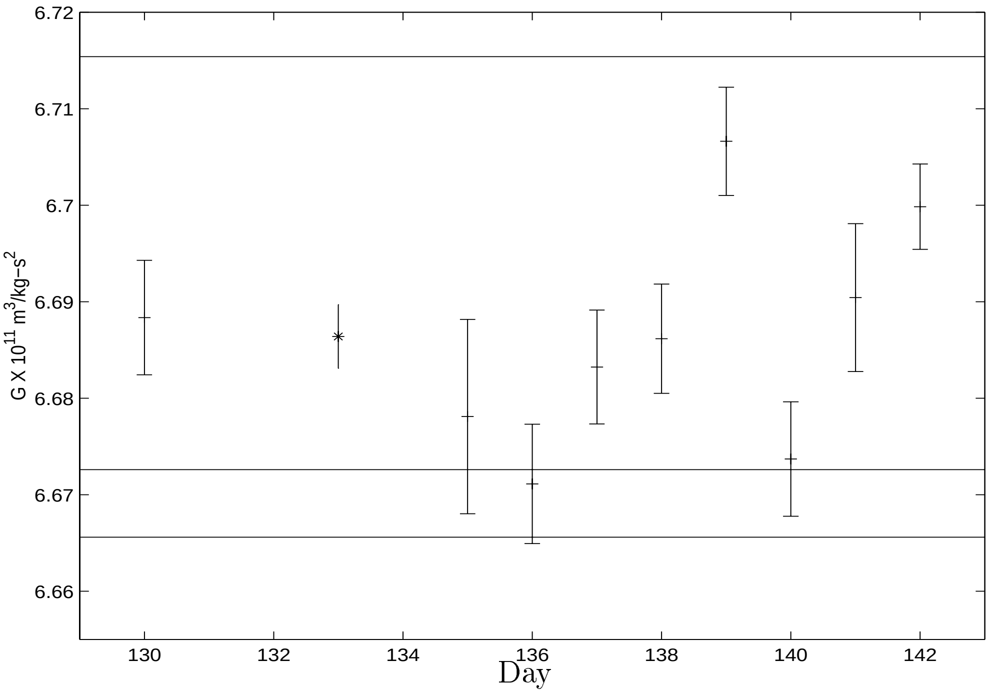

Figure 6.5: Results of the May 1997 experiment. Daily results. The value marked with an asterisk represents the final value of the data run. The error bars represent a single standard error, only. The lowest horizontal line represents the 1995 New Zealand result [15], the middle line is the accepted value [4], and the upper line is the 1995 German result [14].

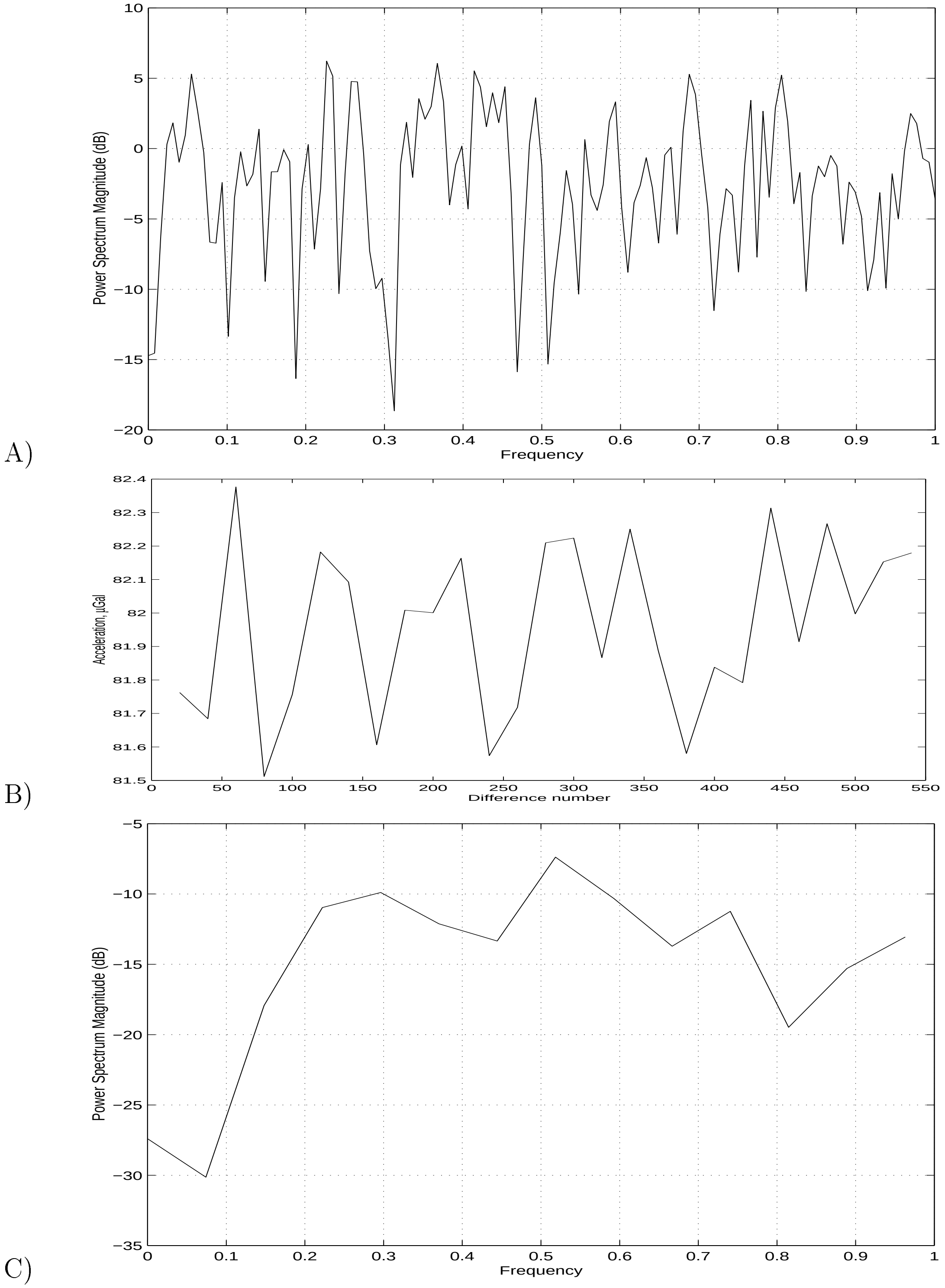

Figure 6.6: Power spectral analysis of individual differences from the 1997 experiment. A)The power spectrum from differences calculated using method two (of Sec 4.2.1). Only half of the differences were used in the calculation to avoid any correlation between the individual values. B)The difference values averaged in groups of 20. This corresponds to periods of approximately 7 hours. C) The power spectrum of the binned data. The power spectrum with bins of 3.5 hours looks much same, with just a bit more definition.

The variation in the value raises the question of which value is appropriate to summarize the result. Because we don't expect that G be physically dependent on the FFF, a fit of all this data to a flat line gives a reasonable indicator (the weighted mean value) for our best estimate for G.

Some portion of the dependence of the measured G on the FFF was systematic. The data points in Fig. 6.7 are not completely independent, as is especially obvious between fringes 24–30 and beyond fringe 60. An estimate of the sensitivity of our "best value" to possible systematics in the data can be made by calculating the change in the value when different portions of the curve are excluded from the calculation of the mean (this assumes that there is no significant DC systematic bias). Figure 6.8 is a plot of the error estimate in G as a function of start fringe. The two "especially suspicious" regions between fringes 24–30 and 60 onwards are marked. The mean value is very insensitive to the G-values in these regions, in part because of their larger uncertainties. The weighted mean value shifts only $1/10^{th}$ of a standard uncertainty when these data points are excluded. The point that the exclusion of this data may be considered arbitrary is moot because our results are insensitive to this manipulation.

The value of G extracted from the 1997 run is the weighted mean of the data shown in Figure 6.7 with a statistical uncertainty of 450 ppm. The statistical uncertainty was based on the complete data set evaluated from fringe 20 to 640 (a region chosen for its compatibility with absolute gravity measurements). The error bar includes estimates of error sources as discussed in Section 5.2 and Appendix B. The 1997 result is:

$$\mathrm{G} = (6.6863 \pm 0.0015 \pm 0.0042 \times 10^{-11}\mathrm{m}^3/\mathrm{kg} - \mathrm{s}^2$$

where the first uncertainty estimate is the root sum square of the systematic errors of Table 5.1 and the second uncertainty is the random error associated with

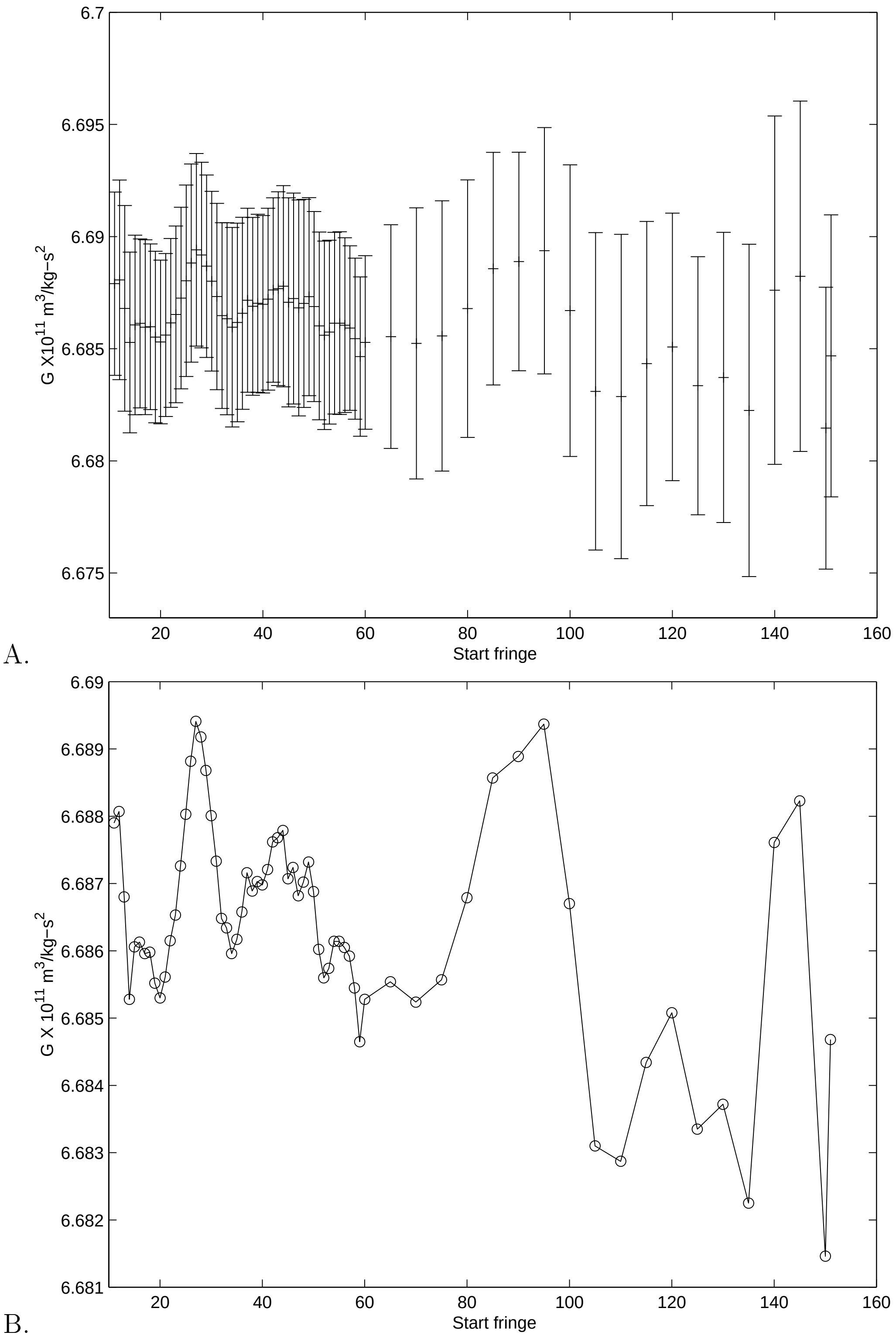

Figure 6.7: G as a function of first fringe fit to a fixed final fringe (#640). A) With error bars associated with the analysis of the complete 1997 data set with each particular choice of first fit fringe. B) Without error bars.

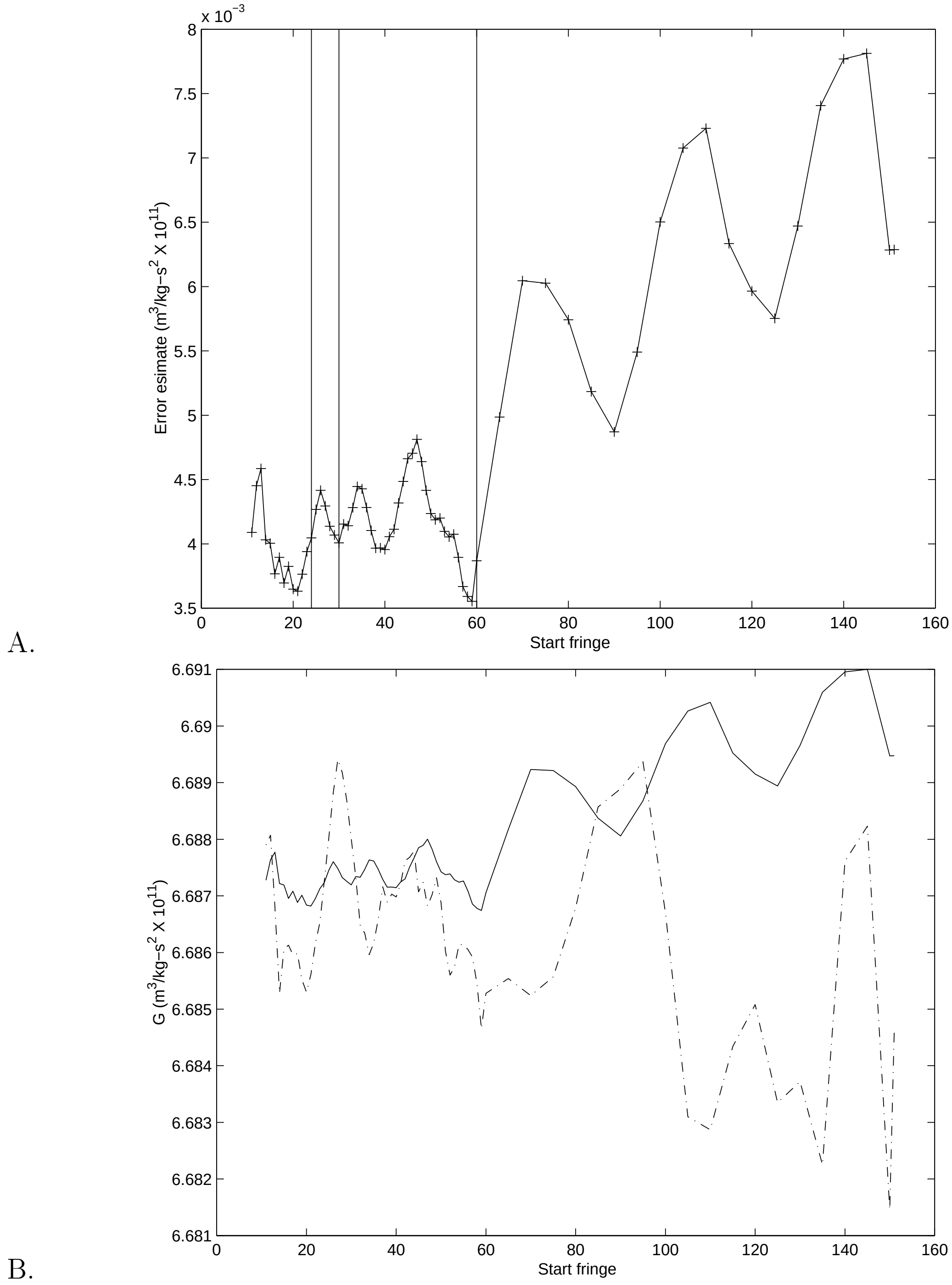

Figure 6.8: Statistical uncertainty in G as a function of first fringe fit to a fixed final fringe (#640). A) The error estimates plotted against start fringe. The vertical lines are at fringes 24, 30, and 60. B) Error (—) scaled for comparison to the actual G values (–·–) error.

a bias in the data from the underlying signal and the statistical uncertainty. The combined statistical and systematic error estimate is 0.0045 x $10^{-11}$ $m^3$/kg-$s^2$ (670 ppm).

### 6.1.3 May 1998 Experiment

We made several improvements to the apparatus for the 1998 data run. Concerned about thermal signals we added a layer of insulation (Cryotex) around the whole lifting assembly and a separate loose thermal shield for the laser and electronics system of the gravimeter. We increased the frequency of modulation of the source mass position by nearly a factor of two, decreasing the correlation of random environmental signals and machine drifts to the G measurement.

One way temperature signals could influence the scatter in the free fall experiment was by causing tilts of the laser verticality (see Section 5.2.4). For this reason we used a fiber-optic interferometer system that had shown improved verticality stability over the standard FG-5 interferometer(see Sec. 3.1.3 for discussion).

We directly measured the motion of the air-vacuum interface throughout the experiment. We hoped that this auxiliary data would help us to place bounds on the differential airgap signal (Section 5.2.1). In addition to airgap data we logged the shaft-encoder voltage (Sec. 3.1.1.2) and ion-pump voltage[1] for each drop.

We attempted to increase the precision of the experiment by using a super spring that had demonstrated superior performance, and by doubling the dropping rate from a drop every 10 seconds to one every 5 seconds.

We made several "miscellaneous" changes. To remove the magnetic signal of the drive motor (Section 5.2.8) and reduce magnetic damping of the airgap motion (Section 5.2.1) magnetic shielding was placed around the motor and ion pump. To improve the performance of the lifting assembly and decrease deformation of the source mass the support plates (Section 3.2) were replaced with thicker plates

---

[1] The ion pump voltage gave a crude estimate of the vacuum pressure in the dropping chamber.

with extra support rods.

Figures 6.9 and 6.10 show the results of these improvements. The scatter in set-to-set g values increased by a factor of 1.9. The the scatter in $\delta g_o$ increased by a factor of 1.5. The increase in scatter was not seen at the high frequency of drop measurements, but only in set-to-set scatter. The ratio of internal to external scatter increased to 1.9. The value of G extracted from this data, however, was consistent with the 1997 value. We don't know what caused this unexpected increase in scatter.

There was some coherence between the individual $\delta g$ differences, as in Figure 6.10. The histogram of the whole set of data, however, displays a normal distribution (Table 6.1 gives the major moments of the distribution, with "typical" values for the kurtosis and skew), and the power spectrum (Fig. 6.11) is reasonably flat. This suggests that the correlations are random. A fit of a line to the data gives a drift value corresponding to a change of $0.065 \pm 0.10 \mu$Gal from the beginning to the end of the data set (15 days). Assuming that the signal was random, a bias error estimate of 0.004 x $10^{-11}$ m$^3$/kg-s$^2$ (600 ppm) was adopted. This was calculated in the same way as in the 1997 data run.

| Moment | Value | Typical |
|---|---|---|
| Mean | 82.8633 $\mu$Gal | |
| Average Deviation | 0.90 $\mu$Gal | |
| Standard Deviation | 1.16 $\mu$Gal | |
| Variance | 1.34 $\mu$Gal$^2$ | |
| Skewness | 0.12 | 0.1 |
| Kurtosis | 0.34 | 0.24 |

Table 6.1: Main moments of the 1998 experiment distribution of $\delta g$ observations. The values for the kurtosis and skew are close enough to "typical" values to be considered normal.

The 1998 data displays much the same scatter in G as a function of first fringe fit as the 1997 data (Figure 6.1.3). It, too, displays coherence between

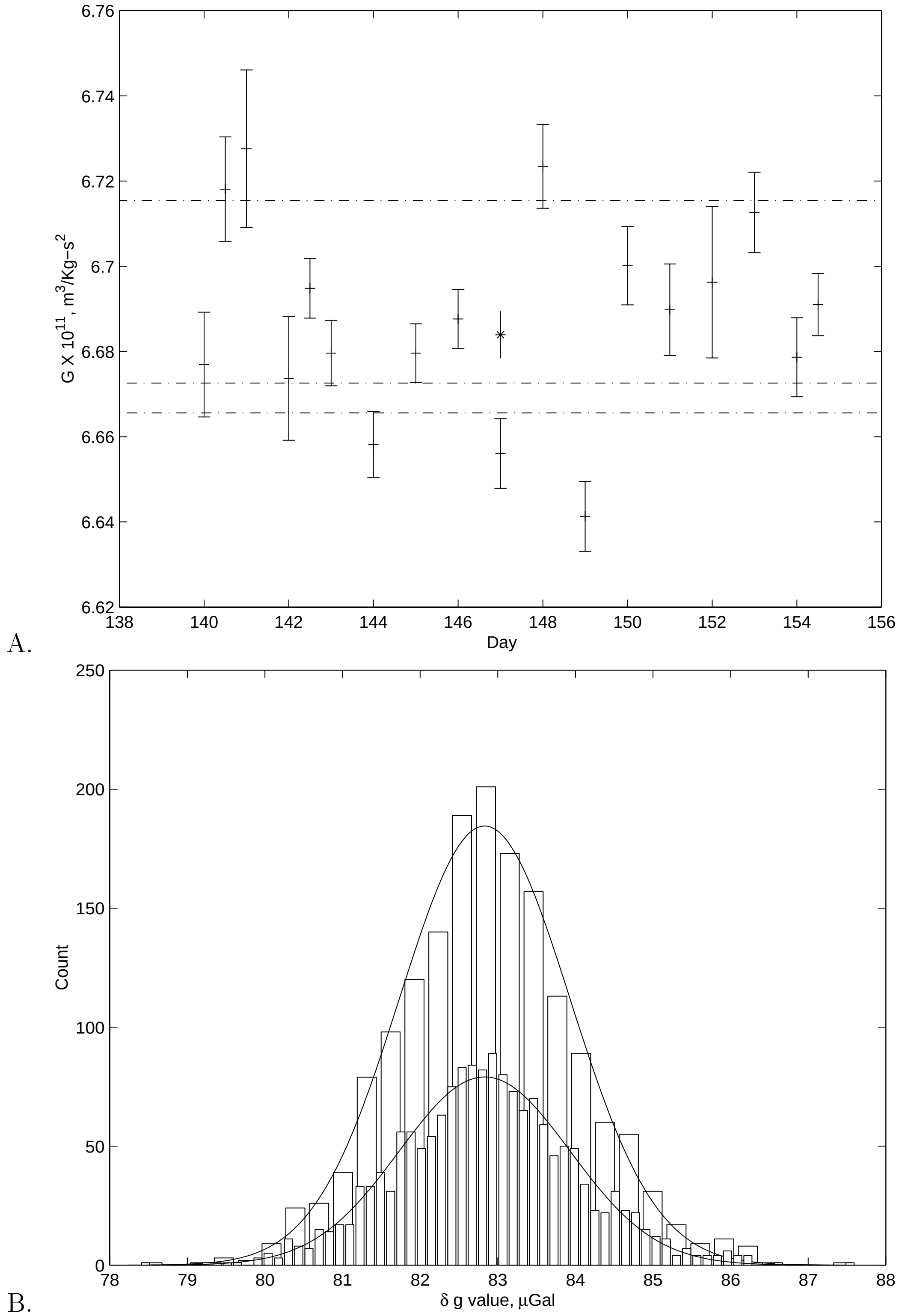

Figure 6.9: Results of the 1998 data run. A) Daily results. The horizontal lines represent values for G from other recent experiments: The upper line is the PTB result, the middle line is the accepted NBS result, and the low line is the New Zealand Standards result. The daily results reflect the coherence obvious in Fig. 6.10. B) A histogram of the individual 1998 $\delta g$ differences. The smooth curves represent the normal probability for the mean and variance of this data. The larger curve consists of 1660 points in 30 bins, while the lower curve is the same data in 70 bins.

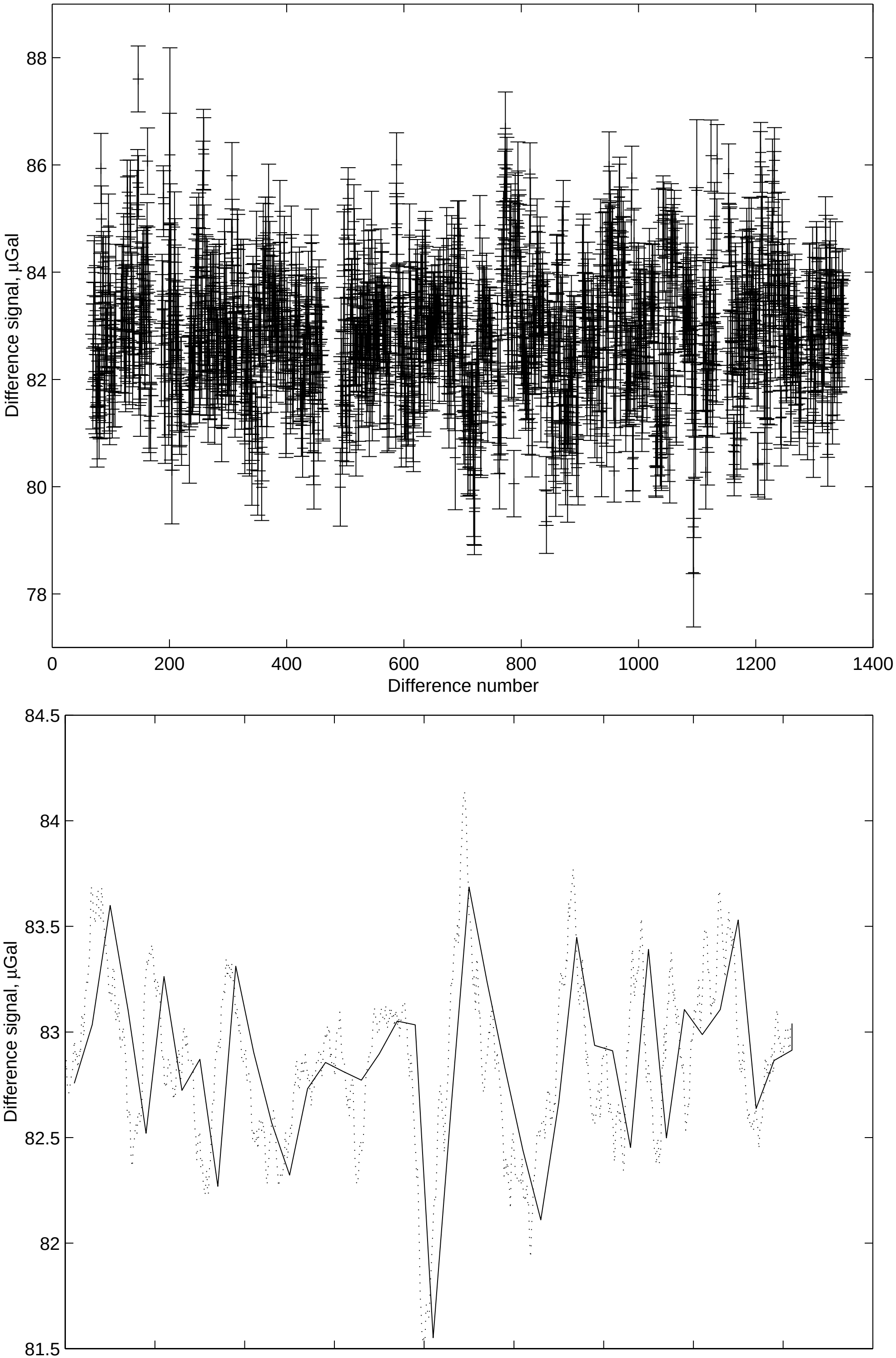

Figure 6.10: Individual differences from the 1998 data run. A) The differences, calculated using method 3 of Sec. 4.2.1. B) The differences averaged in bins of width 40. The dotted line is a running average, while the solid line is simply binned data.

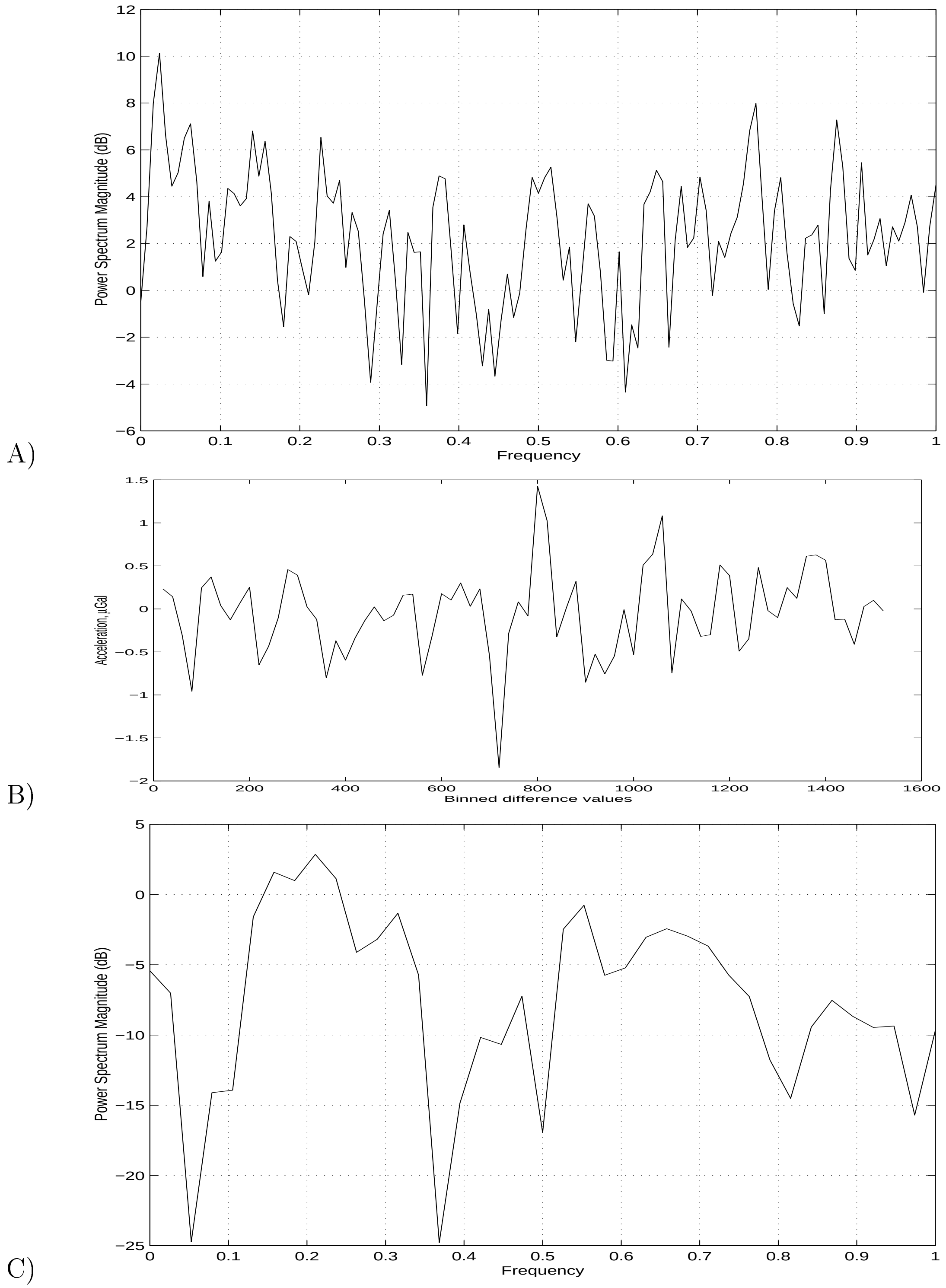

Figure 6.11: Power spectral analysis of the individual differences from the 1998 experiment. A) The power spectrum from differences calculated using method 2 of Sec. 4.2.1, but only every other value was used in the power spectrum to avoid correlated data at the higher frequencies. B) The difference data was placed into bins representing 3.6 hour periods. C) The power spectrum of the binned data.

the values. Once again the weighted mean value of G given by these results is insensitive to exclusion of suspicious data, changing by less than $1/10^{\mathrm{th}}$ sigma when the data is removed. The weighted mean of this data (associated with 700 ppm statistical uncertainty and adjusted with the airgap correction) forms the 1998 data run result:

$$\mathrm{G} = (6.6896 \pm 0.0013 \pm 0.0062) \times 10^{-11}\mathrm{m}^3/\mathrm{kg} - \mathrm{s}^2$$

where the first uncertainty is root sum square of the systematic errors of Table 5.1 and the second uncertainty is the RMS error associated with a bias in the data from the underlying signal and the statistical variation of the data. The combined statistical and systematic error estimate is 0.0063 x $10^{-11}$ $\mathrm{m}^3/\mathrm{kg}\text{-}\mathrm{s}^2$ (940 ppm).

## 6.2 Combined Results

The large underlying signal in the 1998 data could represent a randomly modulated systematic error. If this was the case there could be a systematic bias that we would not be able to identify in the data. Consider the hypothetical situation that our assessment of the thermal coupling between the source mass and gravimeter was vastly underestimated. Clearly the coupling would not exist if all components of the gravimeter and the source mass were the same temperature. If there was a fixed offset in the source mass temperature, however, a constant bias to the $\delta g$ signal would occur. And if the source mass temperature had a constant offset with a random time varying component data such as we've seen might have resulted. It is not clear that there was such an offset, but to be properly cautious, we must deal with this possibility.

The only information that we have that there is no low frequency or DC bias in our results is the agreement between our two data runs. The fact that they were not completely independent is unimportant because the scale of known

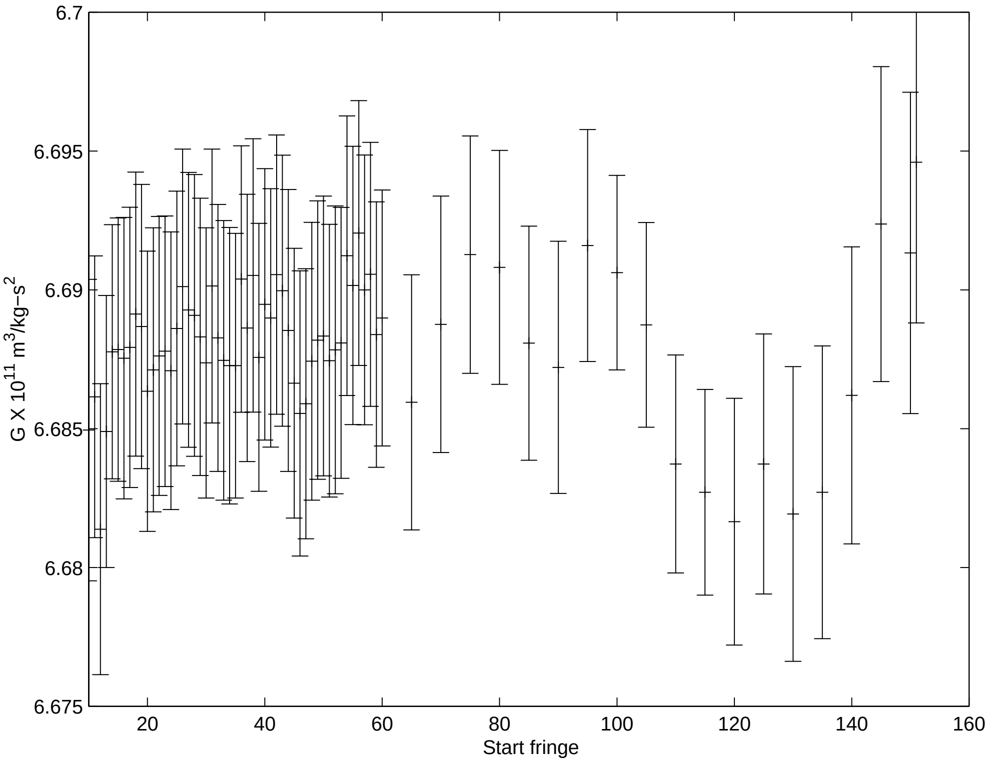

A

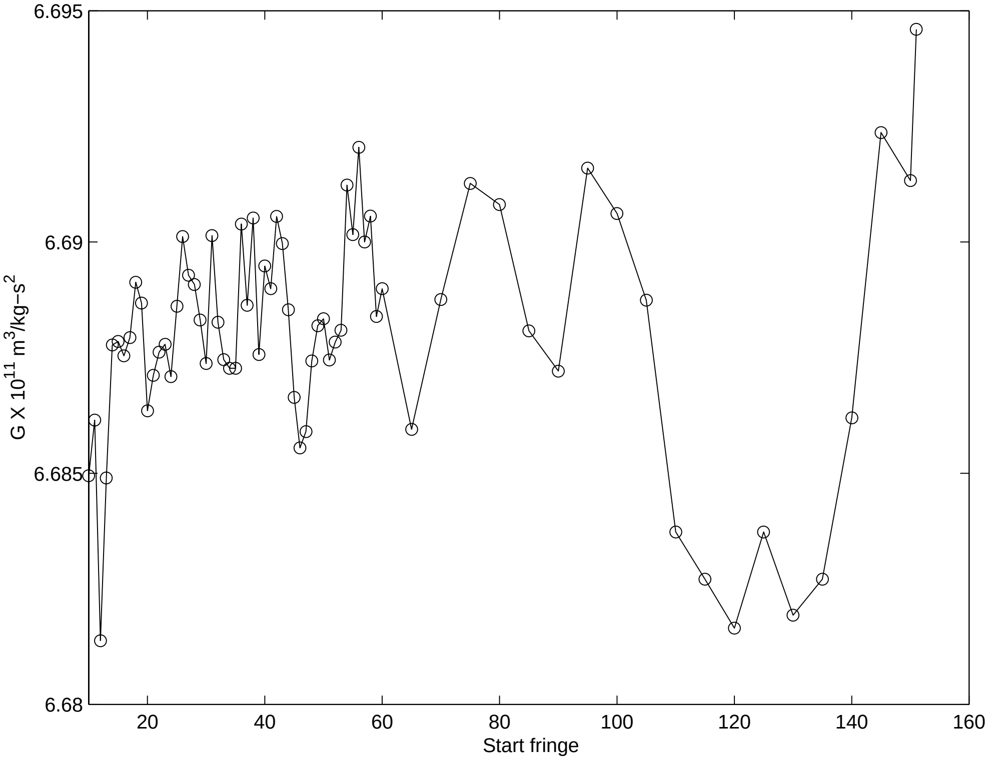

B

Figure 6.12: G as a function of first fringe fit to a fixed final fringe ($N^{o.}$ 640). A) With error bars associated with the analysis of the complete '98 data for each particular value of the first fringe fit. B) Without error bars.

systematic errors is very small compared to statistical and possible systematic uncertainties. We can make an estimate of our uncertainty arising from such a low-frequency bias by taking the difference of the two runs. This difference is only 400 ppm (the two results don't differ in a statistically significant way), but the uncertainty in the difference is 1100 ppm (0.11%).

For the final result of the free fall experiment we combine the 1997 and 1998 data runs. The two experiments were not fully independent; they used the same tungsten masses arranged in roughly the same orientations. Therefore the correct combined error of the two data runs is slightly larger than the uncertainty in the mean of the combination. Adopting the uncertainty in the difference as an estimate of a possible underlying systematic offset increases the uncertainty in the mean to a level were these distinctions are unimportant.

The combined final result for the free fall experiment is:

$$\mathrm{G} = (6.6873 \pm 0.0076)\ \times 10^{-11}\ \mathrm{m}^3/\mathrm{kg}-\mathrm{sec}^2.$$

The uncertainty corresponds to 1150 ppm, 0.12%. This result is shown with all the daily results and some other recent results in Figure 6.13. This value for the constant lies 1.5 standard errors above the accepted value, and 3 standard errors below the German PTB result. Although this result does not uphold the PTB value at all, it does lend some support to the region above the accepted value.

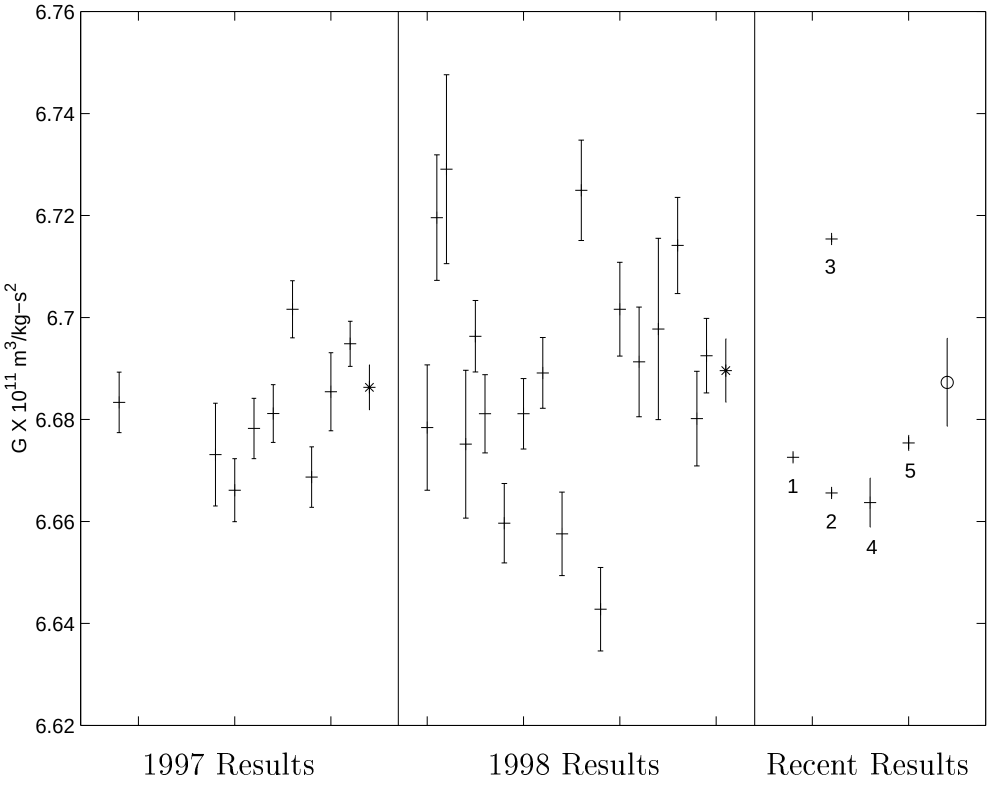

Figure 6.13: A plot of G results. At the right side of the figure, recent results: 1. NBS. 2. New Zealand Standards. 3. PTB. 4. Wuppertal. 5. Zürich. The final free fall result is the value marked with a circle, and includes all error estimates. The other results marked with crosses are the daily results of the free fall experiments. The error bars of the daily results represent statistical uncertainty, only. The weighted mean result of each data run is marked with an asterisk. These values include the error estimates of Table 5.1, statistical uncertainty, and the estimate of bias errors from the underlying signals.

# CHAPTER 7

# CONCLUSION

The free fall determination of G is conceptually simple. An idealized model describing the motion of a falling mass has been well understood for literally hundreds of years. The study of objects moving in gravitational fields begins at the start of an education in physics.

Yet somehow G measurements are full of complexity, subtlety, and beauty — and the free fall experiment is no exception. The complexity of the experiment arises from the fact that our measurement pushes on the boundary between the idealized model and the hard reality of measurement. The calculation of the mutual attraction of the source mass and the proof mass involved over 6000 six-dimensional integrals calculated at 1000 positions along the drop range of the test mass.

The subtleties of the experiment are found mostly in the search for systematic errors. The source mass influences the resonances of the lifting assembly in different ways, depending on its position. These resonances, which extend to below 70 Hz, affect the response of the floor to the changing weight of the dropping system. The weight changes because portions of the dropping chamber (the co-falling chamber and the proof mass) become weightless during the drop. Thus the change in source mass position affects the airgap measurement (Section 5.2.1).

The beauty of the free fall method lies in the hints of simplicity that remain in the experiment. The fact that the sensing mass of the experiment is unsupported means that dependencies on material properties are greatly reduced if not completely removed. The fact that the measurement is differential means that common mode errors of gigantic magnitudes can be tolerated. The modulation rate of the source mass pushes the gravity signature of the source masses beyond the frequencies of most environmental signals.

## 7.1 Results

Our final value for G is

$$\mathrm{G} = (6.6873 \pm 0.0076)\ \times 10^{-11}\ \mathrm{m}^3/\mathrm{kg} - \mathrm{sec}^2.$$

This result incorporates error estimates of random drift bias errors and an estimate of a DC shift between the results of the two data runs. This was not the ideal situation, as made clear by Churchill Eisenhart:

> I realize that some of the subjectively estimated uncertainties tabulated by experimenters are intended, when combined "in quadrature" with the statistical standard error of the mean, to provide an inflated "standard error" of the mean that can be used to "provide an indication of how closely the result of this experiment is likely to agree with other results that might be obtained if the entire experiment were carried out afresh 'from the beginning,' " but experience shows that this is a delusion: there is no substitute for comprehensive realistic repetitions of the entire experiment!
> —Churchill Eisenhart [50]

It is unfortunate that the gravimeter system was not available for in depth testing with the source mass system, or for additional experimental runs. In some sense it was this lack of time with the gravimeter that was our greatest nemesis. It was for this reason that we had to adopt the difference in the results of the 1997 and 1998 data runs as an estimate of systematic bias errors. This estimate is not unreasonable:

> The uncertainty assigned to a precision measurement ideally should not be solely determined by random measurement errors, but should partly be the result of subjective judgments by the experimenter on the accuracy of his work." — Abstract by Peter Franken [51]

## 7.2 Future

At the time that we did our experiments it was not quite clear to what precision we would be able to extend the performance of the FG-5. Now, with the lifting assembly packed away and the tungsten masses waiting for their next leading role, I believe I can clearly see the future of the free fall method.

There are only two ways in which the free fall experiment will be continued. In a series of small improvements, or in a single big step. The combined uncertainty of our results is 1300 ppm, the systematic errors arising from mass homogeneities, modeling errors, and positioning (internal to the source mass) only rear their ugly heads at the level of 100 ppms. Clearly our results can be improved dramatically if the sources of the underlying drifts could be identified and controlled.

If the random signal were removed from our data and questions of low-frequency biases were laid to rest then a result at the level of 300 ppm could be achieved with the present system. Clearly our data would be close to this level if not for the underlying signals.

I have thought of several lines of attack that might be used to track down the drift source. For example, "double moving" the source mass in between sets might give information about spring effects. After each set of data the source mass would be moved half way to its alternate position, and then immediately moved back to its original position. Increased scatter in this situation would indicate that the move was linked to the noise source.

Once the source of the drift was identified, however, and a measurement at the level of 300 ppm completed, further improvement of more than a factor of two would be very difficult to achieve. In this context many of the improvement ideas that I entertained are simply not worth the effort. The "return" on small improvements to the system would not be worth the investment. A dramatic scale-up of the system would be more interesting.

A large scale-up of the experiment would involve a large increase in the time, money and energy spent on the determination. The experiment would be performed in its ideal incarnation, incorporating many ideas independently of the constraints of weight and portability that influenced the current gravimeter system.

The entire dropping assembly would be custom designed to operate at a single location. It would include a simplified proof mass less sensitive to eddy currents, and counterweighted to reduce vibration. The position of the test mass would be recorded at every fringe crossing, not each 500th. The interferometer system would be used to reference the start-of-drop position to the source mass. External magnetic fields would be removed either with shielding or active control. The vacuum pump could be moved far away from the rest of the system. The laser would be, for example, a frequency doubled Nd:YAG green laser. This type of laser can be stabilized to better stability than the HeNe, without the large frequency dither of the current system.

The source mass would be located in the same evacuated room[1] as the test mass. The source mass would be made not of just twelve tungsten billets, but of hundreds of smaller precision machined objects placed as close to the drop as possible. They would be supported by a system capable of switching their

---

[1] Including thermal isolation, naturally. A Big Step!

positions after every drop.

A custom super spring would be made for the experiment. Perhaps an multi-dimensional active isolation unit as have been developed for use in gravity wave detectors could be incorporated into its design [52]. The spring could be located far from the dropping system (perhaps in the same vacuum) to reduce coupling of floor motions.

It is certainly reasonable to wonder whether such a costly experiment using the free fall method will ever be carried out. The free fall measurement currently suffers from lower signal-to-noise ratio than some other comparable experiments. It also also has exhibited unexplained drifts. But the great characteristic of the method is its use of an unsupported mass in a system that, in theory, is extremely simple.

There are several G-experiments that are expected to produce results by the end of this year. If their results are consistent, and the value of G can be stated with confidence and precision, then I don't believe there is a strong future for the free fall method. If the results continue to show great deviation in G, however, then I believe that the conceptual simplicity of the free fall method, coupled with its lack of dependence on material properties, will provide reasonable impetus for an improved experiment.

I know what must be done to solve the problems inherent in the measurement of G. Intelligent thought, unrelenting effort, big money, and a dose of luck must be pooled for one carefully planned, constructed, and executed measurement. I hope that the work presented in this thesis will help future experimenters (as it helped me) to grasp the challenge of the measurement of G, and to recognize some of the possible pitfalls in that measurement.

# BIBLIOGRAPHY

[1] R. Wagoner, W. Fowler, and F. Hoyle Astrophysics Journal, vol. 148, 1967.

[2] H. Cavendish, “Experiments to determine the density of the Earth,” Phil. Trans. R. Soc. London, vol. 88, pp. 469–526, 1798.

[3] R. Heyl. Res. Nat. Bur. Stand. (US), 1930. pg. 1243-1290.

[4] G. G. Luther and W. R. Towler, “Redetermination of the Newtonian gravitational constant, G,” Physical Review Letters, vol. 48, no. 3, pp. 121–123, 1982.

[5] M. Sagitov, V. Milykov, Y. A. Monakhov, V. Nazarenko, and K. G. Tadzhikinov, “A new determination of the cavendish gravitational constant,” Dokl. Akad. Nauk. SSSR Earth Sci., vol. 245, pp. 20–22, 1981.

[6] O. Karagioz, V. Izmaylov, N. Agafonov, E. Kocheryan, and Y. Tarakanov, “The determination of the gravitational constant with an evacuated torsion balance,” Izvestiya Akademii Nauk SSSR, Fizika Zemli, vol. 12, no. 5, pp. 106–111, 1976.

[7] G. T. Gillies, “The Newtonian gravitational constant: Recent measurements and related studies,” Rep. Prog. Phys., vol. 60, pp. 151–225, 1997.

[8] C. H. Bagley, A Determination of the Newtonian Constant of Gravity Using the Method of Heyl. PhD thesis, University of Colorado, Boulder, Colorado, 1996.

[9] W. A. Koldewyn, A New Method for Measuring the Newtonian Gravitational Constant, G. PhD thesis, Wesleyan University, Middletown, Connecticut, 1976.

[10] K. Kuroda, “Does the time of swing method give a correct value of the Newtonian Gravitational constant?,” Physical Review Letters, vol. 75, pp. 2796–2798, October 1995.

[11] R. Newman and M. K. Bantel, "Preparation for a determination of g using a cryogenic torsion pendulum," *Proceedings of the Eighth Marcel Grossmann Meeting on General Relativity*, June 1997.

[12] S. Matsumura, N. Kanda, T. Tomaru, H. Ishizuka, and K. Kuroda, "A measurement of the frequency dependence of the spring constant," *Physics Letters A*, vol. 244, pp. 4–8, July 1998.

[13] M. K. Bantel and R. D. Newman, "Measuremnet of torsion fiber anelastic properties in preparation for a new measurement of g," *Proceedings of the 1998 Conference on Precision Electromagetic Measurement*, 1998.

[14] W. Michaelis, H. Haars, and R. Augustin, "A new precise determination of Newton's gravitational constant," *Metrologia*, vol. 32, pp. 267–276, 1995/96.

[15] M. P. Fitzgerald and T. R. Armstrong, "Newton's gravitational constant with uncertainty less than 100 ppm," *IEEE Transactions on Instrumentation and Measurement*, vol. 44, no. 2, pp. 494–497, 1995.

[16] A. Schumacher, U. Kleinevoβ, H. Schütt, *et al.*, "Determination of the gravitational constant G using a Fabry-Pèrot pendulum resonator," *Proceedings of the 1998 Conference on Precision Electromagnetic Measurement*, July 1998.

[17] J. Schurr, F. Nolting, and W. Kündig, "Gravitational constant measured by means of a beam balance," *Physical Review Letters*, vol. 80, pp. 1142–1145, Febuary 1998.

[18] H. Walesch, H. Meyer, H. Piel, and J. Schurr, "The gravitational force at mass separations from 0.6m to 2.1m and the precise measurement of G," *IEEE Transactions on Instrumentation and Measurement*, vol. 44, pp. 491–493, 1995.

[19] H. Walesch, H. Meyer, H. Piel, and J. Schurr, "Determination of the gravitational constant G using a Fabry-Péreot pendulum resonator." Available via Internet at: http://wpos6.physik.uni-wuppertal.de:8080/ gravi.

[20] H. de Boer, H. Haars, and W. Michaelis, "A new experiment for the determination of the Newtonian gravitational constant," *Metrologia*, 1987.

[21] F. Nolting, J. Schurr, and W. Kündig, "Determination of G by means of a beam balance," *Proceedings of the 1998 Conference on Precision Electromagnetic Measurements*, July 1998.

[22] J. E. Faller, *An Absolute Interferometric Determination of the Acceleration of Gravity*. PhD thesis, Princeton, 1963.

[23] R. L. R. III, *Super Spring — A New Type of Low-Frequency Vibration Isolator*. PhD thesis, University of Colorado, Boulder, Colorado, 1983.

[24] T. M. Niebauer, New Absolute Gravity Instruments for Physics and Geophysics. PhD thesis, University of Colorado, Boulder, Colorado, 1987.

[25] D. S. Robertson, "Treating absolute gravity data as a spacecraft tracking problem," Metrologia, vol. 33, pp. 545–548, 1996.

[26] D. Brouwer and G. Clemence, Methods of Celestial Mechanics. New York: Academic Press, 1961.

[27] W. H. Press, S. A. Teukolsky, W. T. Vetterling, and B. P. Flannery, Numerical Recipes in C. Cambridge University Press, second ed., 1992.

[28] W. H. Press, S. A. Teukolsky, W. T. Vetterling, and B. P. Flannery, "Numerical recipies routines and examples in c." Diskette, 1992.

[29] M. Winters, Model 100 Iodine-Stabilized HeNe Laser, Operator's Manual. Winters Electro-Optics, Inc., first ed., 1994.

[30] M. A. Zumberge, A Portable Apparatus for Absolute Measurements of the Earth's Gravity. PhD thesis, University of Colorado, Boulder, Colorado, 1981.

[31] W. A. Koldewyn, A New Method for Measuring the Newtonian Gravitational Constant, G. PhD thesis, Wesleyan University, Middletown, Connecticut, 1976.

[32] R. S. Davis, "Determining the magnetic properties of 1 kg mass standards," Journal of Research of the National Insitute of Standards and Technology, vol. 100, pp. 209–225, 1995.

[33] R. S. Davis, 1997. Personal Communication to J. Faller.

[34] L. Mansinha, "Barometric and gravimetric observations of the 1999 solar eclipse in europe," Proceedings of the 1997 AGU Chapman Conference on Microgal Gravimetry, 1997.

[35] R. Warburton and J. Goodkind, "Detailed gravity-tide spectrum between one and four cycles per day," The Geophysical Journal of the Royal Astronomical Society, vol. 52, no. 1, pp. 117–136, 1978.

[36] D. S. Robertson, G. Sasagawa, T. M. Niebauer, F. W. Klopping, J. E. Faller, and J. P. Schwarz, "Using spacecraft tracking algorithms to process absolute gravity data," German Geodetic Commission, row B, 1997.

[37] B. Putney, J. Brownd, and R. Gomez, Recursive Partitioned INversion of Large(1500 X 1500) Symmetric Matrices. Greenbelt, MD: NASA GSFC X-921-76-160, 1976.

[38] T. M. Niebauer, G. S. Sasagawa, J. E. Faller, R. Hilt, and F. Klopping, "A new generation of absolute gravimeters," Metrologia, vol. 32, pp. 159–180, 1995.

[39] F. Klopping, G. Peter, B. S. Robertson, K. Berstis, R. Moose, and W. E. Carter, "Improvements in absolute gravity observations," Journal of Geophysical Research, vol. 96, pp. 8295–8303, May 1991.

[40] Micro-g Solutions FG-5 Owner's Manual.

[41] J. Faller and P. Keyser. Research and development of an opto-electric bubble level, JILA.

[42] Personal communication with Jim Faller.

[43] D. J. Summner and A. K. Thakkrar, "Experiments with a 'jumping ring' apparatus," Physics Education, vol. 7, pp. 238–242, 1972.

[44] J. Hall, "Forces on the jumping ring," The Physics Teacher, vol. 35, pp. 80–83, Feb 1997.

[45] W. M. Saslow, "Electromechanical implications of Faraday's law: A problem collection," American Journal of Physcis, vol. 55, pp. 986–993, November 1987.

[46] J. Faller, W. Hollander, P. Nelson, and M. McHugh, "Gyroscope-weighing experiment with a null result," Physical Review Letters, vol. 64, no. 8, pp. 825–6, 1990.

[47] Personal Communication with Fred Klopping, September 1998.

[48] J. R. Taylor, An Introduction to Error Analysis, The Study of Uncertainties in Physical Measurements. Mill Valley, CA: University Science Books, 1982.

[49] P. R. Bebington and D. K. Robinson, Data Reduction and Error Analysis for the Physical Sciences. McGraw-Hill Inc., second ed., 1992.

[50] C. Eisenhart, "Contribution to panel discussion on adjustmenets of the fundamental constants," in NBS Special Publication 343. Precision Measurement and Fundamental Constants (D. Langenburg and B. N. Taylor, eds.), Proceedings of the International Conference held at the National Bureau of Standards, (Gainsburg, MD), pp. 509–517, Aug 1970.

[51] P. Franken, "Comments on the assignements of experimental uncertainties," in NBS Special Publication 343. Precision Measurement and Fundamental Constants (D. Langenburg and B. N. Taylor, eds.), Proceedings of the International Conference held at the National Bureau of Standards, (Gainsburg, MD), pp. 509–517, Aug 1970.

[52] Low-Frequency Active Vibration Isolation System, SPIE Proc. Conf. Vibration Monitoring and Control, (San Diego), July 1994.

[53] Metallwerk Plansee GmbH, D-8923 Lechbruck, High Density Alloys.

[54] S. Schwarz, “Lab book 2,” 1998.

[55] A. L. Steel, Stainless Steel Handbook. Allegheny Ludlum Steel Corporation, 1959.

[56] S. Schwarz, “Lab book 4,” 1998.

# APPENDIX A

# MASS METROLOGY

In an experiment in which we measured the mutual gravitational attraction of two complex masses it was important to describe the mass distributions as well as possible. If the size or mass of one (or both) of the objects were assigned an incorrect value, then our theoretical model would misrepresent the actual physical situation. Correctly describing the objects may sound like a simple task, but it was not. Density variations internal to the masses correspond to errors if they were not accounted for in the models. Unmodeled density variations could arise from voids in the material and from density gradients that occur due to cooling effects. Not to mention that both the source and test masses (our two objects) were made of many of eensy-weensy bits and pieces.

The source and proof mass were each subject to errors that differently affect the experiment. The source mass created an acceleration field that was sensitive to the radial placement of the 12 large tungsten cylinders. The large volumes of the cylinders lent themselves to density variations. The proof mass sampled the field of the source mass over an extended volume. The mass of each component acted as a weighting-value for the acceleration contribution of that component. If the components were mislocated they sampled a slightly different field than was modeled.

This appendix contains the details of the metrology of the tungsten cylinders and the modeling of both the source and proof mass. First I discuss the source mass and then the proof mass.

## A.1 Metrology of the Source Mass

The most important contribution to the mass of the source object is from the 12 tungsten alloy cylinders that form the bulk of its volume. The cylinders were custom made for the experiment by Schwarzkopf Technologies Corporation, a well known producer of tungsten products. Because tungsten has an extremely high melting temperature most tungsten products are sintered rather than cast.

The sintering process glues small tungsten particles together with a binding agent; in our case the binding agent was a mixture of copper and nickel. A well-mixed powder of the tungsten and binding metals was first pressed into forms, then heated. The heat melted the binder, which seeped through the pores of the powder. This process reduces the volume of the mass by about 20%. The binding agent made up 4.5% of the total mass of the alloy. This particular alloy is called "Densimat 18K", a paramagnetic material with low susceptibility; it was tested for magnetic susceptibility, and has a volume susceptibility of 0.00066 ± 5% in MKS units[32, 53].

The tungsten was cast in three long rods that were each cut into smaller lengths to produce the cylinders. When the cylinders arrived in JILA they were machined to matching heights and diameters (to about 0.001 cm). At this point one end of the cylinders was marked as the “R” side, or reference end. This surface was cut at the factory, while the opposite side was cut at JILA. I arbitrarily decided that the “R” sides are the bottom ends of the cylinders, and use the two terms interchangeably.

We tested for density variations between and within the cylinders in three ways. First we weighed each cylinder and calculated its density from its dimensions. The densities of the billets were treated as a statistical ensemble and indicate a mean density of 17.724 gr/cc with a standard deviation of 0.008 gr/cc, representing an variation in density from one piece to another of only 0.04%. The peak to peak variation in density was 0.02 gr/cc, or 0.12% [54]. This measurement gave a good idea of the magnitude of density variations over the volume scale of a single cylinder ($\approx 2000\ \text{cm}^3$). We measured possible variations over smaller volumes using more sophisticated techniques.

To characterize angularly dependent inhomogeneities we measured the period of oscillation of the cylinders on an air bearing. The cylinders were placed on the air bearing so that they could rotate about their axes of cylindrical symmetry with low friction. The bearing was placed on a slight incline and the cylinders were kept from slipping off lengthwise with a pin placed close to the axis of rotation.

The frequency of oscillation is related to the torque of the offset center of mass:

$$dmg\theta = -I\theta'' \tag{A.1}$$

where $I$ is the moment of inertia of the cylinder, $d$ is the displacement of the center of mass from the geometric center, $m$ is the mass of the cylinder, and $\theta$ is the angle from equilibrium. Thus $d$ is given by:

$$d = \frac{I\omega^2}{mg} \tag{A.2}$$

with $\omega$ being the angular frequency of the oscillation. The direction of the offset $d$ was also measured, simply by letting the cylinder ring down to equilibrium. After each measurement the cylinder was swapped end-for-end and both measurements were repeated. The equilibrium position varied slightly depending on whether the bottom or top of the cylinder was facing the pin. When the cylinders were positioned on the support plates the direction of the density gradient was set to be tangential to the radius from the drop axis. This helped limit possible signal errors that arose from angularly dependent density variations.

To obtain some information about linear density variations along the length of the cylinders we compared the weight of each end of the cylinders. Figure 3.6 includes a schematic of the apparatus. Each cylinder was placed such that its weight was supported between a pivot point and a electronic balance. A spacer was used to put the geometric center of the approximately halfway midway the pivots. The balance was zeroed, and the cylinder was then swapped end for end while insuring that the geometric center was not moved. The change in the reading of the balance gave an indication of the linear density variation within each cylinder. The balance used was a Setra brand scale accurate to 1 gram (I checked its calibration through the local NIST chapter). This scale uses a stressed quartz element to determine the weight placed on its pan; there is very little "give" in the pan so it maintains its vertical position even while supporting different weights.

Each cylinder was numbered at the time it was machined. Table A.1 is a listing of the height, diameter, weight, density of each cylinder. Table A.2 lists the results of the air bearing and linear weight difference tests. It includes the period of oscillation on the air bearing for each orientation of the cylinders, and the linear weight difference. The difference (in arc) of the equilibrium position of the cylinders in their two orientations on the air bearing was typically 1 cm.

Only the large cylinders were tested in these ways. All the other components of the source mass were assumed to be uniform in density. Once the cylinders were characterized as carefully as possible they were arranged between the support plates so as to minimize possible linear and radial density variations. Figure A.1 shows how the cylinders were actually placed for the May experiment. The top layer of masses includes cylinders 4, 6, 8, 9, 10, and 11, for a total mass of 238110 grams. Cylinders 1, 2, 3, 5, 7, and 12 formed the lower layer, with a total weight

| Cylinder | Height, cm | Diameter, cm | Weight, g | Density, g/cm$^3$ |
|---|---|---|---|---|
| 1 | 10.3637 | 16.5862 | 39682 | 17.712 |
| 2 | 10.3637 | 16.5857 | 39709 | 17.734 |
| 3 | 10.3627 | 16.5837 | 39669 | 17.723 |
| 4 | 10.3632 | 16.5862 | 39664 | 17.714 |
| 5 | 10.3632 | 16.5862 | 39662 | 17.713 |
| 6 | 10.3637 | 16.5854 | 39700 | 17.731 |
| 7 | 10.3632 | 16.5862 | 39678 | 17.720 |
| 8 | 10.3632 | 16.5862 | 39679 | 17.721 |
| 9 | 10.3627 | 16.5862 | 39701 | 17.732 |
| 10 | 10.3627 | 16.5857 | 39662 | 17.715 |
| 11 | 10.3637 | 16.5867 | 39704 | 17.730 |
| 12 | 10.3632 | 16.5870 | 39704 | 17.730 |
| AVERAGE | 10.36324 | 16.58543 | 39684.5 | 17.7229 |

Table A.1: Dimensions, weight and density of the 12 Densimet 18K tungsten cylinders. All length measurements are in centimeters ± 0.0005 cm. The weight measurements are grams ± 1 gram. The density values are g/cm ± 0.001 g/cc.

| Cylinder | Period Top, s | Period Bottom, s | $\delta$T, s | Linear Difference, g |
|---|---|---|---|---:|
| 1 | 23.25 | 22.5 | 1.0 | -9 |
| 2 | 29.0 | 28.8 | 0.9 | -4 |
| 3 | 29.5 | 28.0 | 0.6 | 3 |
| 4 | 37.0 | 39.5 | 1.9 | 2 |
| 5 | 31.5 | 31.0 | 0.9 | -2 |
| 6 | 25.0 | 24.5 | 0.3 | 1 |
| 7 | 27.0 | 27.5 | 0.6 | -3 |
| 8 | 28.8 | 29.0 | 1.3 | -3 |
| 9 | 24.5 | 24.5 | 1.0 | 17 |
| 10 | 26.5 | 26.5 | 0.9 | -4 |
| 11 | 25.8 | 25.0 | 0.3 | -12 |
| 12 | 23.0 | 23.2 | 0.8 | 3 |
| AVERAGE | 27.6 | 27.5 | 0.9 | -1.8 |

Table A.2: The results of testing the angular and linear density variations of the 12 cylinders. The period is in seconds, ± 0.25 second. The quality of the equilibria positions is indicated by the difference in period between the two orientations, $\delta$T. The linear weight difference is in grams, ± 2 grams.

of 238104 grams. Thus the top and bottom layers only differ in weight by 6 grams.

In the top row cylinders 8, 9, 10 and 11 were placed "right-side up" (R-side down), while cylinders 4 and 6 were placed upside-down (R-side up). Thus there was a net difference in weight from the top of the cylinders to the bottom of -1 gram. In the bottom row, cylinders 1, 3, 5, and 12 were right side up and 2 and 7 were upside down. This resulted in a total gradient of +2 grams over the height of the bottom row. The net linear gradient of the whole mass assembly was thus $-1 + 2 + 6 = 7$ grams over the height of both layers.

All the components of the source mass were modeled as cylinders characterized by a vertical position with respect to the bottom of the lower support plate, a height, an inner and outer radius, an offset from the symmetry axis of the source mass, and a mass. Because many of the cylinders occur in symmetric polar arrays about the central symmetry axis, the model also includes an "array number" which is assigned the number of cylinders in the array. Thus a single entry in the model might represent more than one cylinder. The entry[1] : position $= 1$, height $= -1$, inner radius$= 0.2$, outer radius $= 0.5$, mass $= 1$, offset $= 10$ and number $= 6$ represents an array of hollow cylinders (with the appropriate inner and outer radii) placed 10 cm from the axis of source mass symmetry. Each is located such that the bottom of the cylinder is 1 cm above the bottom of the lower support plate, and there is a 60 $(\frac{360}{6})$ degree polar angle between each cylinder.

The emphasis in the model was on preserving the net mass of each element of the source mass, as well as its radial and vertical position. Some arrays of screws were modeled not as individual cylinders, but as a single ring of mass. This approximation is good for small objects. Because the field of the source mass is very close to cylindrically symmetric the only error in this method is an incorrect density as a function of radius — a tiny error.

---

[1] All positions are given in centimeters. The mass is given in grams.

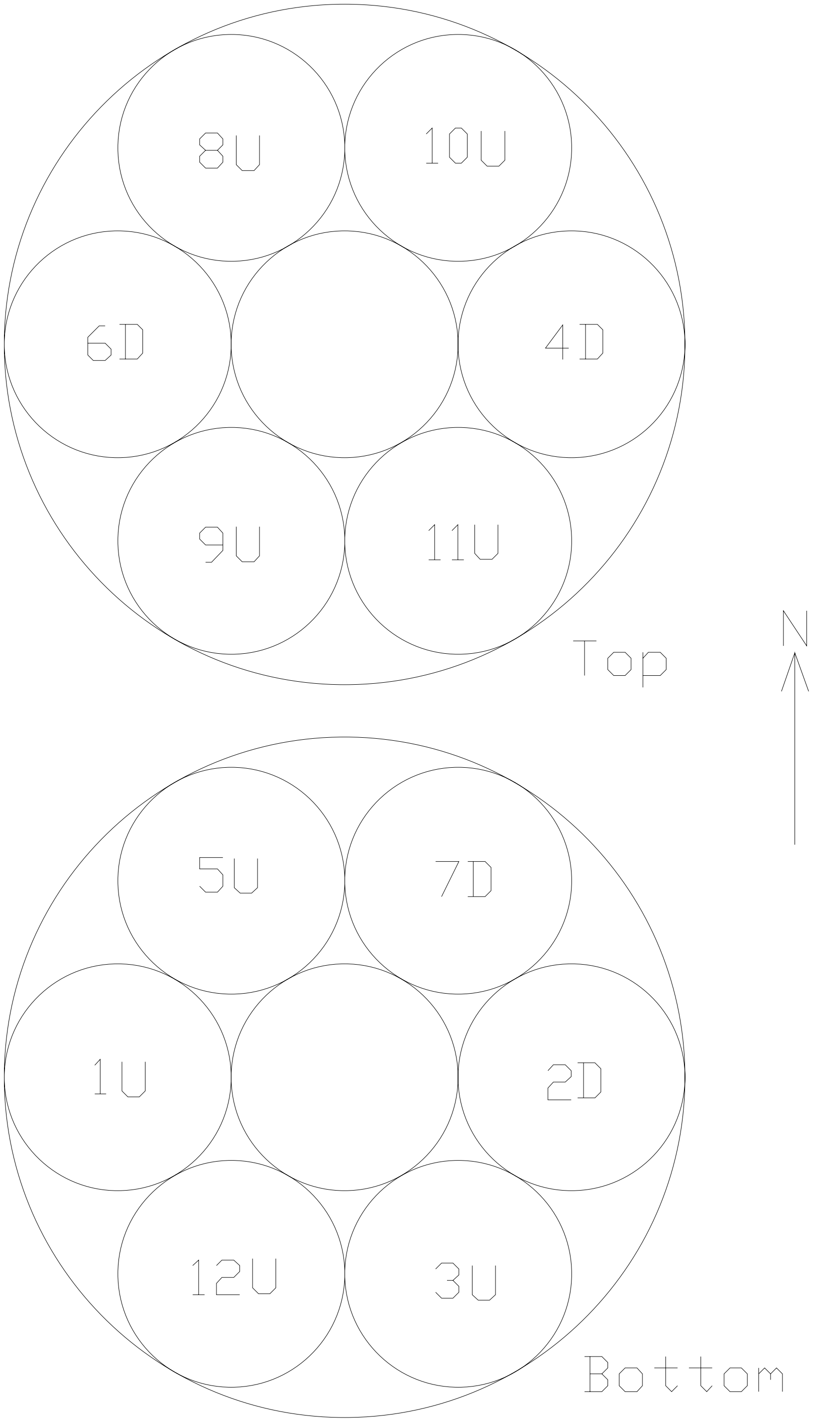

Figure A.1: Arrangement of the 12 tungsten cylinders within the source mass. "U" represents cylinders placed right side up, while "D" marks those that were placed up side down. The arrow points only approximately to the North.

The threads of bolts and the threaded portions of holes were not modeled precisely. In the source mass model I occasionally modeled a width, $x$, of threads on the inner or surface of a hole as an extra thickness of the surface of $\frac{x}{2}$. Alternatively I modeled the threads as a layer with one-half the density of the solid material. The mass of the whole object was constrained to be the measured mass, so this corresponds to a slight density and positioning error, also a tiny error.

Often the objects that make up the source mass were modeled as a series of cylinders. The “inner tungsten rods” are a good example. They were small (1” diameter) tungsten rods with holes tapped in both ends, placed in the gaps around the main cylinders of the source mass. Each rod was modeled as three cylinders: First a solid cylinder of the same outer radius, offset and height of the rods was modeled. This cylinder was assigned a mass value that was the sum of the actual mass of the rod and the additional mass removed from the bolt holes. Second a small solid cylinder located at the lower end of the rod, of dimensions matching the bolt holes and a negative mass to exactly cancel the “extra” mass modeled in the main rod. Third, another “hole” with negative mass was modeled at the top of the rod.

The complete source mass model used for the ’97 experiment is shown in three tables: Table A.3 includes the model of the lower support plate and nut flanges. Table A.4 describes the upper plate, with bushings. Table A.5 embraces the main tungsten cylinders, the tungsten rods, and the support rods.

The 1998 experiment incorporated several improvements. Thicker support plates were used to reduce flexing, and thus cocking of the support nuts. Additional support rods, made of aluminum, also reduced flexing. Table A.6 contains the ’98 model of the support plates, while Table A.7 contains the rest of the system.

| Description | Position | Height | $r_{inner}$ | $r_{outter}$ | Mass | Offset | # |
|---|---|---|---|---|---|---|---|
| Lower Plate | 0 | 1.283 | 10.658 | 25.96 | 6651.5 | 0 | 1 |
| lower ring | 1.283 | 0.993 | 24.892 | 25.963 | 467.3 | 0 | 1 |
| holes for tears | 0 | 1.283 | 0 | 0.337 | -1.26 | 11.366 | 6 |
| CB for tear bolts | 0 | 0.759 | .337 | 0.517 | -1.01 | 11.366 | 6 |
| machining holes | 0 | 1.283 | 0 | 0.700 | -5.34 | 15.24 | 4 |
| Counter Bore for outter W rods | 0 | 0.635 | 0 | 1.045 | -6.00 | 19.06 | 3 |
| Holes for O.W rods | 0.635 | 0.648 | 0 | 0.52 | -1.48 | 19.06 | 3 |
| C.B. for flanges | 0 | 0.635 | 0 | 3.203 | -56.28 | 20.32 | 3 |
| Holes for Bronze Nuts | 0.635 | 0.648 | 0 | 1.93 | -20.86 | 20.32 | 3 |
| Extra flange bolt holes | 0.635 | 0.648 | 1.905 | 2.15 | -2.855 | 20.32 | 3 |
| Necessary F.B. holes | 0.635 | 0.648 | 2.288 | 2.776 | -5.71 | 20.32 | 3 |
| Flanges, Whole | -.629 | 1.264 | 1.700 | 3.187 | 78.92 | 20.32 | 3 |
| Slots in Flanges | -.629 | 1.264 | 2.195 | 2.883 | -32.19 | 20.32 | 3 |
| Threaded portion of nuts | -.629 | 1.264 | .857 | 1.7 | 73.6 | 20.32 | 3 |
| Clean portion of nuts | 0.635 | 2.542 | .857 | 1.911 | 202.1 | 20.32 | 3 |
| Bolts,washers of flanges | -1.30 | 2.54 | 2.19 | 2.88 | 28.4 | 20.32 | 3 |

Table A.3: Model of the lower support plate of the source mass, '97 experiment. The masses are corrected bor buoyancy effects. All dimensions (position, height, $r_{inner}$, $r_{outter}$, offset) are in centimeters. The masses are in grams.

| Description | Position | Height | r$_{inner}$ | r$_{outter}$ | Mass | Offset | # |
|---|---|---|---|---|---|---|---|
| Holes for support rods | 22.01 | 1.01 | 0 | .337 | -1.26 | 11.366 | 6 |
| Top Plate | 22.01 | 1.01 | 8.3 | 25.96 | 5344 | 0 | 1 |
| Inner W holes | 22.01 | .375 | 0 | .55 | -.98 | 9.55 | 6 |
| Inner W clearance | 22.38 | .635 | 0 | 1.04 | -6 | 9.55 | 6 |
| bolt heads | 22.38 | .384 | 0 | .55 | 2.54 | 9.475 | 6 |
| Top Inner W Bolts | 20.9 | 1.68 | 9.08 | 9.88 | 4.9 | 0 | 1 |
| Outter W clearance | 22.38 | .635 | 0 | 1.04 | -6 | 19.06 | 3 |
| bolt heads | 22.38 | .384 | 0 | .55 | 2.54 | 19.252 | 3 |
| screws part | 21.115 | 1.27 | 0 | .3 | 3.46 | 19.252 | 3 |
| Holes for bushings | 22.01 | .375 | 0 | 1.27 | -5.22 | 20.32 | 3 |
| counterbore for bushings | 22.38 | .635 | 0 | 2.54 | -35.4 | 20.32 | 3 |
| holes for bolts for bushings | 22.01 | .375 | 1.64 | 1.67 | -1.2 | 20.32 | 3 |
| holes for machining | 22.01 | 1.02 | 0 | .69 | -4.2 | 15.25 | 4 |
| lip of plate | 21.74 | .27 | 24.89 | 25.96 | 126.9 | 0 | 1 |
| Long part of bushing | 17.3 | 5.08 | .960 | 1.24 | 82.09 | 20.32 | 3 |
| Flange of bushing | 22.38 | .635 | .960 | 2.54 | 86.6 | 20.32 | 3 |
| holes for screws, IN bushings | 22.38 | .635 | 1.57 | 2.21 | -.53 | 20.32 | 3 |
| bolt heads for bushings | 23.02 | .62 | 1.34 | 2.3 | 8.8 | 20.32 | 3 |
| screws body for bushing | 22.09 | .93 | 1.52 | 2.1 | 8.84 | 20.32 | 3 |

Table A.4: Model of the Upper Plate of the source mass, '97 experiment. The masses are corrected bor buoyancy effects. All dimensions (position, height, r$_{inner}$, r$_{outter}$, offset) are in centimeters. The masses are in grams.

| Description | Position | Height | $r_{inner}$ | $r_{outter}$ | Mass | Offset | # |
|---|---|---|---|---|---|---|---|
| Bottom Row W cyls | 1.283 | 10.3632 | 0 | 8.2931 | 39684.0 | 16.586 | 6 |
| Top Row W cyls | 11.6462 | 10.3632 | 0 | 8.2931 | 39685.0 | 16.586 | 6 |
| Inner W rods * | 1.556 | 20.45 | 0 | 1.27 | 1920.91 | 9.475 | 6 |
| O W rods * | 1.283 | 20.45 | 0 | 1.27 | 1920.91 | 19.252 | 3 |
| L holes I rod | 1.556 | 1.27 | 0 | .32 | -7.2 | 9.475 | 6 |
| L holes O rod | 1.283 | 1.27 | 0 | .32 | -7.2 | 19.252 | 3 |
| H holes I rod | 20.73 | 1.27 | 0 | .32 | -7.2 | 9.475 | 6 |
| H holes O rod | 20.46 | 1.27 | 0 | .32 | -7.2 | 19.252 | 3 |
| Washers of O W rods | 21.73 | .27 | .32 | 1.27 | 3.52 | 19.252 | 3 |
| SR * | 1.556 | 20.45 | 0 | .476 | 116.05 | 11.366 | 6 |
| L holes of SR | 1.556 | 1.52 | 0 | .285 | -3.2 | 11.366 | 6 |
| H holes of SR | 20.73 | 1.27 | 0 | .285 | -3.2 | 11.366 | 6 |
| Teardrops(as ring) | 1.283 | .273 | 10.658 | 13.477 | 24.8 | 0 | 1 |
| L. inner W rod bolts | 1.283 | 1.78 | 9.16 | 9.79 | 14 | 0 | 1 |
| L Bolts for SR | 0.07 | 2.54 | 11.05 | 11.68 | 37.5 | 0 | 1 |
| H Bolts for SR | 20.88 | 2.54 | 11.05 | 11.68 | 37.5 | 0 | 1 |

Table A.5: Model of the Main Mass and Sandwich stuctures of the source mass, '97 experiment. * — Mass includes extra mass correction for holes. L(H) — at the lower (upper) portion of the source mass. I(O) — at the inner (outter) rod position. SR — support rods. The masses are corrected bor buoyancy effects. All dimensions (position, height, $r_{inner}$, $r_{outter}$, offset) are in centimeters. The masses are in grams.

| Description | Position | Height | $r_{inner}$ | $r_{outter}$ | Mass | Offset | # |
|---|---|---|---|---|---|---|---|
| LP base* | 0 | 2.2454 | 10.541 | 24.8857 | 10168.19 | 0 | 1 |
| LP ring | 0 | 3.7770 | 24.8857 | 26.6675 | 3092.13 | 0 | 1 |
| Inner SR holes | 0 | 2.2454 | 0 | .3454 | -2.388 | 11.3665 | 6 |
| Inner CB | 0 | .6680 | .3454 | .5359 | -.99965 | 11.3665 | 6 |
| 2nd SR holes | 0 | 2.2454 | 0 | .3454 | -2.388 | 17.3812 | 3 |
| 2nd CB | 0 | .6680 | .3454 | .5359 | -.99965 | 17.3812 | 3 |
| 3rd SR holes | 0 | 2.2454 | 0 | .3454 | -2.388 | 19.252 | 3 |
| 3rd CB | 0 | .6680 | .3454 | .5359 | -.99965 | 19.252 | 3 |
| 4th SR holes | 0 | 2.2454 | 0 | .3454 | -2.388 | 22.86 | 3 |
| 4th CB | 0 | .6680 | .3454 | .5359 | -.99965 | 22.86 | 3 |
| Nut hole | 0 | 2.2454 | 0 | 1.9177 | -73.596 | 20.32 | 3 |
| Nut CB | 0 | 1.2725 | 1.9177 | 3.1979 | -74.271 | 20.32 | 3 |
| threaded holes | 1.2725 | .970 | 2.3813 | 2.699 | -7.501 | 20.32 | 3 |
| Nut flanges* | 0 | 1.264 | 1.700 | 3.187 | 78.92 | 20.32 | 3 |
| Slots in Flanges | 0 | 1.264 | 2.195 | 2.883 | -32.19 | 20.32 | 3 |
| Threaded part nuts | 0 | 1.264 | .857 | 1.7 | 74.6 | 20.32 | 3 |
| Clean part nuts | 1.264 | 2.542 | .857 | 1.911 | 202.1 | 20.32 | 3 |
| Flange bolts | -.671 | 2.54 | 2.19 | 2.88 | 28.7 | 20.32 | 3 |
| TP top | 22.972 | 2.21 | 10.541 | 24.884 | 10001.45 | 0 | 1 |
| TP ring | 21.420 | 3.762 | 24.884 | 26.671 | 3087.33 | 0 | 1 |
| TP scratch | 22.972 | .1956 | 13.202 | 14.1745 | -46.39 | 0 | 1 |
| TP in holes | 22.972 | 2.21 | 0 | .3454 | -2.349 | 11.3665 | 6 |
| 2ndTP in holes | 22.972 | 2.21 | 0 | .3454 | -2.349 | 17.3812 | 3 |
| 3rdTP in holes | 22.972 | 2.21 | 0 | .3454 | -2.349 | 19.252 | 3 |
| 4th inner holes | 22.972 | 2.21 | 0 | .3454 | -2.349 | 22.86 | 3 |
| Bushing holes | 22.972 | 2.21 | 0 | 1.270 | -31.75 | 20.32 | 3 |
| TP bushing bolts | 23.1 | 2 | 1.7 | 2.1 | 17.7 | 20.32 | 3 |
| 4 threaded holes | 22.972 | 2.21 | 1.588 | 2.222 | -6.5073 | 20.32 | 3 |

Table A.6: Model of the support plates, '98 experiment. All length measurments are in centimeters, and all mass values are in grams. LP stands for "lower plate", CB stands for "counterbore", SR stands for "support rods", and TP stands for "top plate". "Inner", "2nd", "3rd" and "4th" refer to rings of bolt holes, counted from the center of the plates. The masses are corrected bor buoyancy effects. Objects marked with "*" include extra mass to make up for holes.

| Description | Position | Height | $r_{inner}$ | $r_{outter}$ | Mass | Offset | # |
|---|---|---|---|---|---|---|---|
| Upper W cyls | 2.2454 | 10.3632 | 0 | 8.2931 | 39678.6 | 16.5887 | 6 |
| Lower W cyls | 12.6086 | 10.3632 | 0 | 8.2931 | 39679.6 | 16.5887 | 6 |
| IW* | 2.5184 | 20.45 | 0 | 1.27 | 1920.74 | 9.475 | 6 |
| OW* | 2.2454 | 20.45 | 0 | 1.27 | 1920.74 | 19.252 | 3 |
| washers for OW | 22.695 | .273 | .3175 | 1.25 | 3.5 | 19.252 | 3 |
| l-corr IW | 2.5184 | 1.27 | 0 | .32 | -7.2 | 9.475 | 6 |
| l-corr OW | 2.2454 | 1.27 | 0 | .32 | -7.2 | 19.252 | 3 |
| h-corr IW | 21.6984 | 1.27 | 0 | .32 | -7.2 | 9.475 | 6 |
| h-corr OW | 21.4254 | 1.27 | 0 | .32 | -7.2 | 19.252 | 3 |
| inner SRs* | 2.5184 | 20.44 | 0 | .476 | 40.07 | 11.3665 | 6 |
| l-corr | 2.5184 | 2 | 0 | .32 | -1.395 | 11.3665 | 6 |
| h-corr | 20.958 | 2 | 0 | .32 | -1.395 | 11.3665 | 6 |
| long middle SR* | 2.2454 | 20.71 | 0 | .476 | 40.61 | 17.3812 | 3 |
| l-corr middle SR | 2.2454 | 2 | 0 | .32 | -1.395 | 17.3812 | 3 |
| h-corr for MSR | 21.2 | 2 | 0 | .32 | -1.395 | 17.3812 | 3 |
| H: i-l SR bolts | 0 | .635 | .254 | .4763 | 1.925 | 11.3665 | 6 |
| S: i-l SR bolts | .635 | 3.175 | 0 | .3175 | 3.00 | 11.3665 | 6 |
| H: 2nd-l SR bolts | 0 | .635 | .254 | .4763 | 1.925 | 17.3812 | 3 |
| S: 2nd-l SR bolts | .635 | 3.175 | 0 | .3175 | 3.00 | 17.3812 | 3 |
| H: 4th-l SR bolts | 0 | .635 | .254 | .4763 | 1.925 | 22.860 | 3 |
| S: i-l SR bolts | .635 | 3.175 | 0 | .3175 | 3.00 | 22.860 | 3 |
| H: o-l TR bolts | 0 | .635 | .254 | .4763 | 1.925 | 19.252 | 3 |
| S: o-l TR bolts | .635 | 2.0574 | 0 | .3175 | 2.308 | 19.252 | 3 |
| H: i-u SR bolt | 25.5120 | .635 | .254 | .4763 | 1.925 | 11.3665 | 6 |
| S: i-u SR bolts | 21.702 | 3.81 | 0 | .3175 | 4.12 | 11.3665 | 6 |
| H: 2nd-u SR bolt | 25.1820 | .635 | .254 | .4763 | 1.925 | 17.3812 | 3 |
| S: 2nd-u SR bolts | 21.372 | 3.81 | 0 | .3175 | 4.12 | 17.3812 | 3 |
| H: o-u SR bolt | 25.1820 | .635 | .254 | .4763 | 1.925 | 22.860 | 3 |
| S: o-u SR bolts | 21.372 | 3.81 | 0 | .3175 | 4.12 | 22.860 | 3 |
| H: o-u TR bolt | 25.1820 | .635 | .254 | .4763 | 1.925 | 19.252 | 3 |
| S: o-u TR bolts | 22.007 | 3.175 | 0 | .3175 | 3.0 | 19.252 | 3 |
| H: i-u TR bolt | 25.5120 | .635 | .254 | .4763 | 1.925 | 9.475 | 6 |
| S: i-u TR bolts | 21.797 | 3.175 | 0 | .3175 | 3.00 | 9.475 | 6 |
| Teardrops | 2.2454 | .273 | 10.658 | 13.477 | 24.8 | 0 | 1 |
| l-bolts IW | 2.2454 | 1.78 | 9.16 | 9.79 | 14.1 | 0 | 1 |
| IW locator body | 22.972 | 2.548 | .3454 | .890 | 14.0358 | 9.475 | 6 |
| IW “”"” flange | 25.182 | .330 | .3454 | .890 | 1.82 | 11.3665 | 6 |

Table A.7: ’98 model of tungsten elements, support rods, and bolts. All length measurments are in centimeters, and all mass values are in grams. “Inner”, “2nd”, “3rd” and “4th” refer to rings of bolt holes, counted from the center of the plates. IW stands for “inner tungsten rod”, OW stands for “outter tungsten rod”, SR stands for the aluminium support rods, “MSR” refers to SRs in the middle ringe. S: stands for “screw” and H: for “head” The masses are corrected bor buoyancy effects. Objects marked with “*” include extra mass to make up for holes.

## A.2 Modeling the Test Mass

The test mass was an extremely important part of the absolute gravimeter. It was designed to be non-magnetic, conducting, and rugged (see Sec. 3.1.4.1). It is a complex object that was difficult to model, especially at the level of accuracy required by the experiment (as discussed in Appendix Sec. B.3.2).

The proof mass model consists of a collection of cylinders, just as that of the source mass. I was more careful in the modeling of threads, however. They were consistently modeled as regions of one half the density of the rest of the material. The proof mass is "blessed" with more components that resist casting as cylinders than the source mass — the corner cube is essentially a pyramid, and the optical lens is a sphere. The corner cube was modeled as ten stacked cylindrical slabs, while the sphere was modeled as a tiny cylinder closely mimicking a point mass. Because in a source free region a sphere acts as if all it's mass were concentrated at the center of the sphere, this is a reasonable approximation. It is not quite perfect because the interpolation grid of the source mass field is imperfect, and the tiny cylinder isn't truly a point mass.

The entire proof mass model is contained in the following tables. Figure A.2 is a photo of the proof mass. Figure A.3 is a drawing of the proof mass model elements. Table A.8 models the top hat of the proof mass. Table A.9 includes the tungsten balls, the top hat cap and optical sphere. Table A.10 encompasses the corner cube holder and the counter weight. Table A.11 embraces the test mass body, nut and legs. Table A.12 only holds the corner cube model.

| Description | Position | Height | $r_{inner}$ | $r_{outter}$ | Mass | Offset | # |
|---|---|---|---|---|---|---|---|
| lowest part | 2.607 | .2 | 0 | 1.025 | 1.7680 | 0 | 1 |
| main base top hat | 2.807 | .4 | 0 | 1.60 | 8.6179 | 0 | 1 |
| thin part central hole | 2.607 | .6 | 0 | .075 | -.0289 | 0 | 1 |
| thick part central hole | 3.207 | .131 | 0 | .15 | -.0244 | 0 | 1 |
| air hole for W ball | 3.169 | .169 | 0 | .1 | -.0146 | .4 | 3 |
| hole for W balls | 2.607 | .562 | 0 | .198 | -.1850 | .4 | 3 |
| holes in TM body legs | 2.807 | .4 | 0 | .15 | -.0759 | 1.27 | 3 |
| top of top hat base | 3.207 | .131 | 0 | .975 | 1.0481 | 0 | 1 |
| bottom tophat can | 3.3376 | .449 | .812 | .975 | 1.1008 | 0 | 1 |
| lowest part OVAL hole | 3.787 | .118 | .812 | .975 | 0.1754 | 0 | 1 |
| 2nd lowest | 3.905 | .1 | .812 | .975 | 0.1318 | 0 | 1 |
| center of oval hole | 4.005 | .2 | .812 | .975 | 0.2385 | 0 | 1 |
| 1st above center | 4.205 | .1 | .812 | .975 | 0.1318 | 0 | 1 |
| top of oval hold | 4.305 | .118 | .812 | .975 | 0.1754 | 0 | 1 |
| Can above oval | 4.423 | .134 | .812 | .975 | 0.3284 | 0 | 1 |
| solid part of can top | 4.556 | .65 | .860 | .975 | 1.1566 | 0 | 1 |
| threaded part can top | 4.707 | .5 | .815 | .86 | 0.1397 | 0 | 1 |

Table A.8: Model of the Top Hat cap of the proof mass. All dimensions (position, height, $r_{inner}$, $r_{outter}$, offset) are in centimeters. The masses are in grams.

| Description | Position | Height | $r_{inner}$ | $r_{outter}$ | Mass | Offset | # |
|---|---|---|---|---|---|---|---|
| tungsten ball stock | 2.569 | .62 | 0 | .1985 | 1.447 | .4 | 3 |
| 1st part ball end W ball | 2.469 | .08 | 0 | .198 | 0.148 | .4 | 3 |
| top W ball | 2.369 | .05 | 0 | .11 | 0.039 | .4 | 3 |
| Glass sphere | 4.104 | .001 | 0 | .01 | 4.65 | 0 | 1 |
| main part top hat cap | 4.785 | .35 | .45 | .8244 | 1.314 | 0 | 1 |
| threads | 4.785 | .35 | .8244 | .8475 | 0.055 | 0 | 1 |
| holes | 4.785 | .4 | 0 | .1 | -.032 | .6 | 4 |
| step | 4.896 | .15 | .334 | .45 | 0.107 | 0 | 1 |
| top layer | 5.135 | .05 | .25 | .8375 | 0.251 | 0 | 1 |
| Mirror | 4.985 | .1 | 0 | .3175 | 0.09 | 0 | 1 |
| spring washer | 4.972 | .13 | .19 | .318 | 0.02 | 0 | 1 |
| outter ring retainer | 4.780 | .192 | .375 | .425 | 0.04 | 0 | 1 |
| inner ring | 4.780 | .1517 | .159 | .375 | 0.08 | 0 | 1 |

Table A.9: Model of proof mass: Tungsten balls, glass sphere, top hat cap. All dimensions (position, height, $r_{inner}$, $r_{outter}$, offset) are in centimeters. The masses are in grams.

| Description | Position | Height | r$_{inner}$ | r$_{outter}$ | Mass | Offset | # |
|---|---|---|---|---|---|---|---|
| Base plate | -4.1746 | .1 | 0 | 1.4 | 1.592 | 0 | 1 |
| main sides | -4.0746 | 1.95 | 1.125 | 1.474 | 14.375 | 0 | 1 |
| threads | -3.8746 | 1.75 | 1.474 | 1.4975 | 0.497 | 0 | 1 |
| Part over sides | -2.1246 | .15 | 1.125 | 1.45 | 1.020 | 0 | 1 |
| Stop | -1.9746 | .2 | 1.125 | 1.6 | 2.103 | 0 | 1 |
| bit over stop | -1.7746 | .1 | 1.125 | 1.47 | 0.728 | 0 | 1 |
| 2nd bit over stop | -1.6746 | .4 | 1.125 | 1.43 | 2.533 | 0 | 1 |
| CC holder | -1.2746 | .5 | 1.28 | 1.43 | 1.652 | 0 | 1 |
| laser holes | -4.1746 | .1 | 0 | .4525 | -.166 | .8125 | 2 |
| CC clearance slots | -1.7996 | .425 | 1.28 | 1.32 | -.021 | 0 | 1 |
| CC holder holesr | -1.05 | .1 | 0 | .1 | -.027 | 1.36 | 6 |
| glue | -1.7996 | .4 | 1.26 | 1.32 | 0.352 | 0 | 1 |
| laser slice | -4.0746 | 2.8 | 1.125 | 1.2 | -.665 | 0 | 1 |
| main ring | -3.303 | .6 | 1.525 | 1.95 | 7.1251 | 0 | 1 |
| threads | -3.303 | .6 | 1.4625 | 1.525 | 0.1034 | 0 | 1 |
| top holes | -2.963 | .261 | 0 | .09 | -.0177 | 1.74 | 2 |
| bottom holes | -3.303 | .26 | 0 | .11 | -.0265 | 1.74 | 2 |
| bolt long part | -3.303 | .6 | 0 | .09 | 0.080 | 1.74 | 2 |
| bolt head | -3.503 | .2 | .075 | .19 | 0.180 | 1.74 | 2 |

Table A.10: Model of proof mass: Corner cube holder and counter weight. All dimensions (position, height, r$_{inner}$, r$_{outter}$, offset) are in centimeters. The masses are in grams.

| Description | Position | Height | $r_{\mathrm{inner}}$ | $r_{\mathrm{outter}}$ | Mass | Offset | # |
|---|---|---|---|---|---|---|---|
| threads TM body | -1.776 | .5 | 1.675 | 1.6975 | 0.1596 | 0 | 1 |
| solid bottom | -1.776 | .5 | 1.47 | 1.675 | 2.692 | 0 | 1 |
| thread relief | -1.276 | .1 | 1.47 | 1.6 | 0.336 | 0 | 1 |
| body can | -1.176 | 2.03 | 1.47 | 1.6975 | 12.304 | 0 | 1 |
| holes TM body | -1.126 | .3 | 0 | .19 | -.046 | 1.685 | 6 |
| top of TM body can | .854 | .25 | .3 | 1.697 | 5.867 | 0 | 1 |
| holes(V) | .854 | .25 | 0 | .15 | -.0477 | 1.27 | 3 |
| V portion of holes | 1.04 | .01 | .25 | .257 | -.0837 | 1.27 | 3 |
| base of legs | 1.105 | .86 | .125 | .330 | 0.674 | 1.27 | 3 |
| solid part of leg | 1.965 | .84 | .15 | .33 | 0.610 | 1.27 | 3 |
| threads | 1.965 | .83 | .125 | .15 | 0.024 | 1.27 | 3 |
| nibs | 2.555 | .25 | 0 | .04 | -.008 | .982 | 3 |
| solid part | -1.776 | .5 | 1.725 | 1.9 | 2.671 | 0 | 1 |
| thread | -1.776 | .5 | 1.662 | 1.677 | 0.035 | 0 | 1 |
| bottom ring | -2.118 | .15 | 1.53 | 1.9 | 1.604 | 0 | 1 |
| thread relief | -1.968 | .2 | 1.68 | 1.9 | 1.170 | 0 | 1 |
| holes | -1.868 | .001 | 0 | .001 | -.015 | 1.5625 | 4 |
| top of bolt | 3.207 | .3 | 0 | .275 | 0.599 | 1.27 | 3 |
| solid of bolt | 2.407 | .8 | 0 | .1 | 0.211 | 1.27 | 3 |
| thread | 2.407 | .8 | .1 | .15 | 0.132 | 1.27 | 3 |
| allen key hole | 3.307 | .2 | 0 | .125 | -.082 | 1.27 | 3 |

Table A.11: Model of proof mass: Test mass body, testmass nut and legs. All dimensions (position, height, $r_{inner}$, $r_{outter}$, offset) are in centimeters. The masses are in grams.

| Description | Position | Height | $r_{inner}$ | $r_{outter}$ | Mass | Offset | # |
|---|---|---|---|---|---|---|---|
| Bottom | -1.2719 | .127 | 0 | 1.265 | 1.72092 | 0 | 1 |
|  | -1.1449 | 0.09449 | 0 | 1.8898 | 1.52197 | 0 | 1 |
|  | -1.05041 | 0.09449 | 0 | 1.79531 | 1.37513 | 0 | 1 |
|  | -0.95592 | 0.09449 | 0 | 1.70082 | 1.16886 | 0 | 1 |
|  | -0.86143 | 0.09449 | 0 | 1.60633 | 1.00384 | 0 | 1 |
|  | -0.76694 | 0.09449 | 0 | 1.51184 | .880089 | 0 | 1 |
|  | -0.67245 | 0.09449 | 0 | 1.41735 | .770077 | 0 | 1 |
|  | -0.57796 | 0.09449 | 0 | 1.32286 | .664191 | 0 | 1 |
|  | -0.48347 | 0.09449 | 0 | 1.22837 | .569306 | 0 | 1 |
| Middle | -0.38898 | 0.09449 | 0 | 1.13388 | .481298 | 0 | 1 |
|  | -0.29449 | 0.09449 | 0 | 1.03939 | .401540 | 0 | 1 |
|  | -0.2 | 0.09449 | 0 | 0.9449 | .328657 | 0 | 1 |
|  | -0.10551 | 0.09449 | 0 | 0.85041 | .262651 | 0 | 1 |
|  | -0.01102 | 0.09449 | 0 | 0.75592 | .204895 | 0 | 1 |
|  | 0.08347 | 0.09449 | 0 | 0.66143 | .154014 | 0 | 1 |
|  | 0.17796 | 0.09449 | 0 | 0.56694 | .110010 | 0 | 1 |
|  | 0.27245 | 0.09449 | 0 | 0.47245 | .072881 | 0 | 1 |
|  | 0.36694 | 0.09449 | 0 | 0.37796 | .039790 | 0 | 1 |
|  | 0.46143 | 0.09449 | 0 | 0.28347 | .019895 | 0 | 1 |
| Top | 0.55592 | 0.09449 | 0 | 0.18898 | .009947 | 0 | 1 |

Table A.12: Model of proof mass: Corner Cube. All dimensions (position, height, $r_{inner}$, $r_{outter}$, offset) are in centimeters. The masses are in grams.

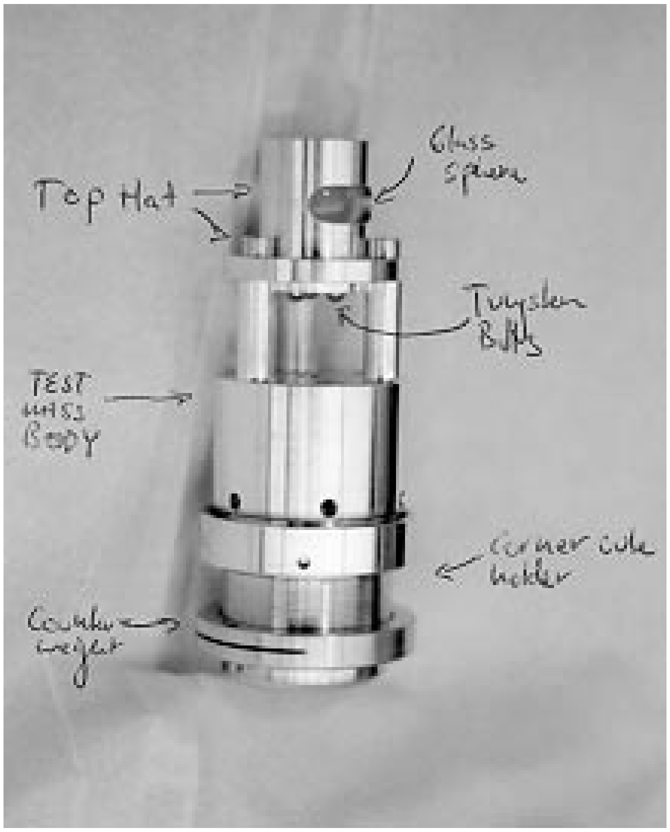

Figure A.2: A photograph of the proof mass. The proof mass is approximately 10 cm long. The "top hat" is upper portion of the mass, containing the glass sphere and the tungsten balls. The "test mass body" forms the center portion of the mass, including the three legs. The "corner cube holder" is the bottom portion of the mass, and has the counterweight treaded on its nether region.

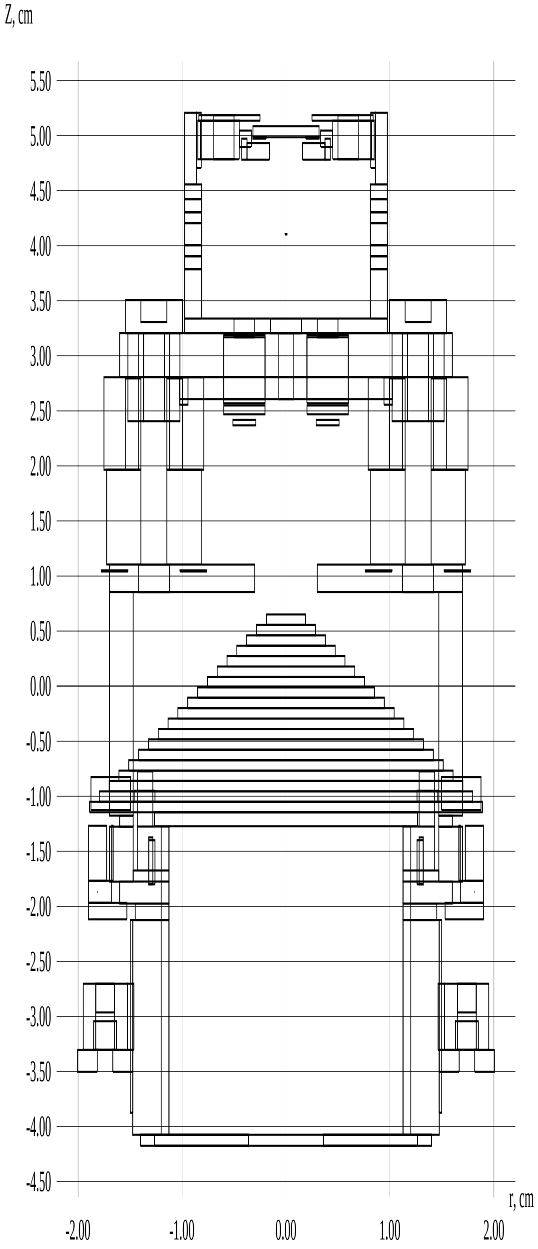

Figure A.3: A drawing of the proof mass model. The vertical axis is vertical extent of the proof mass, in centimeters. The horizontal axis represents its radial extents, in centimeters.

# APPENDIX B

# ERROR CALCULATIONS

This appendix contains the details of the error analysis that was introduced in Section 5.1.

## B.1 Positioning Errors

### B.1.1 Source Mass Positioning Errors

The source mass is located vertically about the gravimeter with a stepper-motor/shaft-encoder/screw-drive system. The lower mass position was measured to ± 0.01 cm with relation to the top of the (3/8" thick) flange of the custom dropping chamber. The top position was referenced to the lower with an uncertainty of ± 0.01 cm due to lead errors in the screws. Thermal expansion introduced uncertainty of ± 0.006 cm. Wear in the support nuts introduced an additional error of 0.01 cm. The root mean square uncertainty in the vertical position of the source mass (with respect to the dropping chamber flange) was ± 0.025 cm for the upper mass position, by direct measurement.

The distortion of the support plate in the 1997 experiment introduced a vertical displacement of approximately 0.01 cm. This was accounted for in our models, but still produced an uncertainty of 0.01 cm. The distortion of the plate raised some concern that the tungsten cylinders were being angled outwards. The distortion changes the radial position of the cylinders by less than 0.003 cm from

| Description | Magnitude | Signal, $\mu$Gal | Error, ppm |
|---|---|---|---|
| Shaft Encoder positioning[2] | 0.04 cm | 0.004 | 50 ppm |
| Horizontal velocity[1] | +0.004 -0 cm | 8e-6 | 8 ppb |
| Can setup[1] | +0.15 -0 cm | 0.003 | 33 ppm |
| Rotation errors | 0.0004 radian | 1e-6 | 1 ppb |
| Wear in tungsten vees, balls[2] | ± 0.02cm | 0.001 | 12 ppm |
| referencing to optical center within proof mass[2] | ± 0.005 cm | 0.0001 | — |
| referencing to gravimeter flange[2] | ± 0.01cm | 0.0002 | 5 ppm |

Table B.1: Uncertainties in proof mass position and orientation. [1]: A radial measurement. The net radial position uncertainty is 0.18 cm (0.007 $\mu$Gal = 85 ppm) in the 1997 experiment, and 0.15 cm (0.005 $\mu$Gal = 60 ppm) in the 1998 experiment. [2]: This error is not included in the total, because it is absorbed into the statistical uncertainty of the vertical position, from the direct extraction of the start of drop position from the data.

top to bottom. In the 1998 experiment the support plates used were approximately three times thicker than those of the 1997 run. Because the stiffness increases with the cube of the thickness, these errors were negligible in the 1998 experiment.

### B.1.2 Proof Mass Positioning errors

The signal magnitudes of test mass mis-positioning errors were calculated with a simplified test-mass model. The falling mass was modeled as a 8 cm long cylinder of inner diameter 1 cm and wall thickness of 1 mm for the calculations of errors. The net acceleration of this simplified model agrees with with the full model acceleration to 5%. Table B.1 lists the errors associated with proof mass positioning mechanisms.

### B.1.3 Extracted Positions

It is possible to extract the average value for the start-of-drop position from data directly (Sec. 4.3), with statistical uncertainty of 0.05 cm. In the 1997 experiment this method gave a result in agreement with the "direct" measurement.

In the 1998 experiment, however, the two determinations differed by 0.15 cm. The directly extracted value was used for both data runs, with the statistical uncertainty adopted as the error in this parameter. This method incorporates vertical positioning errors of both the source and test masses.

It is possible to extract the average value for the start-of-drop position from data directly (Sec. 4.3), with statistical uncertainty of 0.05 cm. In the 1997 experiment this method gave a result in agreement with the "direct" measurement. In the 1998 experiment, however, the two determinations differed by 0.2 cm. The directly extracted value was used for both data runs, with the statistical uncertainty adopted as the error in this parameter. This method incorporates vertical positioning errors of both the source and test masses.

## B.2 Spurious Signals

### B.2.1 Differential Magnetic Forces.

The manner that magnetic forces affect the results of the experiment are discussed in Sections 5.2.7 and 5.2.8, but here we discuss the calculation of the magnitudes of these effects. The information required to do this includes estimates of the magnetic field ( to calculate the direct attraction of the source mass to the proof mass) and field gradient (to determine the eddy current damping forces acting on the proof mass) carried by the changing position of our source mass.

Imagine the source mass as a thick-walled rod oriented vertically within a volume of uniform external vertical magnetic field. The field will induce the magnetic surface pole density, or effective charge, of

$$\chi \mathbf{B} \cdot \hat{n} \tag{B.1}$$

on the flat faces of the cylinder. $\mathbf{B}$ is the magnetic field, $\chi$ is the susceptibility of the material, and $\hat{n}$ is the unit vector normal to the surface. We integrate this density over the surfaces of the cylinder to find the magnetic scalar potential due to the presence of the source mass:

$$\varphi_i^*(\hat{r}) = \frac{1}{4\pi} \int_{S_o} \frac{\chi \mathbf{B} \cdot \hat{n}\ da'}{|\hat{r} - \hat{r}'|}$$

where $S_o$ is the area of the two faces of the cylinder, $\hat{r}$ is the position of evaluation, and $\varphi_i^*$ is the induced magnetic scaler potential. For the magnetic field on the axis of symmetry, we evaluate the gradient of the scaler potential:

$$\mathbf{B}(\hat{r}) = -\mu_o \nabla \varphi^*(\hat{r})$$

where $\mu_o$ is the permittivity of free space. The vertical component of the field and its gradient are plotted in Figure B.1.

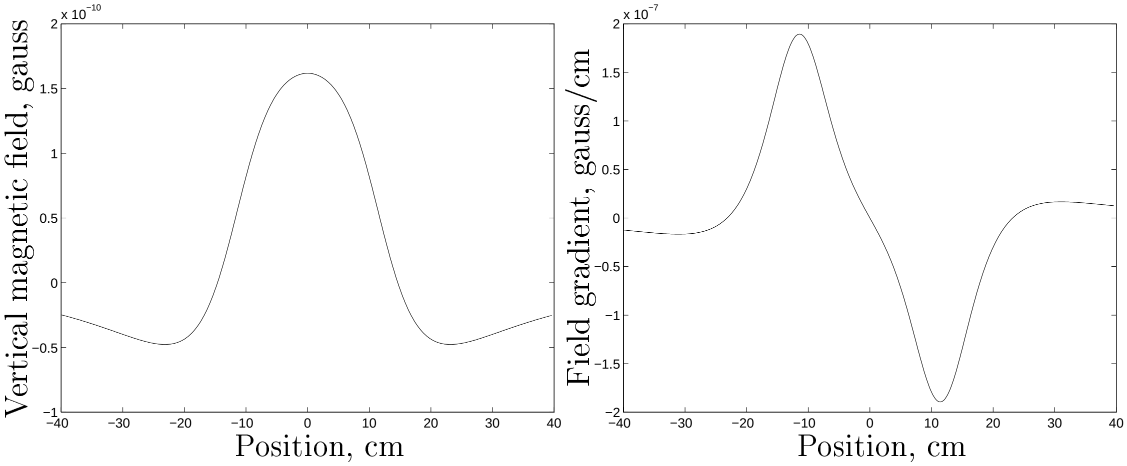

Figure B.1: The vertical magnetic field and field gradient induced by the susceptibility of a simple source mass model in a uniform vertical magnetic field of 0.5 gauss.

A bound of $5 \times 10^{-10}$ gauss and $5 \times 10^{-7}$ gauss/cm for the field and field gradient is reasonable. Modeling the proof mass as an aluminum cylinder [38] we can calculate the expected worst case eddy damping effect. From Eqn 5.5:

$$F = \frac{vA^2(\frac{dB}{dz})^2}{R}$$

defines the force, $F$, on a cylinder with surface area A perpendicular to a vertical magnetic gradient $\frac{dB}{dz}$. $R$ is the cylinder's resistance in a loop perpendicular to the gradient, and $v$ is its velocity. Using the values in Table B.2 we find that eddy currents could only cause a differential acceleration of $3X10^{-9}\mu$Gal. A quick sanity check of this surprisingly small value can be made in the following way: Assume a 1 gauss/ meter gradient. The source mass could produce a maximal gradient on the order of $2\chi$ times this gradient. This gradient would result in an acceleration of $10^{-8}\mu$Gal — still far below the level that would compromise the results of the experiment.

| Variable | Value |
|---|---|
| $R$ | 0.25 Ω |
| $A$ | 0.00018 $\mathrm{m}^2$ |
| mass | 0.13 kg |
| $v_{max}$ | 2 m/s |
| $\frac{dB}{dz}$ | $5 \times 10^{-7}$ gauss/cm |

Table B.2: A simple proof mass model for use with eddy current calculations.

The first order direct attraction between the source mass and proof mass may also be calculated. Using Equation B.1 we can calculate the attraction between the proof mass and just one pole of the "magnet" induced in the source mass, thus bounding the actual effect. Let us consider the magnetic "charge" induced on the face of the source and proof mass by a 1 gauss vertical constant magnetic field:

$$\mathcal{Q}_s = A_s\chi_s B = (.176m^2)(6.6 \times 10^{-4})(1 \times 10^{-4}T) = 1.16 \times 10^{-7}m^2T$$
$$\mathcal{Q}_p = A_p\chi_p B = (\pi(.01)^2m^2)(6.6 \times 10^{-4})(1 \times 10^{-4}T) = 2.1 \times 10^{-11}m^2T$$

The magneto-static force, $F$, is:

$$\text{Force} = \frac{\mathcal{Q}_s\mathcal{Q}_p}{r^2}$$

Here the subscripts $p$ and $s$ refer to the proof and source mass. $\mathcal{Q}$ is the induced effective magnetic surface charge. For a separation of 5 cm the force is $1 \times 10^{-18}$N, so the acceleration $a$ is:

$$\text{Acceleration} = \frac{\text{F}}{m} = \frac{1 \times 10^{-18} N}{.13\text{kg}} = 1 \times 10^{-8} \mu\text{G}al \tag{B.2}$$

Second order effects arising from magnetic poles induced in the proof mass from the perturbation fields created by the presence of the source mass are on the order of $\chi^2$ smaller still. Only negligible torques were introduced by these fields.

These calculations were all based on a single hollow cylinder of tungsten, of dimensions comparable to the ring of tungsten in the source mass. In fact the source mass also contains some stainless steel, bronze, and aluminum components.

In the 1997 experiment, 6 thin 304 stainless steel rods sandwiched the source mass together. Stainless steel was chosen because of its great strength)[1] . The susceptibility of this alloy is 0.02 ([55]), thirty times greater than the susceptibility of the tungsten alloy we used. The rods are the same height as the source mass, but have a net surface area almost 2000 times smaller than that modeled in tungsten. As the rods were at a radius from the drop comparable to that of the tungsten, and as the magnetic field was proportional to the product of the surface area with the susceptibility, the magnetic fields due to these components were a factor of $\frac{30}{2000}$ smaller.

It is also necessary to check on the signal due to the stainless steel bolts used to tie the smaller tungsten rods in place. These were cold worked, which had the effect of increasing their magnetic susceptibility. When the height of the material is decreased to a value consistent with the bolts used (but still preserving the surface area of the tungsten), the magnetic field induced in the mass is decreased by a factor of two, as does (surprisingly) the gradient of the magnetic field. Using the same argument before, we can limit the effect of these bolts to:

---

[1] In the 1998 experiment 12 aluminum rods were used instead. Also the 1998 run the fittings discussed later in this section were made of titanium, a non-magnetic material.

$$B_{\text{bolts}} = \frac{B_{\text{tungsten}} A_{\text{tungsten}} \chi_{\text{bolts}}}{2 A_{\text{bolts}} \chi_{\text{tungsten}}}$$

$$B_{\text{bolts}} \leq B_{tungsten}/3$$

The calculations of the effects of the AC magnetic fields produced by the drive motor were based on measurements of the reading of the balance in the test experiment, Sec. 5.2.8. Only a sample calculation is done here (all the real numbers may be found in [56]), for a single proof mass position. Table B.3 shows the field generated by the drive motor at the upper position of the test mass.

| Rotation frequency, Hz | Vertical $B_{pp}$, Gauss |
|---|---|
| 5.1 | 0.00256 |
| 9.2 | 0.00249 |
| 21.1 | 0.00214 |
| 39.9 | 0.00165 |
| 60 | 0.0014 |

Table B.3: Magnetic field of the drive motor at the upper proof mass position. $B_{pp}$ is the vertical peak-to-peak magnetic field.

Once I knew the magnitudes of the actual fields that would be sensed by the proof mass, I needed to generate much larger fields so that I could measure the corresponding force with the balance system. By using a bit of algebra the two could be related to give a limit on the actual force on the test mass. To increase our signal the coil was placed midway between the test mass and the drive motor. Table B.4 gives the calibration of one of the voice coils used to produce the larger fields. The full fields of the coils could not be directly measured because they saturated our sensor.

Once the coil was calibrated more current was driven through it and the force on the test mass was measured. Table B.5 contains the current and force measurements.

| Rotation frequency, Hz | Current, amps | Vertical $B_{pp}$, Gauss |
|---|---|---|
| 5.2 | 0.30 | 1.04 |
| 10.0 | 0.35 | 1.19 |
| 20.5 | 0.37 | 1.10 |
| 41.2 | 0.31 | 0.735 |
| 83.9 | 0.31 | 0.469 |
| 161 | 0.35 | 0.305 |
| 316 | 0.27 | 0.116 |
| 604 | 0.15 | 0.027 |

Table B.4: Calibration of the voice coil. This calibration was for the upper proof mass position. $B_{pp}$ is the vertical peak-to-peak magnetic field.

Now the force measured with the coils can be compared to the force of the drive motor. From Eqn. 5.8 the force at a given frequency is proportional to:

$$F_{\mathrm{r}} \propto \frac{B^2}{h^3}$$

where $h$ is the distance of the test mass from the dipole source. At a frequency of approximately 10 Hz, we can calculate the actual force error. From the calibration, a current of 0.35 amps corresponded to a field of 1.19 gauss. Thus the actual testing current of 6.6 amps must have made a field of 1.19x6.6/0.35 = 22.4 gauss. Recalling that the distance of the coil to the test mass was half the distance of the mass to the motor,

$$\frac{F_c}{F_m} = \frac{B_c^2/(1/8)}{B_m^2}$$

putting in the numbers gives:

$$\begin{aligned}\frac{F_c}{F_m} &= \frac{22.4 * 22.4 * 8}{0.00249 * 0.00249} \\ &= 6.5 \times 10^8\end{aligned}$$

So the force due to the motor was (5e-7 kg)(9.8 m/$s^2$)/6.5e8 = 7e-15 N. This

| Rotation frequency, Hz | Current, amps | Vertical Force, mg |
|---|---|---|
| 5.6 | 6.0 | 0 |
| 10.1 | 6.6 | 0.5 |
| 20.9 | 6.15 | 1.0 |
| 37.7 | 4.95 | 1.3 |
| 82.2 | 3.56 | 0.5 |
| 165 | 2.8 | 0.1 |
| 309 | 1.18 | 0 |
| 610 | 0.61 | 0 |

Table B.5: Calibration of one of the voice coils used in the experiment. This calibration was for the upper proof mass position. $B_{pp}$ is the vertical peak-to-peak magnetic field.

corresponds to an acceleration of the 100 gram test mass of 7e-14 m/$s^2$, or 7e-5 $\mu$Gal. This is completely negligible.

## B.3 Modeling Errors

### B.3.1 Source Mass Modeling Errors

This section presents the errors associated with mass measurements and approximations in modeling components of the source mass.

The large tungsten cylinders were weighed on a scale calibrated for stainless steel standard masses weighed in air (at 5200 feet altitude). This means that the scale, which measures a force, assumes both a value for g, and a buoyancy correction. The buoyancy correction is only correct if the mass being weighed really is stainless steel — in our case it wasn't. I corrected this problem, and buoyancy effects, in two steps. First I calculated the amount that the balance overestimated the mass of the tungsten (the balance added in the weight of too much air; tungsten is denser than stainless steel). This gave me the correct mass value for the cylinders. Then I calculated the mass of air displaced by the tungsten. Including this second correction in the model "automatically" compensate for the

| Description | Signal, $\mu$Gal |
|---|---|
| Eddy Current Damping | $< 0^{-7}$ $\mu$Gal |
| Direct Magnetic attraction | $< 10^{-6}$ $\mu$Gal |
| AC; Magnetic Forces | $< 10^{-4}$ $\mu$Gal |

Table B.6: Errors due to spurious forces. The effects of the source mass are discussed in Sec. 5.2.2.

gravitational attraction of the displaced air. The total correction to the reading on the scale was -4.76 grams per cylinder. The uncertainty associated with the mass of each of the 12 tungsten cylinders and the two aluminum plates (arising from the scale's accuracy) is ±1 gram. The total mass uncertainty (for the cylinders) was taken as $1\text{g} * \sqrt{14} = 4$ g.

In the same way a buoyancy correction was applied to the upper and lower aluminum plates of the experiment. 1997: the Upper plate was modeled 0.62 grams lighter than its true mass, while the lower plate was made 0.76 grams lighter. 1998: the lower plate was modeled 1.53 grams lighter and the upper was made 1.55 grams lighter.

The error in the buoyancy corrections due to barometric pressure changes (approximately 1% magnitude) is far smaller than the error in weighing, and therefore is ignored. In some sense the time-varying barometric pressure correction, which shifts with pressure, is a variable independent of our signal and is therefore absorbed in the statistical errors of the experiment.

The mass uncertainty in all other components of the system (about 20 different objects, in which nuts and bolts were weighed as collections) is 0.1 gram. This leads to a total error estimate of 0.5 g. Grease on the screws collected on the nuts and thus traveled with the source mass. The weight of a sample of grease of about the same volume as that on the nuts weighed 5 grams. I couldn't reliably model this effect because the screws were often cleaned. Rather than assume an average perturbation, the whole grease effect is accepted as an error.

The measurement of the position of the center-of-mass with respect to the geometric centers of the tungsten cylinders allowed us to make estimates of errors from angular and linear density variations within the cylinders. 11 of the 12 tungsten cylinders had an angular density variation producing a torque equivalent to a 25 gram mass placed on their circumferences. The twelfth mass, however, (#4) displayed no angular density variation, and was therefore suspect (discussed in Appendix A). We needed to include an estimate for the error introduced by these characteristics.

Exactly how to calculate the errors due to these types of sources was not immediately clear. The position of an unmodeled point mass distribution strongly influences the magnitude of the signal error it causes. We decided to assign a value of 5g as the over all uncertainty in the mass of the source mass, distributed uniformly about the source mass. We also modeled a 25 gram point mass in the position that results in the largest signal bias. The possibility of a misplaced point of mass of 25 grams is of greater probability than an error in the total mass of this size because a misplaced point mass represents the uncertainty in density inhomogeneities in the masses. It is interesting that a 25 gram mass placed on the inner radius near the middle of the source mass results in a bias in the differential signal of 0.01 $\mu$Gal, yet if the 25 grams were distributed uniformly around the source mass, they would have a signal of:

$$\text{perterbed signal} = \frac{\text{25g total signal}}{\text{mass of source mass}} = \frac{25g}{40kg * 12}(80\mu\text{Gal}) = 0.005\mu\text{Gal} \tag{B.3}$$

This result indicates that even if our source mass were infinitely dense, our signal could only be improved by approximately a factor of two (assuming no major redesign of the FG-5 and conserving the net mass of the source mass)!

| Description | Signal, $\mu$Gal | Signal, ppm |
|---|---|---|
| Mass estimates errors | 0.002 | 25 |
| Unmodeled grease and unknown point mass | 0.005 | 60 |
| density variations: linear | 0.004 | 50 |
| Radial | 0.002 | 25 |
| Angular | 0.002 | 25 |
| quadratic | 0.005 | 60 |
| TOTAL | 0.011 | 110 |

Table B.7: Uncertainties in proof mass position and orientation

Other approximations in the source mass model were unimportant. The error from modeling an array of screws as a ring of screws is approximately $2 \times 10^{-8}\mu$Gal. the thread as part of the screw is approximately $4 \times 10^{-9}\mu$Gal. Table B.7 displays the errors associated with modeling of the source mass.

### B.3.2 Proof Mass Modeling errors

To scale errors of modeling the proof mass and to discover the degree of precision required for an adequate model to be constructed, I made three simplified models of the proof mass. The first was a vertical line charge of mass, the same length as the proof mass. To test the sensitivity of the results to the vertical "granularity" of the model, the line charge was broken into $n$ point charges, equidistant from each other. Figure B.2 displays the differences in net accelerations for the given models falling though a field generated by a simplified source mass model. The data shows that the convergence is better than linear, so with 32 layer model in the vertical direction we expect the error to be less than twice the maximum difference between the acceleration of the 64 layer model and the 32. This difference is 0.0015 $\mu$Gal. A vertical granularity corresponding to 64 layers (1.25 mm/step) was used in the final proof mass model.

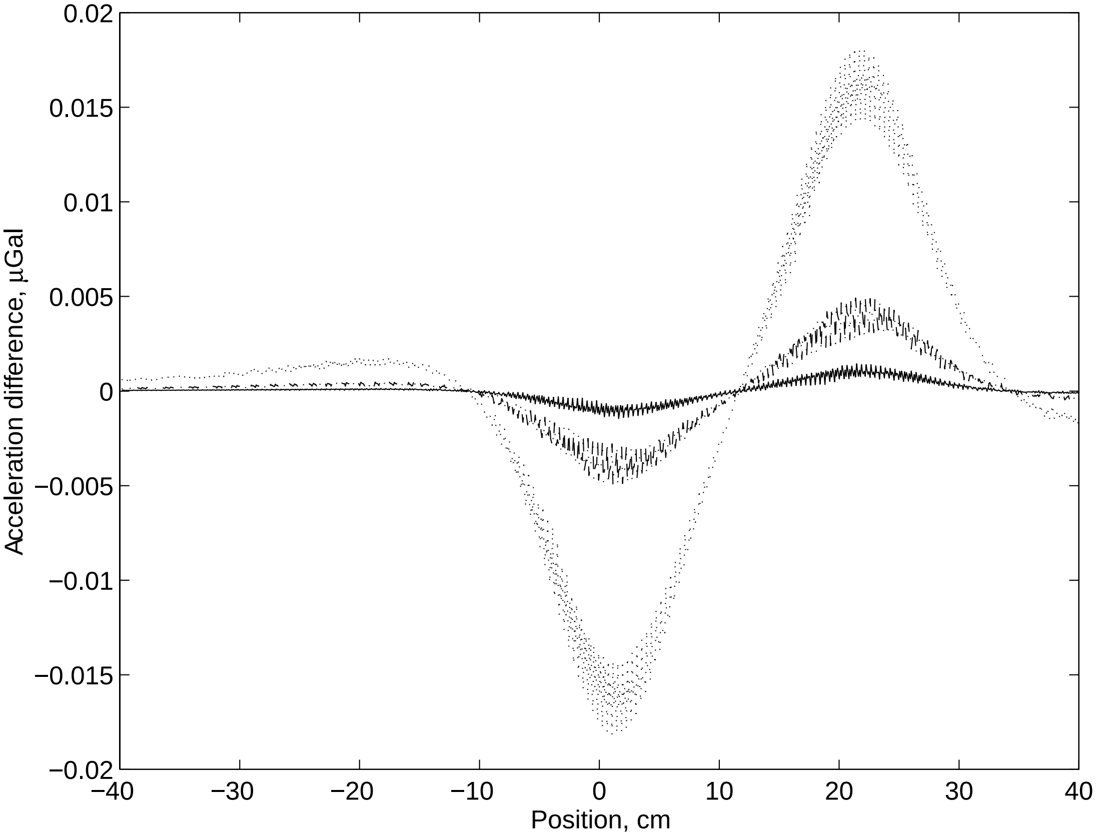

Figure B.2: Change in vertical acceleration as a function of the vertical granularity of model. (—) the difference between calculated acceleration for a vertically oriented line charge of the same length as the actual proof mass, modeled as 64 and 32 point masses. (-·-) modeled as 32 vs 16 point masses and (· · ·) modeled as 16 vs 8 point masses.

I performed a similar test of the horizontal granularity sensitivity by using a 1 cm line-charge radially oriented. Although the proof mass actually extends to a 1.5cm radius, modeling granularity in not an issue at these radii, because the proof mass portions can be nearly perfectly described as cylinders. The corner cube, the object most badly approximated by a cylinder, extends to a 0.5 cm radius. Figure B.3 plots differences in accelerations for various granularity models. Using a radial model granularity of 0.125 cm is adequate for our purposes, introducing only 0.0012 $\mu$Gal error.

In one last test of the sensitivity, in both dimensions at the same time,

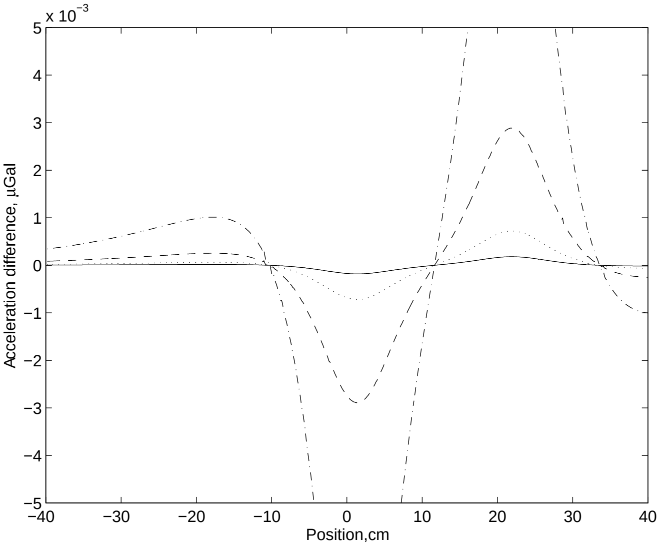

Figure B.3: Change in vertical acceleration as a function of the radial granularity of the model. (—) the difference between calculated acceleration for a horizontally oriented line charge extending from the axis of symmetry to 1 cm off axis, modeled as 32 and 16 point masses. (···) Modeled as 16 vs 8 point masses, (- -) 8 vs 4, and (· − ·) 4 vs 2 points.

I modeled an hourglass shaped mass with its axis of symmetry aligned in the vertical direction. The hourglass was the same height as the actual proof mass, and of 1 cm maximum radius. The results of this test show that a granularity of 32 slices across the height of 8 cm is satisfactory for the experiment, resulting in an error that (using the extrapolation to an continuous object) is good to better than 0.01 $\mu$Gal.

This granularity is so coarse that actual modeling errors of reasonable magnitude are not going to affect the accuracy of the results strongly. For example, the proof mass is made up of some objects that are very well modeled as cylinders — they only differ from perfect cylinders in that they are imperfectly machined. When we model these pieces as perfect cylinders, the actual object may vary from the model by some small fraction of a millimeter: certainly by less than 0.003cm. Since we only need the granularity to be better than about 0.1 cm, these errors are lost in the glare of large modeling approximations. The fact that many pieces of the proof mass are very good approximation of cylinders means that adopting the whole error due to granularity is unreasonable. Because well over half of the mass is contained in objects which are perfectly described as cylinders to levels of 0.01 cm, we might halve the error estimates for granularity errors. Since the errors are so small, however, they are maintained.

The final proof mass model was made with a vertical and horizontal granularity of better than 0.125 cm. This corresponds to an error of 0.0015 $\mu$Gal due to the vertical approximation, and 0.0006 $\mu$Gal due to the radial approximation, for a fully complex object, in a single source mass position.

The model of the proof mass was developed from machine drawings and measurements of the masses of individual proof mass components. There were three elements of the model, the corner cube holder, corner cube, and glue that we weren't able to weigh independently (because they're all glued together). We weren't able to get their masses by weighing disassembled assemblies because they aren't very consistent from piece to piece. For this reason we had to estimate[2] the mass distribution between the three components. This error introduced by the uncertainty in this distribution is greater than the combined uncertainty in all other components of the model.

Only the relative masses of each component of the test mass was important in our models. Since the components were weighed in air a relative mass error between materials of different density was introduced. The buoyancy correction for the optical sphere, for example, is 0.002 grams. This is an order of magnitude smaller uncertainty in the accuracy of the scale used in the measurements. We

---

[2] We chose to use the greatest mass observed for both the corner cube and the corner cube holder, and make up the mass difference in the binding glue. Our original estimate of the glue weight was based on a similar system, in which a corner cube was glued to a small aluminum cylinder modeled on the corner cube holder. The glue mass used in this system was 0.29 grams, only about 20% lighter than our final glue estimate.

| Description | Signal, $\mu$Gal | Signal, ppm |
|---|---|---|
| radial Model Granularity | 0.0012 | 15 ppm |
| Vertical Granularity | 0.003 | 35 ppm |
| Relative Mass Errors (CC, CCholder,Glue) | 0.003 | 35 ppm |
| Relative Position Errors | 0.007 | 80 ppm |
| Total | 0.008 | 90 ppm |

Table B.8: Uncertainties in proof mass position and orientation

made the assumption that all the material of the proof mass was free of voids and appreciable density variations.

The positions of each element have uncertainties of as much as 0.01 cm. By modifying the weight and position of individual elements of the the proof mass model, and testing the output solution, I obtained error estimates of: 0.002 $\mu$Gal in the final signal due to a 0.07 cm translation of any of the major proof mass elements and and error of 0.0009 $\mu$Gal due to a 0.1 gram mass error. The proof mass is built of approximately 10 pieces, so the total error due to incorrect weights and positions is about 0.007 $\mu$Gal.

Table B.8 lists the proof mass modeling errors. The final proof mass model that we used in Appendix A.

## B.4 Numerical System

### B.4.1 Absolute Accuracy of Quadrature: The Integration Over the Source Mass

To insure the accuracy of our numerical results we used quadrature algorithms that calculated error estimates for the values they returned. The algorithms were checked against analytic solutions whenever possible[3] . We implemented the integration algorithms twice, using a straight 4-D integration as a check to the

---

[3] We used analytic solutions for the the case of cylinders with a common axis of symmetry.

interpolation scheme discussed in Sec. 2.1. Unfortunately the 4-D integration was incredibly slow — a full test of the integration over the complete source and proof mass models could not be performed. Once we were sure that the implementations were consistent and correct for small systems of masses the interpolation system (that was used in the final calculations) was tested for self-consistency.

The main source of concern was the required density of grid points in the interpolation field to achieve our required accuracy. A standard method of testing for sufficient density is to double the density until the variation in the final values (integrated over the grid) becomes negligible. Figure B.4 is a plot of the net acceleration of the proof mass (using a 44 piece model) as a function of the number of grid points used in the vertical direction. The three plots were all calculated using the same radial grid density of 30 points/3 cm. The 500 to the 1000 point accelerations differ by less than 0.001 /Ugal, as seen in Figure B.5. Results for a radial grid density of 15 points/3 cm are very similar.

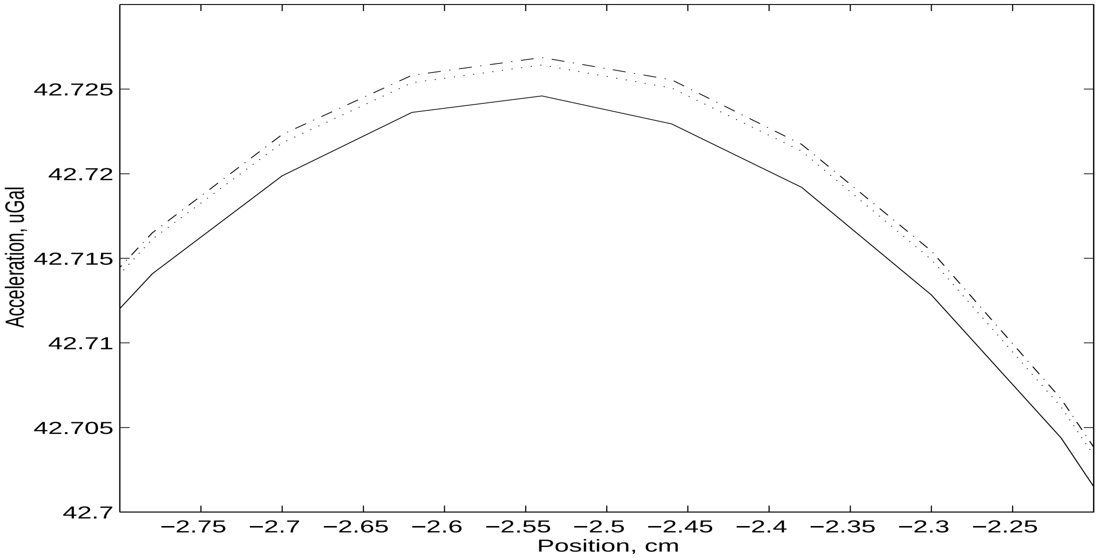

Figure B.4: Calculated acceleration for a 44 piece proof mass model, using three different vertical grid densities. The — line represents the acceleration resulting from using 250 grid points in the vertical direction (over approximately 90 cm ). The $\cdots\cdot$ line results from 500 points, and the -·- line from 1000 points.

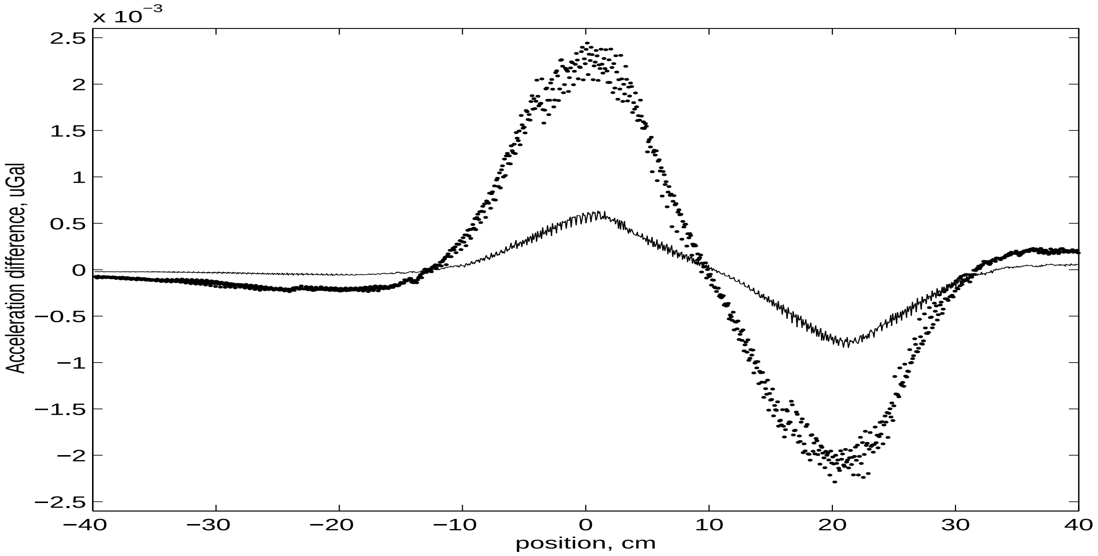

Figure B.5: Differences in calculated acceleration for a 44 piece proof mass model, using three different vertical grid densities. The solid line represents the difference in accelerations calculated using 1000 grid points and 500 grid points. The dotted plot is the difference between the results of a 500 and a 250 point grid. All grids used had 30 grid points off axis.

Testing the dependence of calculated acceleration on radial grid density in the same way insured the appropriate choice of grid size. Figures B.6 and B.7 show computed results for three different radial grid densities. Based on these results, the final solution was calculated using a vertical grid density of 1000 points/90 cm, and a radial density of 30 points/3 cm. These plots clearly indicate that the error in the interpolation due to the radial grid density is bound by 0.0005 $\mu$Gal .

### B.4.2 Assumption of Cylindrical Symmetry

The two-dimensional interpolation grid algorithm assumes that the field of the source mass was cylindrically symmetric. Although the mass is 1-, 2-, 3-, and 6-fold rotationally symmetric[4] , it was not cylindrically symmetric. Figure B.8 displays the vertical field as a function of angle for each of six cylinders making up a simplified source mass model. The plots were made for a vertical position

---

[4] To the degree that the masses were perfectly homogeneous...

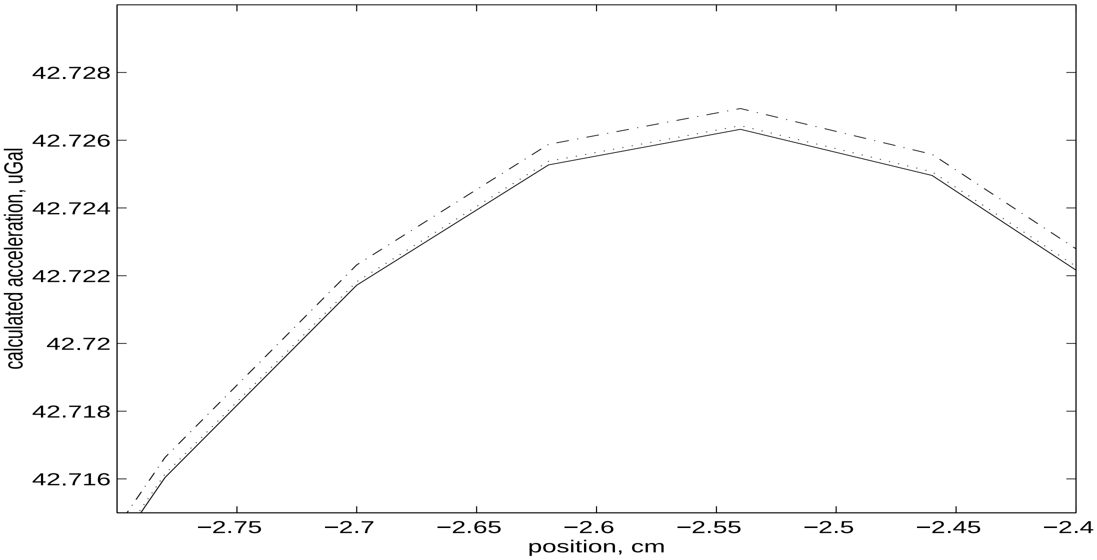

Figure B.6: Calculated acceleration for a 44 piece proof mass model, using three different radial grid densities. The — line represents the acceleration resulting from using 60 grid points over 3 cm. The · · · · line results from 30 points, and the -·- line from 15 points, over the same range.

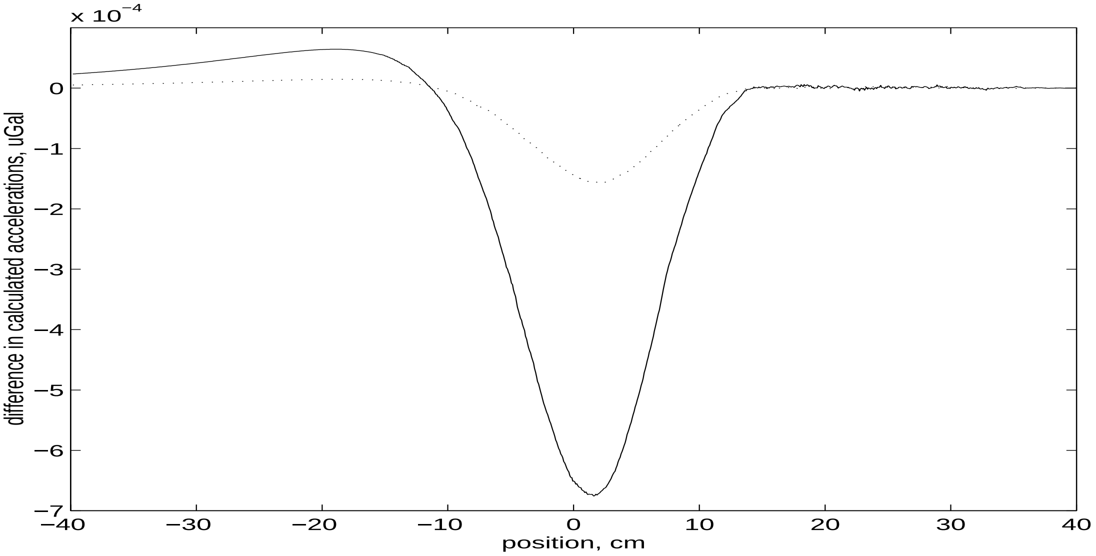

Figure B.7: Differences in calculated acceleration of a 44 piece proof mass model, using three different grid densities. The solid line represents the difference in accelerations calculated using 30 grid points and 15 grid points over 3 cm. The dotted plot is the difference between the results of a 60 and a 30 point grid. All grids used had 500 grid points over 90 cm on the vertical axis.

at a maximum of the vertical field. The dependence on vertical field magnitude on angle is more clearly seen in Figure B.9. The approximation of cylindrical symmetry is clearly valid to better than 1 nGal, or a level of approximately 2 parts in $10^5$. At the zero in the field, at the center of the source mass (but with the same radial offset) the variations are two orders of magnitude smaller.

### B.4.3 Differential Precision of the System

Because there might be a non-linear error in the numerical integrations (who knows?) I was concerned that the differential accuracy of the method was suspect. By testing the integration of the differential equation describing the motion of the test mass falling through various fields, I found that the numerical result was good to 2 parts in $10^6$ for a 80 $\mu$Gal signal. At this level the algorithms showed some lack of stability. As the goal of the experiment was for a result good to 5 parts in $10^4$, this is more than sufficient. The differential accuracy was tested on a constant field and a linearly changing field.

| Description | Signal($\mu$Gal ) | Error (ppm) |
|---|---:|---:|
| Interpolation Density | 0.0015 | 20 |
| Assumption of Cylindrical Symmetry | 0.001 | 10 |
| Numerical Stability | 0.0002 | 2 |

Table B.9: Errors due to the numerical system. Errors arising from the precision of the quadrature algorithms are negligible.

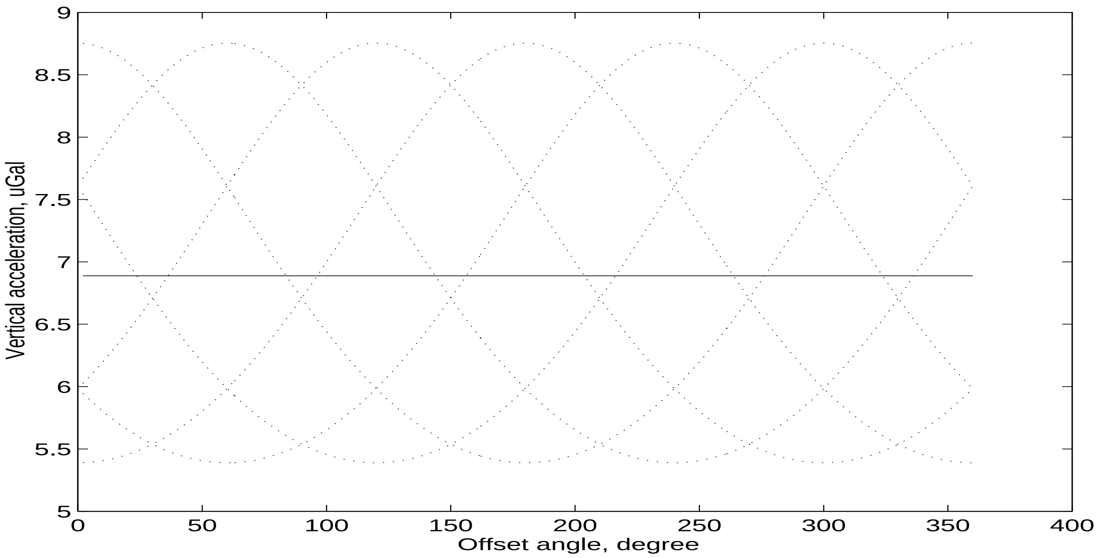

Figure B.8: Vertical acceleration from a source mass model constructed of six cylinders. Values are plotted as a function of angle from a line of symmetry, for a point 2 cm off axis. Note that that contributions of the individual cylinders (····) are not true cosines( as they would be if the vertical force on the proof mass were a function linear in the distance between the proof mass and the cylinder) because they are modulated by the $\frac{1}{r^2}$ factor in the gravitational interaction. The solid line represents the average acceleration due to each cylinder. As far as this curve approximates a line, the field is cylindrically symmetric.

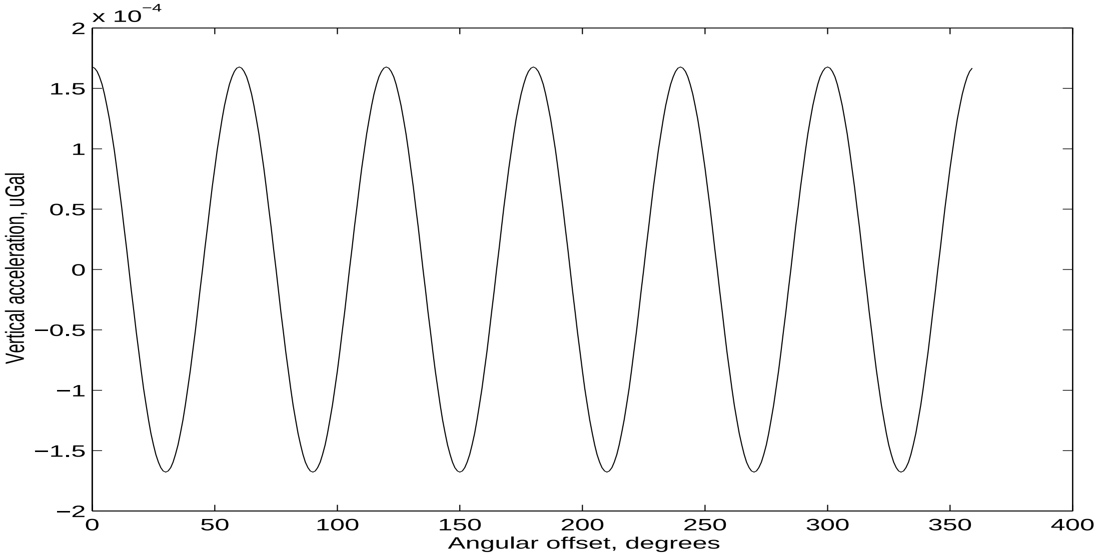

Figure B.9: Variation of vertical acceleration as a function of angle when 2 cm off axis. At a maximum in the field, this plot shows that the field is cylindrically symmetric to 0.2 nGal, at a 2 cm radius.